University of Nevada, Reno

Application of Geothermal Play Fairway Analysis to the Desert Queen Geothermal Prospect, Northern Hot Springs Mountains, Churchill County, Nevada

A thesis submitted in partial fulfillment of the requirements for the degree of Master of Science in Geology

by

Nolan P. Dellerman

Dr. James E. Faulds/Thesis Advisor

December, 2021

THE GRADUATE SCHOOL

We recommend that the thesis
prepared under our supervision by

NOLAN P. DELLERMAN

entitled

**Application of Geothermal Play Fairway Analysis
to the Desert Queen Geothermal Prospect,
Northern Hot Springs Mountains, Churchill County, Nevada**

be accepted in partial fulfillment of the
requirements for the degree of

MASTER OF SCIENCE

James E. Faulds, Ph.D., *Advisor*

Andrew Zuza, Ph.D., *Committee Member*

Scott Basset, Ph.D., *Graduate School
Representative*

David W. Zeh, Ph.D., Dean
Graduate School

December, 2021

ABSTRACT

This study utilized a multidisciplinary approach to assess geothermal potential at the Desert Queen geothermal area, a known blind geothermal system in western Nevada. Geothermal play fairway analysis was employed to vector into the most favorable areas for further exploration in the Desert Queen basin. This study hinged on decades of previous exploration work by synthesizing and expanding upon many existing datasets, including detailed geologic mapping, temperature gradient well data, 2 m temperature probe data, and multiple geophysical surveys. With the addition of new geologic and geophysical data, a comprehensive structural model was completed to elucidate the structural controls on geothermal activity. The motivation for applying the play fairway analysis methodology to the Desert Queen area was to further refine the method at a fine-scale in the middle to late stages of exploration.

The Desert Queen area occupies the eastern portion of the northern Hot Springs Mountains adjacent to two power producing geothermal systems, Bradys and Desert Peak. The northern Hot Springs Mountains lie within the Basin and Range province directly northeast of the Walker Lane, where dextral shear diffuses into and enhances regional extension. The Desert Queen geothermal system appears to be controlled by the southward termination and horse-tailing of the Desert Queen fault zone, a major east-dipping normal fault, as well as a step over to a less prominent fault to the east, the Power Line fault. The termination and step over of the Desert Queen fault zone generated a zone of structural complexity marked by abundant closely spaced normal faults. Enhanced

permeability induced by greater fracture density within this structurally complex area generated a favorable environment for geothermal activity.

Detailed geologic mapping, structural analysis, and geothermal play fairway analysis have resulted in the delineation of five favorable structural settings that potentially control geothermal activity in the area. Two of the favorable structural settings are hybrid overlap settings that are the most favorable based on multiple lines of evidence. Both hybrid settings are marked by a 2 m temperature anomaly that spatially coincides with the warmest temperature gradient wells. The hottest measured temperature within the Desert Queen basin (140°C) occurs in a well proximal to the eastern hybrid overlap between the Desert Queen fault – Power Line fault step over and the termination of the Power Line fault into the Desert Queen basin. The western hybrid overlap between the termination of the Desert Queen fault and the step over to the Power Line fault has moderate shallow temperatures but slightly higher play fairway favorability scores. Fluids may upwell in the vicinity of the western hybrid setting and flow up and out to the east-northeast. An alternative interpretation is that multiple upwellings occur at Desert Queen in the vicinity of both hybrid settings. This study indicates two promising areas to focus further exploration at Desert Queen. Additionally, the fine-scale, geothermal play fairway analysis has been shown to be an effective tool in middle to late stages of exploration.

ACKNOWLEDGMENTS

I would like to extend the upmost gratitude and thanks to my advisor Jim Faulds. Not only for the superb opportunity to work on the Desert Queen project, but for his guidance, mentorship, friendship, and incredible patience along the way. My graduate career was presented with some unique challenges that would have tanked me without Jim's support. Most importantly, Jim has shaped me into a legitimate scientist, and for that I am indebted. Many thanks go out to Mark Coolbaugh for his collaboration and quick execution of the play fairway analysis, Jeff Witter for the extensive back and forth on the 3D inversion model (still ongoing), Drew Siler for providing code and know-how on the slip and dilation tendency analyses, and to Trenton Cladouhos for great insight and a periodic fresh set of eyes. Additional thanks go out to Chris Kratt for flying the aeromag survey at Desert Queen, and Jennifer Mauldin for the crucial cartography tips. A special thanks to everybody within the GBCGE for collaboration, ideas, and general support and interest in this project. Thanks to all the fellow graduate students along the way for shared ideas, extra motivation, and comic relief. Thank you to my additional committee members Scott Bassett and Andrew Zuza for support. Andrew helped me get started on the painstaking process of mineral separation (only to run out of time and send those samples off). This work was funded by Cyrq Energy/ Raser Power Systems, LLC for which I thank Trenton Cladouhos.

I must acknowledge the immense support and sacrifice made by my amazing wife throughout this process. Life doesn't stop when one goes through graduate school, and many responsibilities were taken on by her. I would probably still be stuck on a

dewatering rig if not for her encouragement through this program. Lastly, I thank my little girl Ellie for giving me the drive I needed to finish this.

TABLE OF CONTENTS

LIST OF TABLES

LIST OF FIGURES

1. Introduction

Geothermal energy is an important form of renewable energy that does not rely on weather patterns or sunlight. Geothermal power production is a baseload energy source, meaning it can operate almost continuously. Additionally, the process of producing energy from a geothermal system emits very little CO_2 into the atmosphere. Increased energy demand, depletion of hydrocarbon resources, and the trajectory toward "clean" energy are all factors contributing to the need to utilize and develop geothermal energy.

In general, there are three major geologic conditions that allow for geothermal resources to reside within a few kilometers of the surface such that they can be developed: 1) heat in the shallow crust, 2) permeable reservoir rock, and 3) fluids to circulate heat (Jolie et al., 2021). This geologic recipe is most commonly found proximal to active tectonic settings, where heat and permeability result from an array of dynamic processes. For example, the Great Basin region of the Basin and Range province of western North America contains abundant geothermal systems, which can be attributed to the active extensional to transtensional tectonic setting and associated high heat flow of the region (Blackwell et al., 1999; Wisian, 1999) (Figure 1.1). Most of the geothermal activity in the region occurs along faults and cannot be related to shallow magma sources, as magmatism in the Great Basin region generally ceased ~3-10 Ma (Faulds et al., 2006). Instead, geothermal systems in the Great Basin region are generally amagmatic, and both heat and permeability result primarily from the extensional tectonic regime. High heat flow induced by crustal thinning characterizes essentially the entire Basin and Range province (Figure 1.1), and thus permeability is the most important geologic condition

controlling geothermal activity.

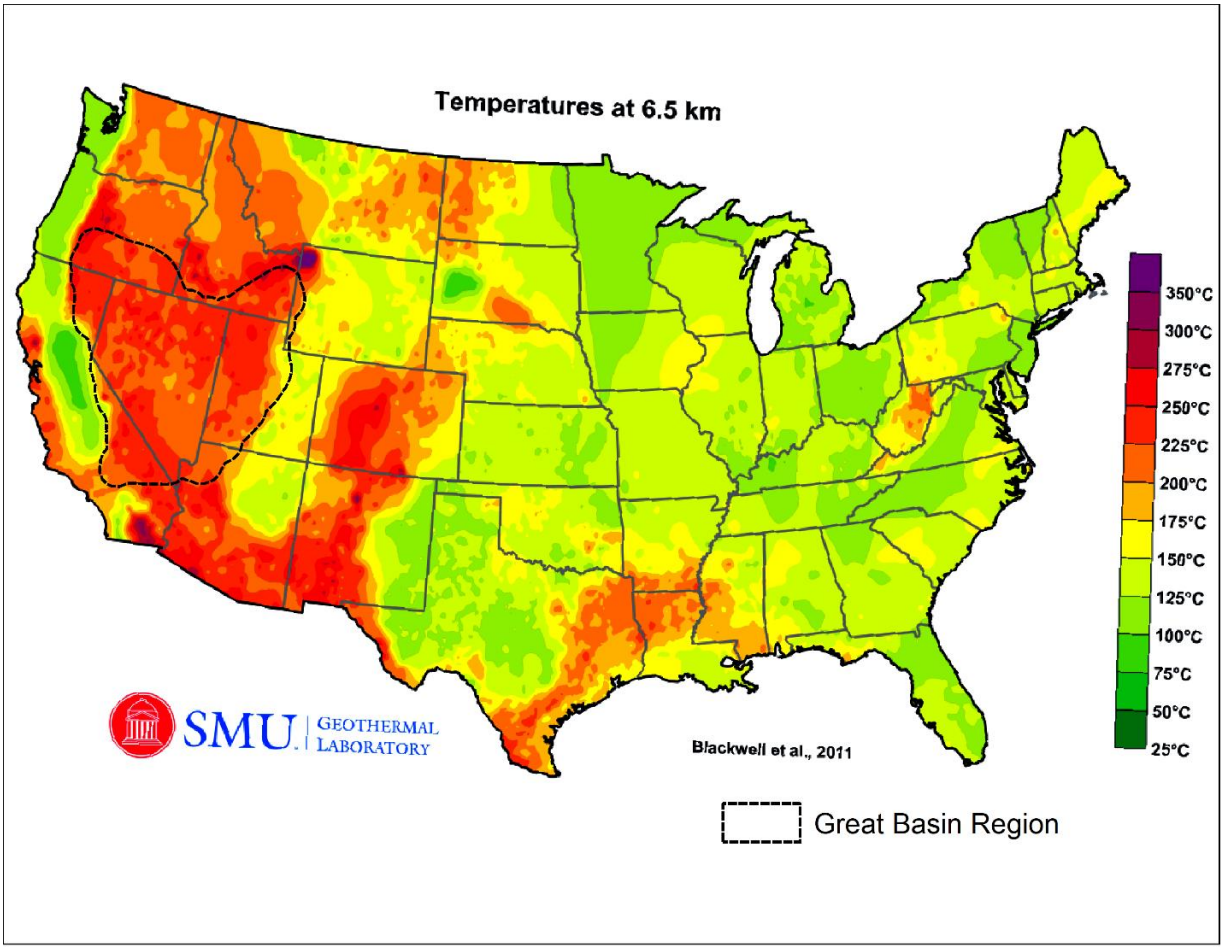

Figure 1.1 Temperature at 6.5 km depth of the contiguous United States (modified from Blackwell et al., 2011). Dashed black line shows outline of Great Basin region.

Notably, geothermal energy is underutilized in the Great Basin region with only 28 producing geothermal systems. At least ~1000 MWe of undiscovered geothermal resources remain in Nevada alone, with some accounts suggesting much larger amounts of untapped potential in Nevada and the Basin and Range as a whole (Williams et al., 2008; Augustine et al., 2019). The underutilization of geothermal energy in the Great Basin region results in part from the blind nature of as much as 2/3 of all geothermal resources, meaning that there are no surface expressions in the form of fumaroles, hot

springs, or geysers (Coolbaugh et al., 2006).The geothermal systems in the Great Basin region cluster in north-northeast trending belts, and faults striking N0E – N60E are the primary controlling structure for ~75% of the fields in Nevada (Faulds et al., 2004). Additionally, most geothermal systems across the region are controlled by 4-6 favorable structural settings (Faulds et al., 2011, 2021; Faulds and Hinz, 2021) (Figure 1.2). The most favorable settings are step-overs or relay ramps along normal faults, hosting ~32% of such systems. Other settings include horse-tailing normal fault terminations (25%), fault intersections (22%), displacement transfer zones, accommodations zones, and pull apart systems (Faulds et al., 2011, 2015b).

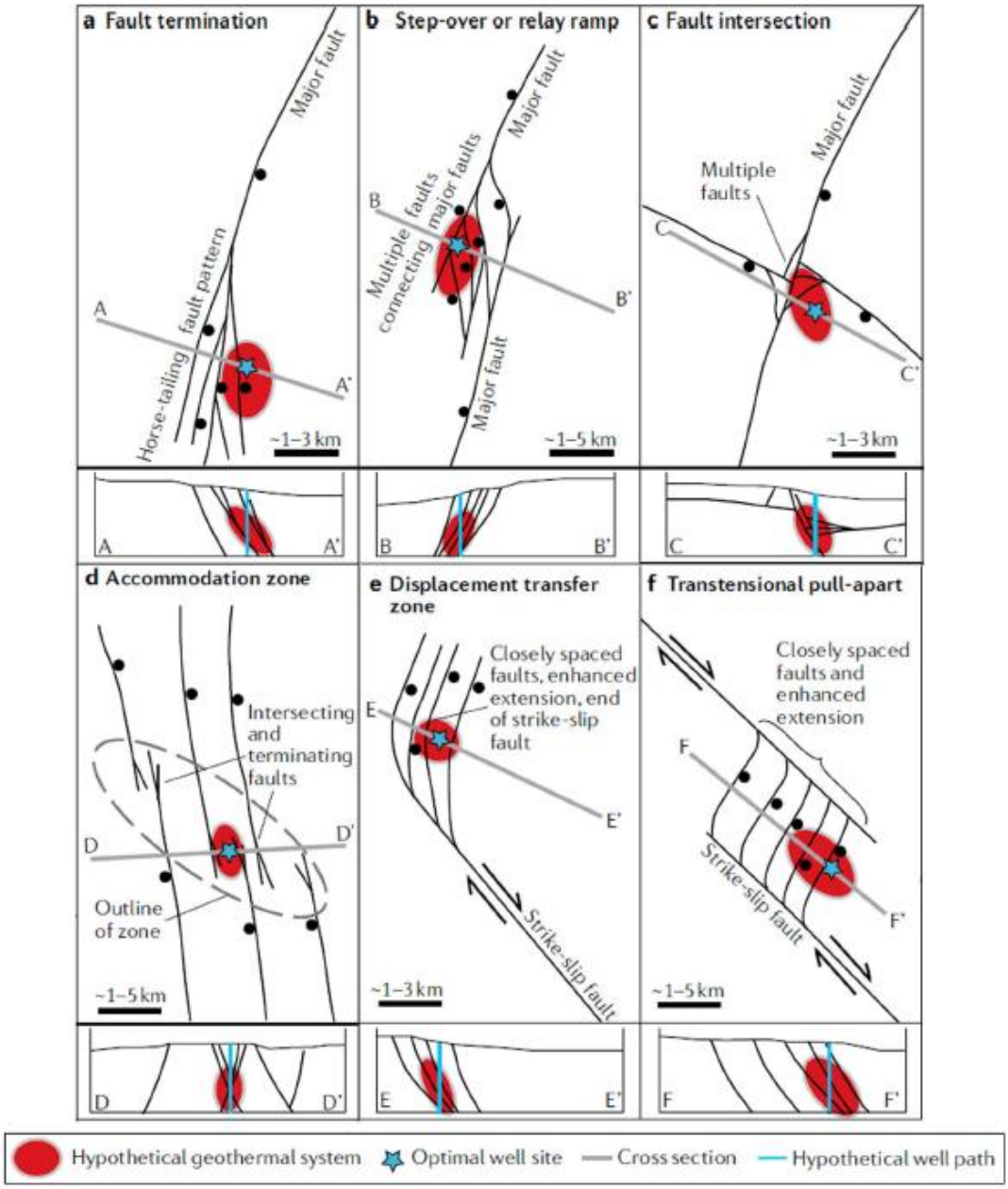

Figure 1.2. Schematic examples of favorable structural settings (modified from Faulds et al., 2021)

These settings are associated with more closely spaced faults and structural complexity, which ultimately allow for *enhanced permeability*. This increased permeability ultimately facilitates fluid flow and allows for geothermal fluids to circulate more readily from deeper levels in the crust, thus facilitating development of relatively

high temperature (>130°C) geothermal systems within a few kilometers of the surface (Faulds et al., 2011, 2015b). Due to the implication that permeability is the most important factor and that faults control most of the geothermal systems in the Great Basin region, it is pertinent to discern the structural controls on individual systems. Because many geothermal systems in the region are blind systems (Coolbaugh et al., 2006), it is also imperative both to analyze known blind systems and to identify favorable settings that may host a blind system.

The Nevada geothermal play fairway project (Faulds et al., 2015, 2016, 2018, 2020), funded by the Department of Energy aimed to develop workflows and methodologies to integrate different datasets to identify potential geothermal exploration targets associated with blind geothermal systems across about one third of Nevada. Play fairway analysis was adapted from the petroleum industry, which uses it to reduce exploration risk through integration of multiple datasets and regional analysis (Magoon and Dow, 1994; Grant et al., 1996; Doust, 2010). In addition to Nevada, geothermal play fairway analyses have been applied to several other areas in the western U.S., including parts of Washington, Idaho, New Mexico, California, Utah, and Hawaii (Forson et al., 2016; Shervais et al., 2016; Nash and Bennett, 2015; Siler et al., 2017; Wannamaker et al., 2017; Lautze et al., 2017).

The Nevada play fairway analysis project consisted of three phases. Phase 1 (Faulds et al., 2015) utilized a geostatistical approach by applying nine parameters to a 96,000 km^2 area across the Great Basin region o in west-central to eastern Nevada. Structural setting, slip and dilation tendency of Quaternary faults, strain rates, modeled sub-surface temperature at 3 km depth, age and slip rate on Quaternary faults, gravity

data, and earthquake density were integrated to calculate play fairway scores across the area (Faulds et al., 2016). Geochemical and temperature data from available springs and wells were then incorporated to evaluate favorability. Ultimately, this led to the production of predictive play fairway and favorability maps that combined heat and permeability as the main factors (Faulds et al., 2015) (Figure 1.3). This study identified 24 particularly promising sites across the Nevada study area, and five areas were selected for more detailed study in Phase 2 of the project (Craig et al., 2017; McConville et al., 2017; Faulds et al., 2019, 2020; Hinz et al., 2020). Phase 3 of this project involved additional geophysical surveys and temperature gradient drilling of two sites, southeastern Gabbs Valley and Granite Springs Valley. One of the five areas selected, southeastern Gabbs Valley, was shown to host a previously undiscovered blind geothermal system (Craig, 2018; Faulds et al., 2018; Craig et al., 2021).

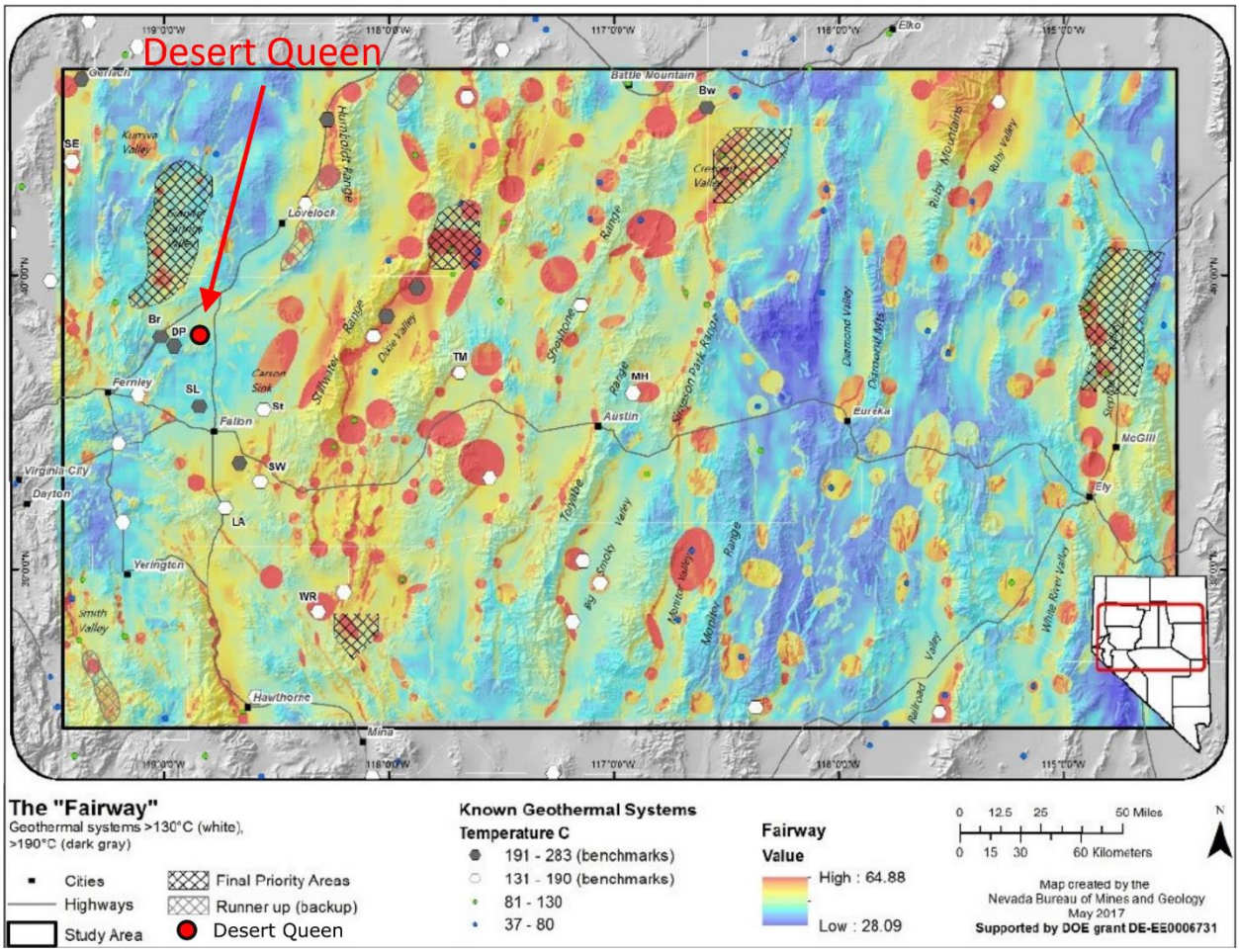

Figure 1.3. Nevada play fairway map modified from Faulds et al. (2015). Warmer colors indicate higher play fairway scores. Location of the Desert Queen geothermal system is annotated with red circle and red arrow.

The effectiveness of the play fairway methodology on the broad scale of the Great Basin region, and in discrete areas, such as southeastern Gabbs Valley, were important proof that the play fairway method is effective in early stages of geothermal exploration. The motivation of this study was to apply the play fairway analysis to a known geothermal system in the middle to late stages of exploration in the Desert Queen area of the northern Hot Springs Mountains (Figure 1.4). The Desert Queen geothermal prospect is an excellent candidate for applying play fairway analysis at a finer local scale because

this area has been shown to host a blind geothermal system (Faulds et al., 2010), as evidenced by regional thermal gradient drilling (Benoit, 2011). Desert Queen is proximal to two commercial grade geothermal systems (Bradys and Desert Peak), which host power producing plants, both within the northern Hot Springs Mountains. A 2 m temperature survey has also delineated a shallow thermal anomaly in the Desert Queen basin (Coolbaugh et al., 2007a).

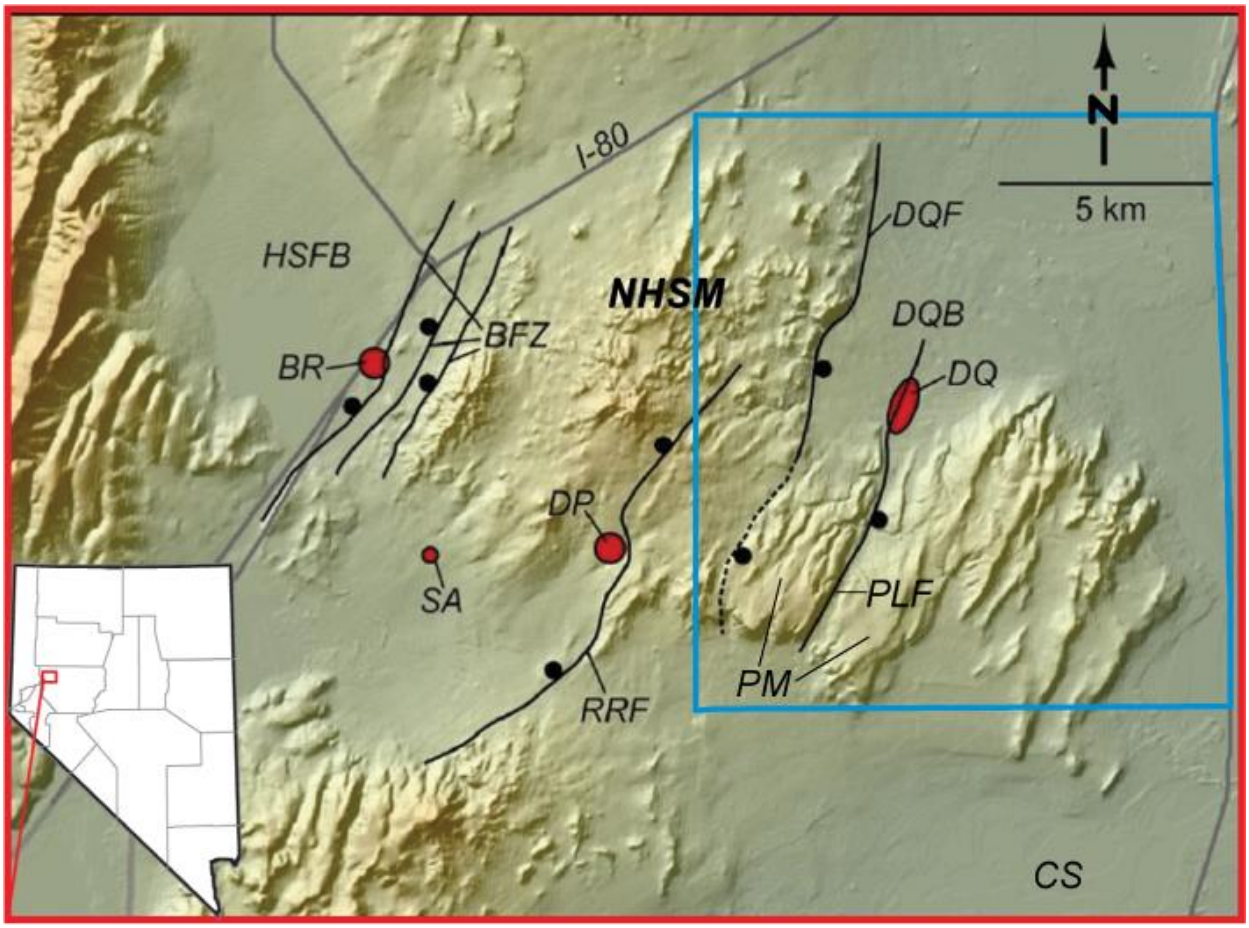

Figure 1.4. DEM of the northern Hot Springs Mountains (NHSM) modified from Faulds et al. (2010), showing major faults and geothermal fields. Ball shown on downthrown sides of faults. Independent geothermal fields marked by larger red circles. BFZ, Bradys fault zone; BR, Bradys geothermal field (area of production wells); DP, Desert Peak geothermal field (area of production wells); DQ, Desert Queen geothermal field (area of hottest temperature-gradient wells); DQB, Desert Queen basin; DQF, Desert Queen fault zone; PLF, Power line fault; HSFB, Hot Springs Flat basin; RRF, Rhyolite Ridge fault zone; SA, small geothermal anomaly; PM, Parran Mesa; CS, Carson Sink. Desert Queen study area is outlined in blue. Inset map at lower left shows location of the northern Hot Springs Mountains in the state of Nevada.

The primary goals of this study were to better characterize the Desert Queen geothermal system by refining its structural setting, collecting additional geological and geophysical data, and integrating existing geological and geophysical datasets to synthesize these parameters into a local-scale, site-specific play fairway analysis (e.g., Craig, 2018; McConville, 2018; Faulds et al., 2019, 2020; Hinz et al., 2020; Craig et al., 2021). A major motivation for the analysis conducted at Desert Queen was further refinement of the play fairway methodology at a fine-scale, as well as a test of the methodology in later stages of exploration. This study builds on previous work in the Desert Queen area (e.g., Benoit et al., 1982; Faulds et al., 2010; Benoit, 2011) but represents the first attempt to fully integrate all existing datasets. Compared to previous work at Desert Queen, this study also incorporated several additional parameters, including new geologic mapping, structural analysis, magnetic, magnetotelluric (MT), and thermal gradient drilling data, all critical for a comprehensive assessment of the Desert Queen geothermal prospect. This, in turn, afforded identification of the most favorable areas for further exploration and potential geothermal development at Desert Queen.

2. Geologic Setting

The regional tectonic and geologic settings of the Desert Queen geothermal area are important to understand. The broad tectonic context provides a foundation for assessing the local geologic setting and also for applying geologic methods, such as detailed geologic mapping and structural analysis. Additionally, a detailed description of the local geologic setting permits review of the features that may contribute to

geothermal activity at Desert Queen.

2.1 Regional Tectonic Setting

The Desert Queen geothermal area is located in the northern Hot Springs Mountains near the northwest margin of the Carson Sink ~80 km northeast of Reno, Nevada. This area is near the boundary of the northern Walker Lane and Basin and Range province (Figure 2.1). The Basin and Range province is a broad region of extensional tectonism that began primarily in the Oligocene-Miocene (e.g., Wernicke, 1992), with significant deformation from the middle Miocene to the present in the western part of the province (Henry and Perkins, 2001, Wesnousky et al., 2005, Fosdick and Colgan, 2008). The Walker Lane is a belt of predominantly northwest-striking dextral faults that accommodate up to 25% of the relative motion between the Pacific and North American plates (Atwater and Stock, 1998; Bennet et al., 2003; Hammond et al., 2009). Walker Lane faulting began in the central and southern Walker Lane ~11-10 Ma but initiated somewhat later in the northern Walker Lane at ~4 Ma and has continued to the present-day (Faulds and Henry, 2008). The timing of deformation in the northern Walker Lane is broadly contemporaneous with the westward migration of Basin and Range deformation (Henry and Perkins, 2001; Surpless et al., 2002).

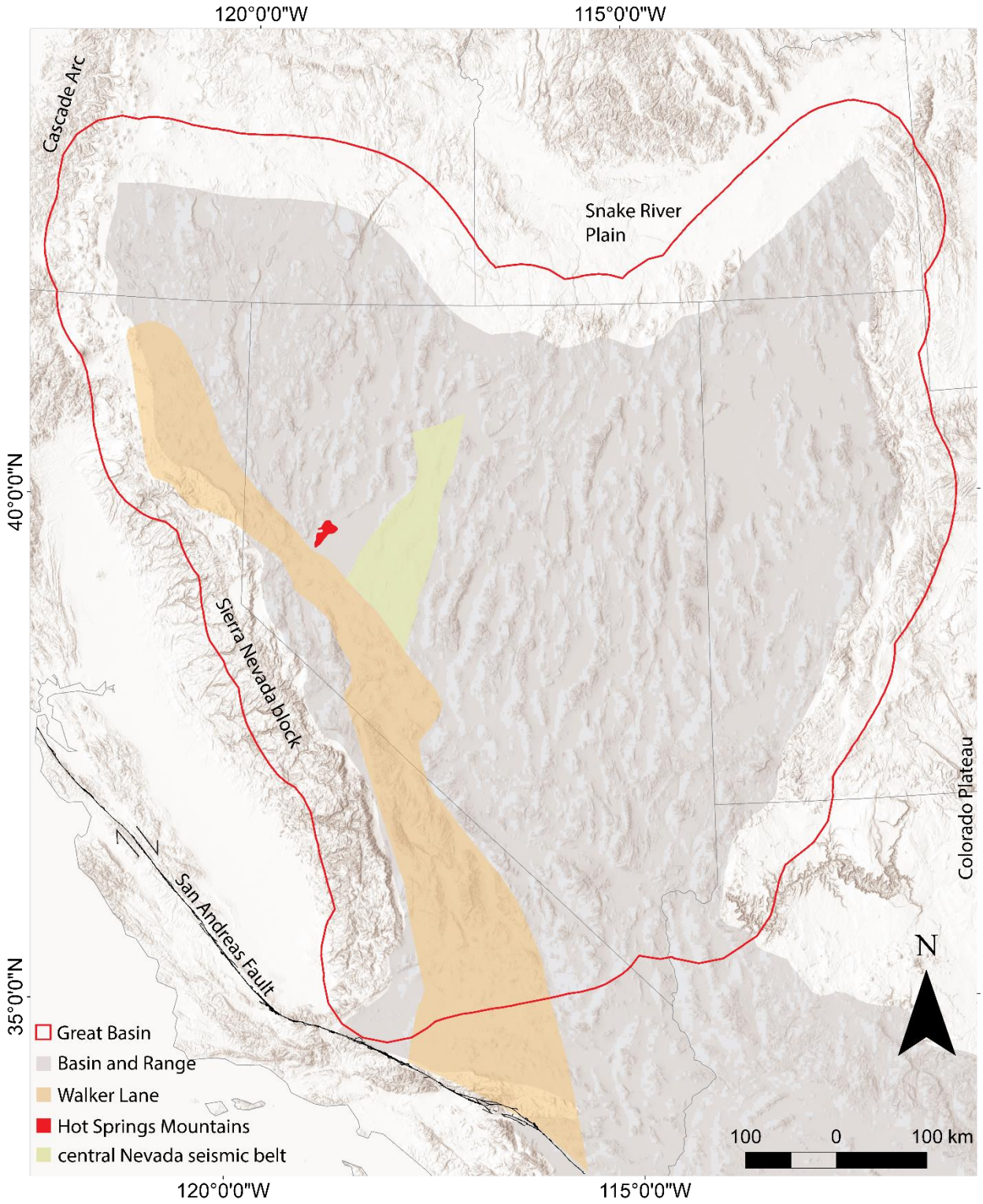

Figure 2.1. Regional tectonic map of western North America. Major structural domains discussed in text are highlighted and the boundary of the Great Basin hydrologic domain is outlined. Location of Hot Springs Mountains are colored red. Major tectonic features are annotated.

In the western Basin and Range province in the vicinity of the Hot Springs Mountains two studies are relevant for constraining the overall timing of extension. In the East Range ~100 km northeast of the northern Hot Springs Mountains (Fig. 2.2), thermochronological and geochronological data indicate a minimum of 40% extensional strain since 17-13 Ma (Fosdick and Colgan, 2008). Major faulting in the East Range began ~15 Ma, when much of the Basin and Range was extending. An additional phase of extension post 10 Ma has continued to the present in the East Range in a distinct younger episode of deformation. Pre-Cenozoic basement was exhumed in the footwall of the west-dipping normal fault system that accommodated the tilting and uplift of the East Range, and Quaternary fault scarps and hot springs indicate recent faulting along the western flank (Fosdick and Colgan, 2008). Within the Hot Springs Mountains, recent studies indicate a major episode of extension ~13-8 Ma, slightly later than that in the East Range, as evidenced by tilt fanning in half grabens and both tephrochronological and geochronological data (Faulds and Garside, 2003; Faulds et al., 2010, 2012). Similar to the East Range and much of western Nevada, widespread Quaternary fault scarps and hot springs and fumaroles in the Bradys area along the northwest flank of the Hot Springs Mountains demonstrate that extension has continued to the present (Faulds et al., 2010).

Although major pulses of extension occurred in the middle to late Miocene, abundant evidence demonstrates significant contemporary northwest-directed extension across the region. For example, fault trenching studies indicate that the Bradys fault zone, which bounds the northern Hot Springs Mountains on the northwest (Figure 1.4), has undergone at least one episode of Holocene normal displacement (Trevor and Wesnousky, 2001; Wesnousky et al., 2005). Historic earthquake ruptures along the

central Nevada seismic belt also document ongoing extension in the western Basin and Range (Caskey et al., 2004; Bell et al., 2004; Wesnousky et al., 2005). The central Nevada seismic belt loosely marks the transition from east-west extension in the eastern Basin and Range to more northwest-southeast extension to the west (Hammond and Thatcher, 2004, 2007). Additionally, contemporary geodetic strain rates show 2.8 ± 0.2 mm/yr of extension across the northern Basin and Range, with higher rates in the western portion that includes the northern Hot Springs Mountains (Thatcher et al., 1999; Bennett et al., 2003; Wesnousky et al., 2005). The increased GPS velocities west of the central Nevada seismic belt may result from the increased dilational strain related to the influence of dextral shear in the Walker Lane (Bennet et al., 2003; Hammond and Thatcher, 2007) and possibly to the transfer of some of that dextral shear into extension as the Walker Lane terminates northwestward (Faulds and Henry, 2008).

2.2 Desert Queen Geothermal Area

The Desert Queen geothermal area lies in the eastern part of the northern Hot Springs Mountains near the northwestern boundary of the Carson Sink. The study area encompasses ~200 km^2 (Figures 1.4 and 2.2). The eastern extent of the northernmost Hot Springs Mountains is bounded abruptly by the east-dipping Desert Queen normal fault. The Desert Queen basin lies in the hanging wall of the Desert Queen fault and takes up much of the northern portion of the study area and extends ~15-20 km to the north. The Desert Queen basin narrows to the south, ultimately terminating at Parran Mesa (Figure 1.4), which is a set of low-lying, flat-topped ridges that extend east and southeast of the

main portion of the northern Hot Springs Mountains. Parran Mesa is dissected down its center by a prominent fault, hereby referred to as the Power Line fault. Near the southern end of the study area, Parran Mesa ends abruptly southward giving way toa low-lying area that eventually grades into the Carson Sink to the southeast.

The Desert Queen geothermal area was named for the Desert Queen Mine, which is a long-abandoned lode gold mine with numerous adits, vertical shafts, and small dumps. The gold deposit lies within veins that cut a Mesozoic diorite unit, which is exposed in the footwall of the Desert Queen fault. Very little information exists about the Desert Queen Mine, but the resource was likely discovered in 1862 or 1863, and mining continued there until about 1900 (Bard et al., 1981).

In addition to the small mineral deposits at Desert Queen, abundant geothermal resources occur in the northern Hot Springs Mountains. Two commercial grade geothermal systems exist to the west of Desert Queen: Desert Peak and Bradys (Figure 1.4), which both host power producing plants. The Bradys system has been well known since the 19th century (Benoit et al., 1982). The many thermal features (hot springs, steam vents, fumaroles, etc.) at Bradys have made it an obvious target for geothermal production. The first formal development of Bradys was a spa in the 1940s. Additionally, in 1978, the first geothermal dehydration processing plant for vegetables in the world was installed and is still in use today (Benoit et al., 1982). However, commercial grade electricity production did not begin at Bradys until 1991 (Ettinger and Brugman, 1992). Desert Peak lies between Desert Queen and Bradys in a sand covered, southward sloping basin. It was discovered in 1976 by Phillips Petroleum Company as part of the reservoir assessment program of the Department of Energy (Benoit et al., 1982). Desert Peak, like

Desert Queen, is a blind geothermal system and is attributed as the first blind geothermal system discovered in the Basin and Range province (Benoit et al., 1982). Both the Desert Peak and Bradys geothermal systems are hosted along step overs in north-northeast-striking normal fault zones (Faulds et al., 2010). Desert Queen is also controlled by a north-northeast-striking normal fault system and has previously been attributed to the southward horse-tailing end of the Desert Queen fault zone (Faulds et al., 2010).

Much of the Desert Queen area has been previously mapped in earlier studies, starting in the 1960's by the Southern Pacific Railroad and followed by a master's thesis by Hiner (1982). However, a much more detailed geologic map of the area was later prepared by Faulds and Green (unpublished, 2009) and represents the most detailed mapping carried out in the area. It is a 1:24,000 scale map detailing bedrock units and Quaternary deposits. Part of this map was later incorporated into the published map of the Desert Peak quadrangle, which includes the westernmost part of the Desert Queen area (Faulds et al., 2012). A preliminary structural analysis was also carried out by Faulds and Green (2009), and much of this was published by Jolie et al. (2015). This analysis describes the inferred stress field inverted from fault kinematic data, including the local west-northwest-trending extension direction. This work established a thorough stratigraphic framework for Desert Queen. In addition, Magma Energy conducted detailed geophysical surveys of the area in ca. 2010, including gravity and MT surveys.

In addition to the previous geological and geophysical work, extensive exploration work has been completed at Desert Queen, such as temperature gradient drilling, 2 m temperature probe surveying, and preliminary geochemical analyses. The initial temperature gradient drilling was completed in the 1970s as an extension of the

Phillips Petroleum exploration program at the neighboring Desert Peak geothermal system (Benoit et al., 1982). Four additional temperature gradient wells were drilled in 2010 by Magma Energy, including the hottest well drilled in the area. A 2 m temperature probe survey was carried out across the Desert Queen basin in 2007 using general interpretations from the 1970s temperature gradient drilling as a guide (Benoit et al., 1982; Coolbaugh et al., 2007). Preliminary geochemical analyses were conducted at Desert Queen on thermal waters airlifted from the more recent temperature gradient wells (Benoit, unpublished data, 2010). These analyses were mostly used for comparative purposes in attempting to distinguish the Desert Queen geothermal system from the neighboring Desert Peak system. A partial geochemical analysis of non-thermal waters collected in artesian wells near the playa in the Desert Queen basin was also carried out (Garchar and Arehart, 2008). Geothermometry was conducted on all of the water samples to estimate potential reservoir temperatures.

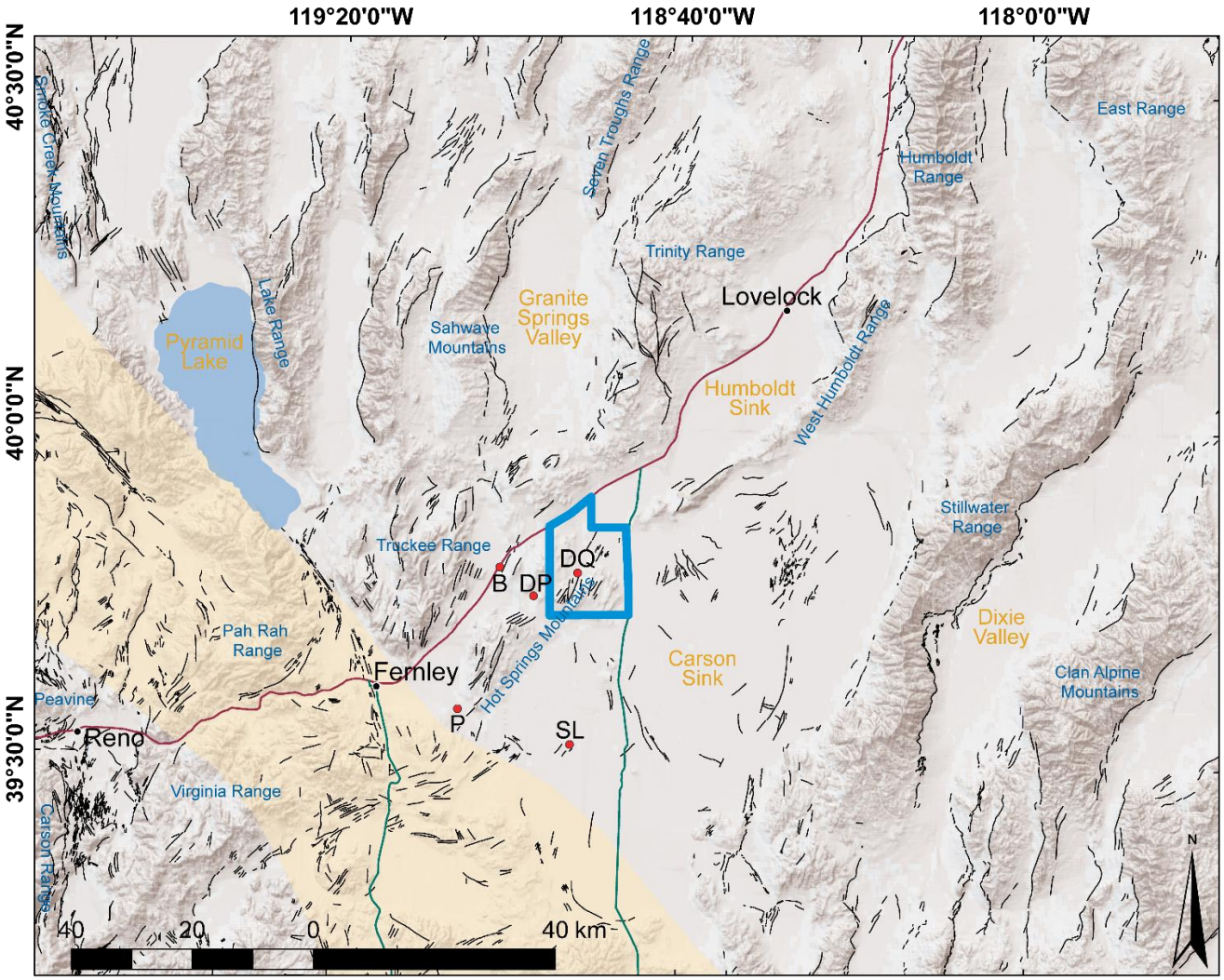

Figure 2.2. Regional map of northwestern Nevada. The Desert Queen study area is outlined in blue. Map is annotated with names of selected cities (black dots), some of the major mountain ranges (in blue text), and major valleys and basins (in orange text). Interstate 80 is shown in red, and Route 95 is shown in green. Approximate extent of the Walker Lane dextral shear zone is shaded in light orange. Narrow black lines mark Quaternary fault traces from the USGS fault and fold database (USGS, 2010) . Geothermal systems in the Hot Springs Mountains and vicinity are denoted with red dots as follows; Bradys (B), Desert Peak (DP), Desert Queen (DQ), Patua (P), and Soda Lake (SL).

2.2.1 Stratigraphic Framework

The stratigraphy at Desert Queen can be broken into three major groups:

Mesozoic basement, Tertiary volcanic and sedimentary rocks, and late Miocene -

Quaternary alluvial and surficial units (Figure 2.2.1). These groups are summarized here, but more detailed relationships can be found on the accompanying geologic map (Plate 1). Mesozoic basement crops out in the footwall of the Desert Queen fault in the northwest part of the study area and consists of a 102 Ma diorite pluton based on new U/Pb zircon dating from this study (Appendix A, Table A1). The diorite unit has an unknown extent in the subsurface and is the only exposed Mesozoic basement in the northern Hot Springs Mountains.

Resting noncomformably atop the Mesozoic rocks is a 2-3 km thick Tertiary section of mixed rock types. Mostly Miocene strata are exposed, but Oligocene ash-flow tuff units have been observed in core from the 35-13 well (Figure 2.2.2). Additionally, an altered sedimentary unit of possible Eocene to Oligocene age (based on new detrial zircon data from this study-Appendix A, Table A2) is exposed at Cinnabar Hill in the footwall of the Desert Queen fault, adjacent to the Cretaceous diorite. The total thickness of the altered sedimentary unit is unknown, but ~120 m is exposed directly west of the Desert Queen fault. The Miocene section consists of laterally interfingering volcanic and sedimentary units. This section is divided into 5-6 distinct sequences as follows from oldest to youngest: 1) lower sequence of Miocene andesite, dacite, and rhyolite lavas and subordinate rhyolitic to dacitic ash-flow tuffs ranging from ~16 to 13 Ma; 2) complex section of dominantly aphanitic basalt lavas, but with intercalated sequences of white siltstone, diatomite, and tuffaceous sedimentary rocks ranging from ~13 to 10 Ma; this sequence contains units that likely correlate to the Chloropagus Formation of Axelrod (1956), but this name has generally been discarded due to many local volcanic centers and isolated basins leading to significant variations in composition and thickness (e.g.,

Benoit et al., 1982; Faulds et al., 2012); 3) sequence of dominantly sedimentary rocks (mainly diatomite and tuffaceous siltstone) and lesser olivine basalt flows ranging from ~12 to 10 Ma; this predominantly sedimentary sequence contains many members of the Miocene Truckee Formation of Axelrod (1956) and further described by Stewart and Perkins (1999), but the Truckee Formation is generally no longer used due to deposition in many isolated basins (e.g., Trexler et al., 2000); 4) ~10-9 Ma limestone unit that pinches out eastward and interfingers with the upper part of the 12-10 Ma sequence; 5) olivine basalt flows and porphyritic dacite domes and flows cropping out mostly in the eastern part of Parran Mesa; and 6) a dacitic ash-flow tuff that is the youngest volcanic unit in the area, forms a resistant cap atop Parran Mesa, and is conspicuous in most of the study area south and east of the Desert Queen fault; it has yielded a 7.46 ± 0.31 Ma $^{40}Ar/^{39}Ar$ date (Faulds and Green, unpublished data, 2009). The capping tuff likely underlies much of the Desert Queen basin, as evidenced by small outcrops of the unit along the western edge of the basin in the hanging wall of the Desert Queen fault. Notably, the Miocene sedimentary units crop out more extensively in the western part of the area, as they likely thin and possibly pinch out toward the east. Conversely, the upper olivine basalt and porphyritic dacite units that dominate the eastern extent of the area along Parran Mesa appear to thin toward the west (Figure 2.2.2). The ages of many of these stratigraphic units are bracketed by tephras that are common throughout the late Miocene section, facilitating correlation of these units via tephrochronology (Stewart and Perkins, 1999; Perkins and Nash, 2002; Faulds and Green, unpublished data, 2009; Faulds et al., 2012).

Late Miocene to Pleistocene alluvial sediments are found throughout the area and likely largely fill the relatively broad Desert Queen basin to ~600 m depth, as evidenced by gravity data. Quaternary sediments comprise the surface of the Desert Queen basin and are dominated by Pleistocene Lake Lahontan sediments. The oldest lacustrine deposits in the area accumulated in the Sehoo cycle, when the high stand of Lake Lahontan reached an elevation of 1330 m ~13 ka (Adams and Wesnousky, 1999). Many of the bedrock units in the area were therefore submerged and are commonly coated by shoreline tufa deposits, making them hard to distinguish at a distance. Abundant well preserved lacustrine beach berms and bars are found throughout the area (Plate 1) above and within the margins of the Desert Queen basin marking the retreat of Pleistocene Lake Lahontan. Lacustrine deposits vary, but generally consist of sand, silt, and mud in low lying areas below alluvial and beach deposits. Additionally, many small playas have formed on the uphill sides of beach berms. In the northwest portion of the area, where the Desert Queen basin widens to the north-northeast, abundant and lengthy beach berm deposits (up to km in scale) are commonly topped with large tufa towers (up to 10 m tall in some cases).

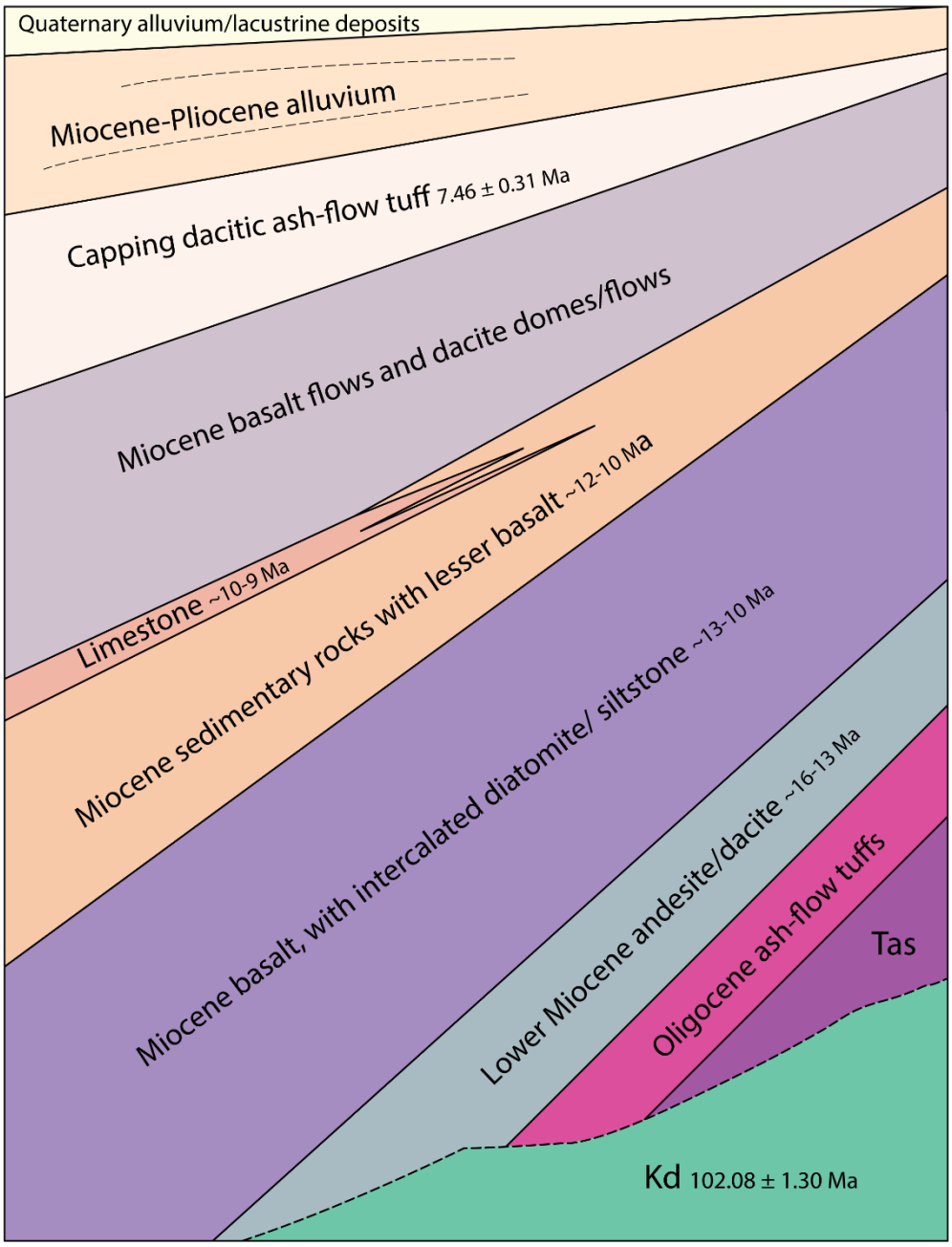

Figure 2.2.1. Generalized stratigraphic column of major units and packages of units in the Desert Queen area. The column is not to scale; however, relative thicknesses are shown. Dashed line is the Tertiary nonconformity. Column schematically portrays decrease in tilt up section. Age of units are listed where known and approximated. Kd is Cretaceous diorite, and Tas is lower altered Tertiary sedimentary rocks. Unit packages denoted in this figure contain anywhere from 2 to >12 individually mapped units (Plate 1).

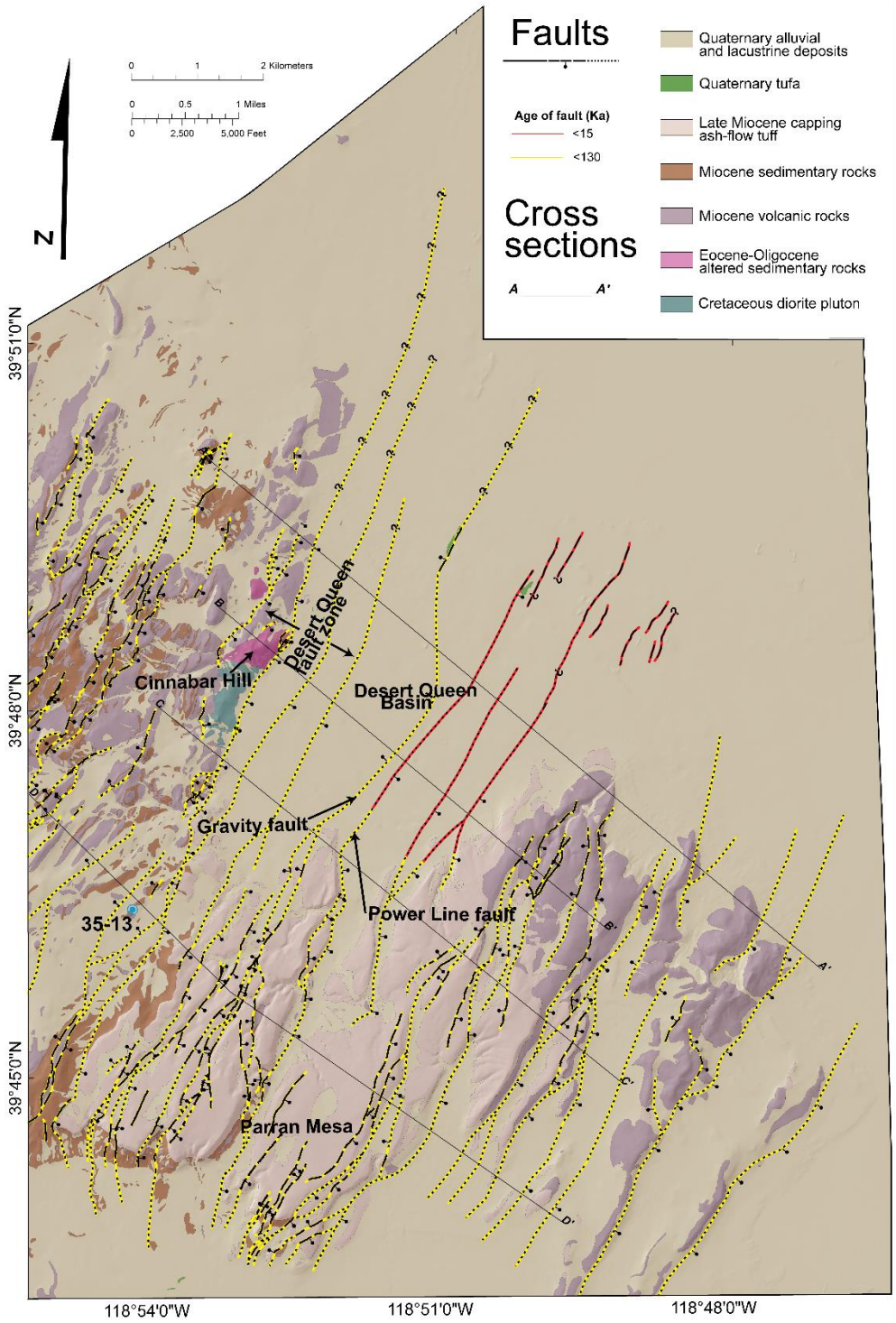

Figure 2.2.2. Simplified geologic map of the Desert Queen study area. Faults are shown with solid, dashed, and dotted black lines (certain, approximate, and concealed traces, respectively) with balls on down dropped sides, and attributed with fault recency. Locations of cross sections are labeled with thick red lines. Geologic units were consolidated into 7 major units as annotated on map and described in text. Major faults, features, and wells discussed in text are annotated.

2.2.2 Structural Framework

Tertiary normal faults are the primary structural features in the Desert Queen area compatible with the northern Hot Springs Mountains lying within the Basin and Range province and the dominant exposures of Miocene strata (as opposed to older units). The area consists of many gently to moderately tilted fault blocks cut by relatively closely spaced moderately to steeply dipping (50-80°), north-northeast-striking normal faults (e.g., Faulds and Green, 2009; Faulds et al., 2010, 2012). Both east- and west-tilted fault blocks characterize the area and reflect west- and east-dipping normal fault systems, respectively. However, the Desert Queen area is dominated by west-tilted fault blocks that are cut by east-dipping normal faults (Figure 2.2.3). The predominant north-northeast-striking bedding and layering in the area reflects the prominent strike of normal faults.

The most prominent structure in the area is the north-northeast striking Desert Queen fault zone, which accommodates up to 2 km of normal offset in the northern part of the study area, where Quaternary sediments and Tertiary rocks are juxtaposed against Mesozoic basement. The Desert Queen fault zone consists of at least four major strands; one directly west of the range front, one defining the range front, and two poorly exposed strands basinward of the range front (Figure 2.2.2). The Desert Queen basin is a complex west-tilted half graben developed in the hanging wall of the Desert Queen fault. Gravity data suggest an antithetic west-dipping fault within the basin, hereby referred to as the Gravity fault, which defines a narrow graben within the broader half graben (Figure 2.2.2 and 2.2.3). Offset along the Desert Queen fault zone decreases to the south toward the southern end of the basin. The Desert Queen fault zone breaks into multiple fault strands,

as it terminates toward the southern end of Parran Mesa.

Parran Mesa is broken into many small horst and graben blocks by faults that accommodated much less displacement (100's of meters) than the main segment of the Desert Queen fault zone. Relatively minor normal faults that dip both west and east dissect Parran Mesa and generate several extensional anticlines and synclines (Plate 1), as the tilt direction of fault blocks varies according to the dominant dip direction of bounding normal faults (e.g., Faulds and Varga, 1998). The narrow valley through the middle of Parran Mesa is bounded by the Power Line fault, a conspicuous east-dipping normal fault (Figure 2.2.2). The Power Line fault projects northeast into the Desert Queen basin and closely parallels the Gravity fault in the basin. The Power Line fault bisects Parran Mesa to the south, where the southern end of Parran Mesa ends abruptly with a steep east-trending escarpment (perpendicular to the trend of the Desert Queen fault zone). South of this escarpment the Power Line fault, as well as the many minor faults that break up Parran Mesa, are concealed by Quaternary units.

Interestingly, three Quaternary tufa mounds, which contain small silica nodules (Faulds and Green, 2009), crop out near the trace of the Power Line fault near the southern end of Parran Mesa. The tufa outcrops are of interest because of their spatial correlation with the Power Line fault and the presence of the silica nodules. Tufa columns such as these can indicate past thermal spring activity and may also provide evidence for ongoing geothermal activity hidden beneath the surface (Coolbaugh et al., 2009).

Although some short length faults and lineaments appear to cut the late Pleistocene Lake Lahontan sediments in the Desert Queen basin, Quaternary fault scarps

are generally hard to distinguish in the area. Many young fault scarps are likely obscured by the thin cover of late Pleistocene and Holocene lacustrine and eolian sediments in the Desert Queen basin (Faulds and Green, 2009).

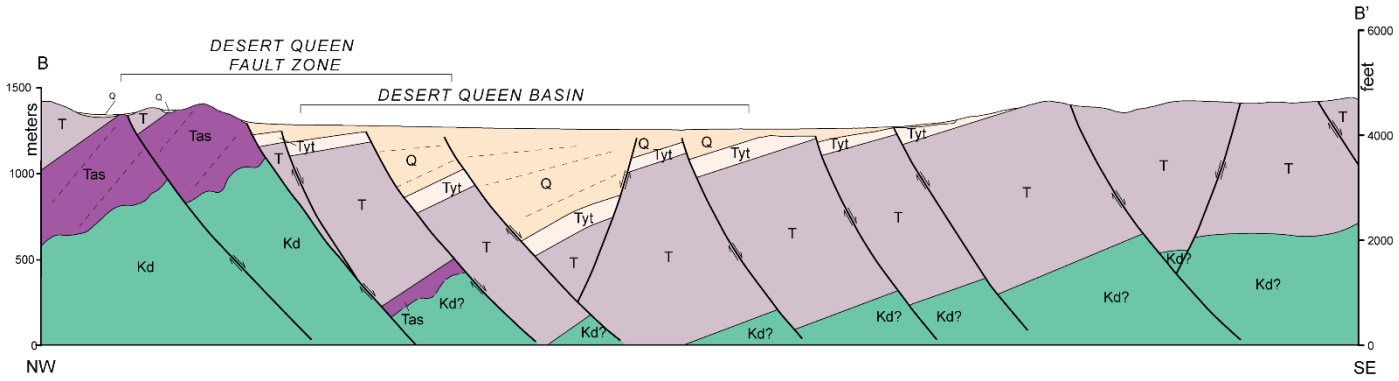

Figure 2.2.3. Simplified cross section across the Desert Queen fault zone and Desert Queen basin Section corresponds to A-A' on Figure 2.2.2. Units are as follows: Q: Quaternary deposits, Tyt: late Miocene capping tuff, T: Tertiary (Miocene) sedimentary and volcanic rocks, Tas: Eocene-Oligocene altered sedimentary rocks, Kd: Cretaceous diorite pluton. Tertiary rocks are lumped into two units to demonstrate general stratigraphic and structural framework.

3. Methods and Results

Geologic methods at Desert Queen were carried out over an ~200 km^2 area bounded by the adjacent Desert Peak area, Interstate 80, Route 95, and the Carson Sink (Figure 2.2). Methods included detailed 1:24,000 scale geologic mapping of both bedrock and Quaternary units, fracture analysis of potential reservoir rock, and targeted geochronology.

3.1.1 Detailed Geologic Mapping

A 1:24,000 scale detailed geologic map was compiled and finalized over the entire ~200 km^2 area (Plate 1). The preliminary geologic map of Desert Queen and associated geodatabase by Faulds and Green (2009) served as a baseline for the mapping in this study. Faulds and Green (2009) completed ~75% of the area, with the remaining

25% accomplished in this study. With the additional geophysical datasets and modeling, previous mapping was rectified and updated where necessary. Field mapping was carried out using a combination of color stereo air photos, topographic maps, and supplemented using FieldMOVE software. Completion of the geologic map allowed for the generation of two new cross sections, as well as updating two cross sections originally produced by Faulds and Green (2009) (Plate 1).

Detailed Quaternary mapping was critical for evaluating geothermal activity in the area, as most higher temperature geothermal systems in the Great Basin region are associated with Quaternary faulting (Bell and Ramelli, 2007). Alluvial deposits were distinguished based on numerous characteristics, including relative elevation, degree of weathering, channel incision, degree of rounding, and development of desert varnish. Younger alluvial surfaces tend to be less incised, less rounded, and lower elevation than older surfaces. In general, most of the surficial Quaternary deposits at Desert Queen consist of Pleistocene Lake Lahontan sediments, as well as Holocene eolian sand deposits. Faulds and Green (2009) determined that most of the Lahontan sediments above the present-day Humboldt Lake bottom were part of the Sehoo formation dated at 13,110 ± 110 yr B.P. (Adams and Wesnousky, 1999), adding age constraints to faults that cut these units. Minor units within this formation were largely left undivided; however abundant beach berm deposits commonly associated with large shoreline tufa towers were mapped throughout the area. Fault scarps can also be used to determine relative ages of Quaternary deposits, but no prominent fault scarps were observed in the Desert Queen area. Some Quaternary faults were inferred in the Desert Queen basin based on minor lineaments observed in aerial imagery, but the bulk of the concealed faults within

the basin were mapped with the aid of geophysical data. Additionally, locations of faults from the USGS fault and fold database (USGS, 2010) were assessed and compared with fault traces mapped in the Desert Queen basin.

Detailed bedrock mapping was carried out to delineate the stratigraphic and structural framework of the area. Knowledge of the stratigraphy was important for constraining the traces of faults, both within the exposures of bedrock and extrapolating into the basins. Detailed mapping of faults also aided in identifying favorable structural settings (e.g., Faulds et al., 2011, 2021; Faulds and Hinz, 2021) (Figure 1.2) capable of controlling geothermal fluid flow.

The age of Quaternary faults was based on the age of most recent rupture and included data from Phase I of the Nevada play fairway project (Faulds et al., 2016) (Figure 2.2.2). Most of the faults within the area are presumed to be >15 ka, as fault scarps within surficial units are either nonexistent or covered by Pleistocene (<~15 ka) Lake Lahontan lacustrine sediments. Some small fault segments in the Desert Queen basin that cut Lahontan units are accordingly attributed as younger than 15 ka (Figure 2.2.2). Fault slip rates were also assigned based on the regional data set used in Phase I of the Nevada play fairway project (Faulds et al., 2016). However, due to the lack of both Quaternary fault scarps in the area and any new data to shed light on fault slip rates, all of the fault segments at Desert Queen were assigned a general, conservative slip rate of 0.01 mm/yr.

3.1.2 Targeted Geochronology

Samples from the presumed Mesozoic basement in the footwall of the Desert

Queen fault were collected for U-Pb dating of zircons to better constrain the age and structural character of these units. The highly jointed diorite represents a possible geothermal reservoir rock at depth, and thus it is important to understand its stratigraphic and structural relationships. The diorite intrusion is juxtaposed against hydrothermally altered sedimentary rocks also exposed in the footwall of the Desert Queen fault. Three bulk samples (~7 kg total) were collected from the altered sedimentary units at different stratigraphic intervals to account for any lithologic variations within the unit. Two representative bulk samples (~10 kg total) were collected on the least altered exposures of the diorite. Samples were packaged and sent to the University of Arizona Laserchron lab for preparation, imaging, and analysis. Zircons used in the analysis were first imaged with back scatter electron (BSE) and cathodoluminescence (CL) imaging techniques to identify inherited cores and/or younger overgrowths (e.g., Gehrels et al., 2008).

The diorite was dated using a standard U-Pb LA-ICPMS method outlined in Gehrels et al. (2008). The data were filtered to include analyses that were between 80 – 105% concordant (Figure 3.1.1C). The weighted mean age from the concordant analyses is 101.8 ± 0.5 Ma. The Cretaceous age for the diorite differs from the inferred Jurassic age in earlier studies (Faulds et al., 2012).

The altered sedimentary unit was dated using a similar U-Pb LA-ICPMS method following the detrital zircon method outlined in Gehrels and Pecha (2014). U-Pb detrital zircon dating has been commonly employed since the early 2000s (e.g., Rainbird et al., 2001; Stewart et al., 2001; Surpless et al., 2006) and was applied to the altered sedimentary unit to constrain its depositional age (e.g., Gehrels et al., 2000; Linde et al., 2016; Lawton et al., 2017). Detrital zircon geochronology has been proven to be a viable

method for determining maximum depositional ages using the youngest detrital zircon grains in a population (Davis et al., 2003; Brown and Gehrels, 2007; Dickinson and Gehrels, 2009). Maximum depositional ages were constrained using the youngest concordant grains from all three altered sedimentary samples (Dickinson and Gehrels, 2009). Analyses were filtered to include only grains between 70 – 105% concordance. The largest population of detrital grains are late Cretaceous, and the weighted mean of the youngest three concordant ages is 104.3 ± 0.5 Ma (Figure 3.1.1A,B). Both of these analyses show that the altered sedimentary unit is at least younger than ~104 Ma. The youngest concordant grain is 97 Ma, further constraining the maximum depositional age to late Cretaceous. The abundance of late Cretaceous grains in the altered sedimentary unit similar in age to the adjacent diorite suggests that the diorite and related intrusions were a significant source of detritus in the sedimentary sequence. Furthermore, rough concordance of the attitude of this sedimentary unit with the lower part of the Miocene section (Plate 1) indicates the possibility of a younger Paleocene – Eocene age.

Locations of dated bulk samples and their associated ages can be found on the inset map on Plate 1. Complete geochronological data are presented in Appendix A (Table A1 and A2).

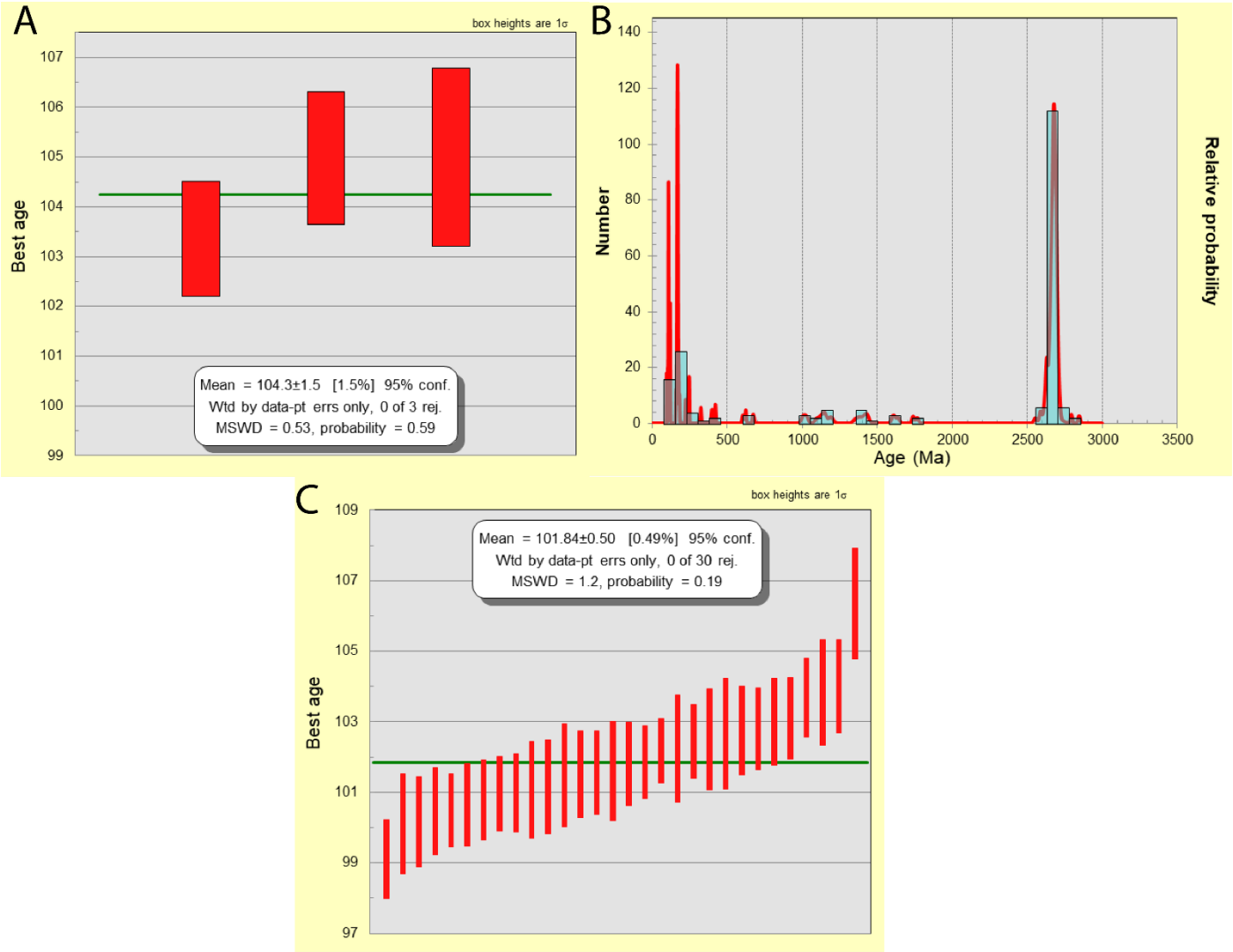

Figure 3.1.1. A) Weighted mean plot of youngest three concordant detrital zircon ages for the altered sequence of sedimentary rocks. **B)** Relative probability plot of the full spectra of concordant detrital zircon data for the altered sedimentary sequence. **C)** Weighted mean plot of 30 concordant analyses from the diorite pluton samples.

Additional dating techniques were previously employed (Faulds and Green, 2009; Faulds et al., 2012, 2017) to bracket the ages of the Miocene stratigraphic section. Abundant tephras facilitated dating of most of the Miocene units. Tephrochronology (e.g. Stewart and Perkins, 1999; Perkins and Nash, 2002; Faulds et al., 2012) was conducted by Mike Perkins at the University of Utah in 2009 on multiple samples in the area. In addition, $^{40}Ar/^{39}Ar$ dates were obtained for several key volcanic units in the northern Hot

Springs Mountains (Faulds et al., 2012). For example, the young capping ash-flow tuff that dominates much of the area yielded an $^{40}Ar/^{39}Ar$ date of 7.46 ±0.31 Ma. This ash-flow tuff is one of the youngest volcanic tuff exposures in the region (J. Faulds personal communication, 2019). The results from these dates helped to correlate units across the study area (Figure 2.2.1).

3.2 Structural Analysis

3.2.1 Geometry of Faults and Structural Blocks

The attitudes of bedding, layering, faults, and joints were measured to define the structural framework of the Desert Queen area. Bedding and layering attitudes demonstrate that the area is characterized by north-northeast-trending, gently to moderately west-tilted fault blocks bounded by east-dipping normal faults. Bedding and layering attitudes average 034^{o} in strike and 38^{o} in dip, with a progressive decrease up section in dip from ~50^{o} to ~10^{o} (Figure 3.2.1). Strata mostly dip to the west, but minor antithetic west-dipping faults bound some east-dipping fault blocks.

Faults surfaces measured in the area mainly strike north to northeast (~0-45°) and dip moderately (average 64°) (Figure 3.2.2). The major fault within the area is the Desert Queen fault zone. It consists of several poorly exposed strands, as well as at least 2 major strands concealed within the Desert Queen basin. Only one exposure of the Desert Queen fault zone has been observed, and it strikes 003^{o} and dips 74^{o} east. Other strands of the fault are inferred to dip moderately to steeply (50^{o} to 80^{o} +).

Joints were measured in the Cretaceous diorite unit (Figure 3.2.3) to constrain the structural character of a potential reservoir within the Desert Queen geothermal system.

These data were used to carry out a simple fracture analysis of this unit. The joints dip steeply and generally strike northerly (N20^{o}W to N20^{o}E), with a significant subset striking northeast (Figure 3.2.4) Thus, the joints are generally oriented orthogonal to the west-northwest-trending extension direction (Bennett et al., 2003) and least principal stress (Jolie et al., 2015). Therefore, the majority of fractures within the diorite are favorably oriented in the present stress field to allow for enhanced permeability.

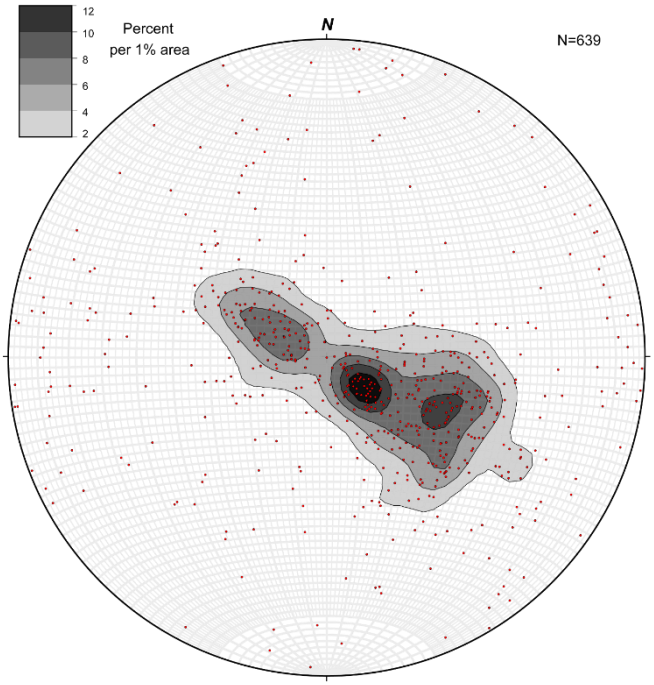

Figure 3.2.1. Equal-area stereographic projection of poles to bedding and layering in the Desert Queen study area. Data points shown by red dots. Clusters indicate that NNE strikes and gentle to moderate west-northwest and east-southeast dips prevail. N=number of data points.

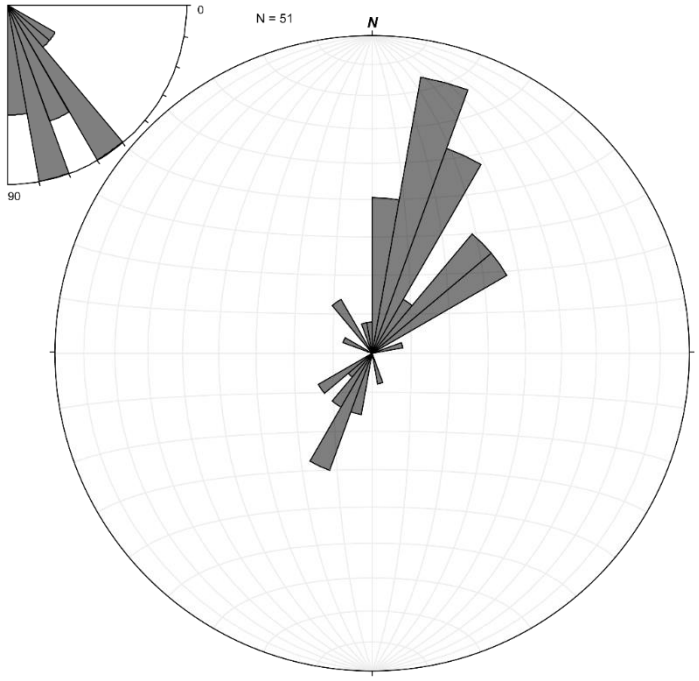

Figure 3.2.2. Rose diagram and associated dip histogram generated from measured fault planes in the northern Hot Springs Mountains. Data are binned in intervals of 10°. Main rose diagram is plotted on lower hemisphere stereographic projection.

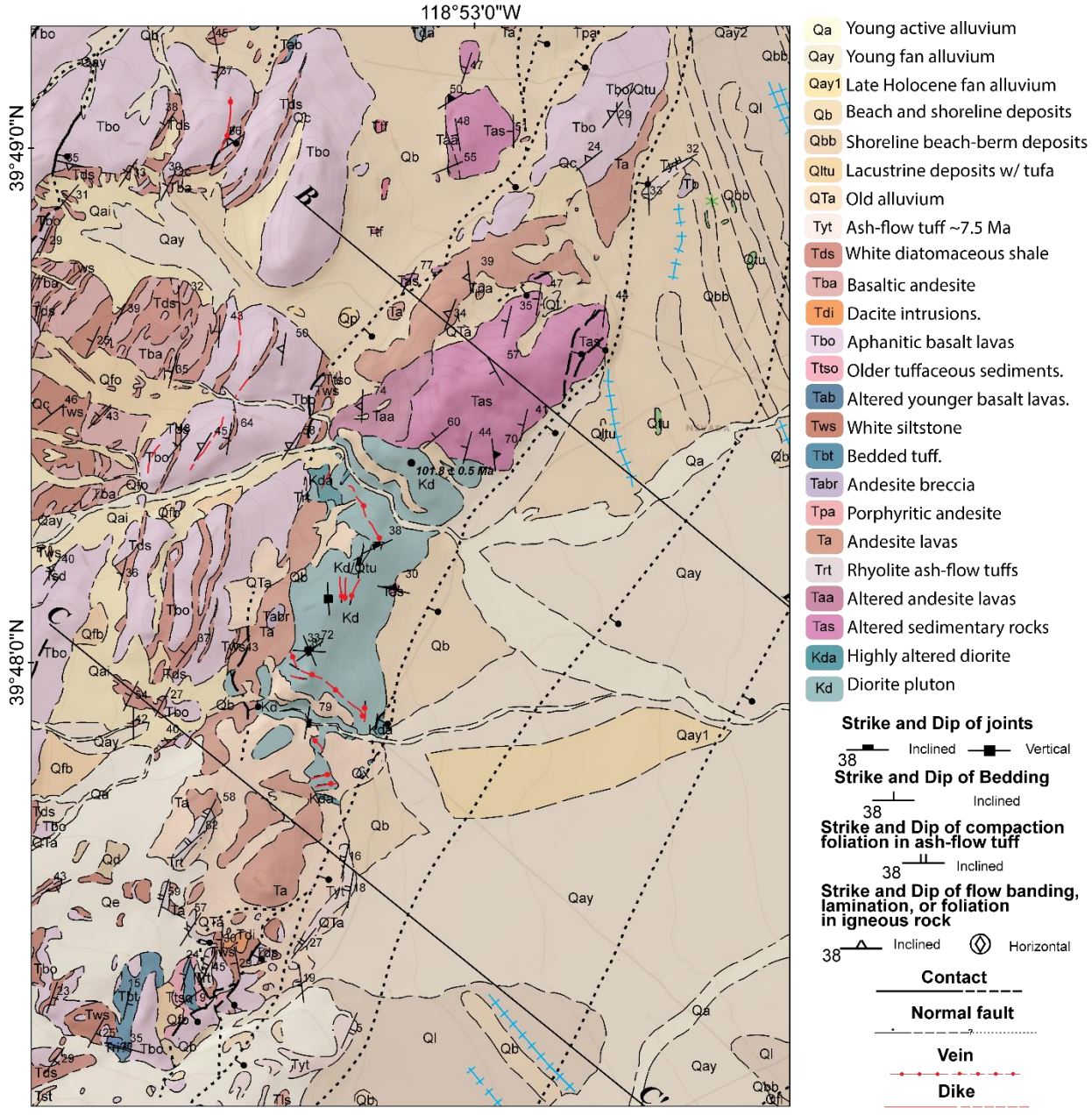

Figure 3.2.3. Detailed geologic map inset highlighting extent of fractured diorite pluton unit (Kd). Map shows the spatial extent of all joint measurements used in the fracture analysis of the diorite. Map also demonstrates the level of detailed mapping for the entire study area.

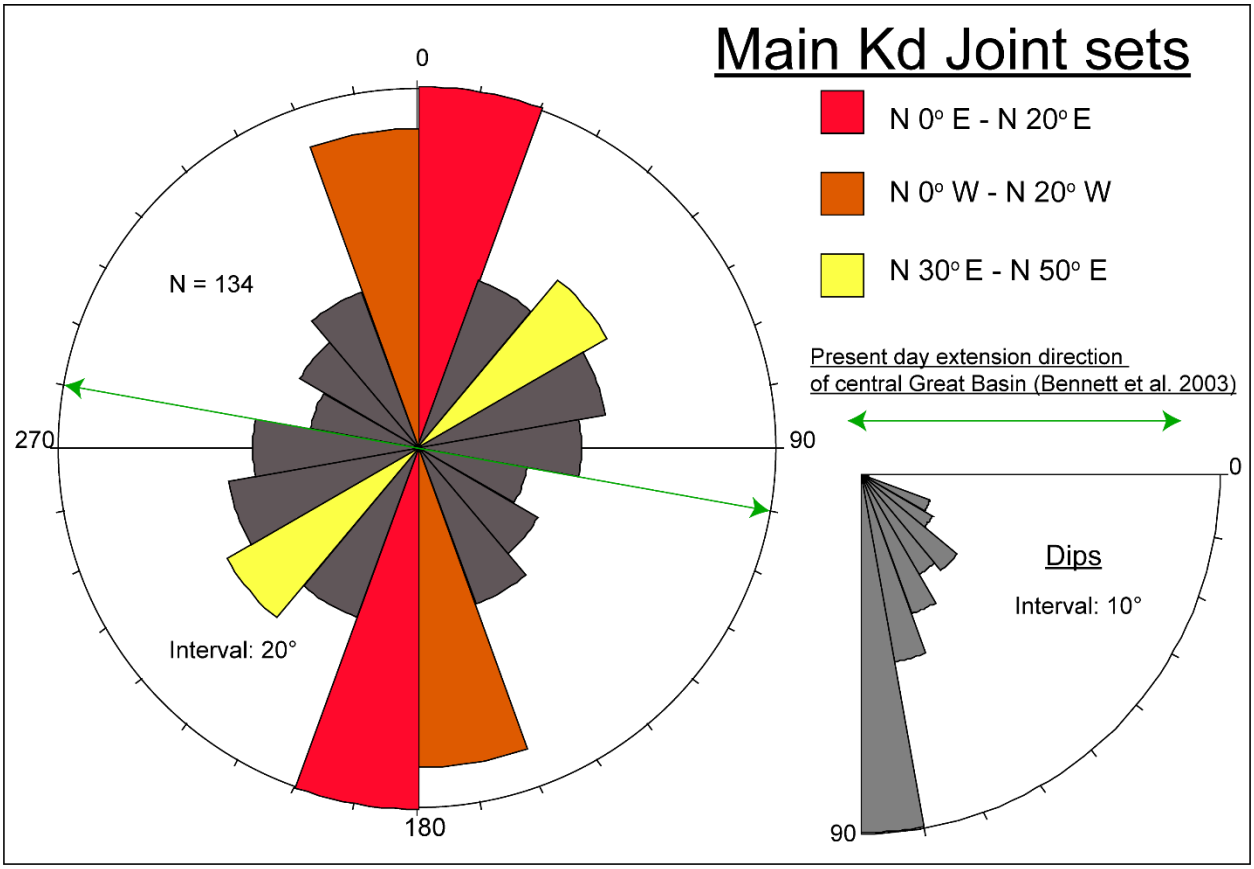

Figure 3.2.4. Rose diagram of joint attitudes from the basement diorite relative to present day extension direction (Bennet et al., 2003). (a) Strikes of joints; three main joint sets are highlighted in color. (b) Bottom right shows joint dips.

3.2.2 Kinematic Analysis and Stress Inversion

Building on the existing dataset generated by Faulds (unpublished data, 2009, 2017) and partially published in Jolie et al. (2015), the previously completed structural analysis was expanded to include all available kinematic data from the northern Hot Springs Mountains (Figure 3.2.5) (Appendix B, Table B1). This more regional dataset allowed for greater certainty in constraining the stress field, as a limited number of kinematic data points were collected in the Desert Queen area. On first order, displacement sense on faults was identified by stratigraphic offset. Attitudes of bedding/layering proximal to the faults and kinematic indicators (e.g., fault striae,

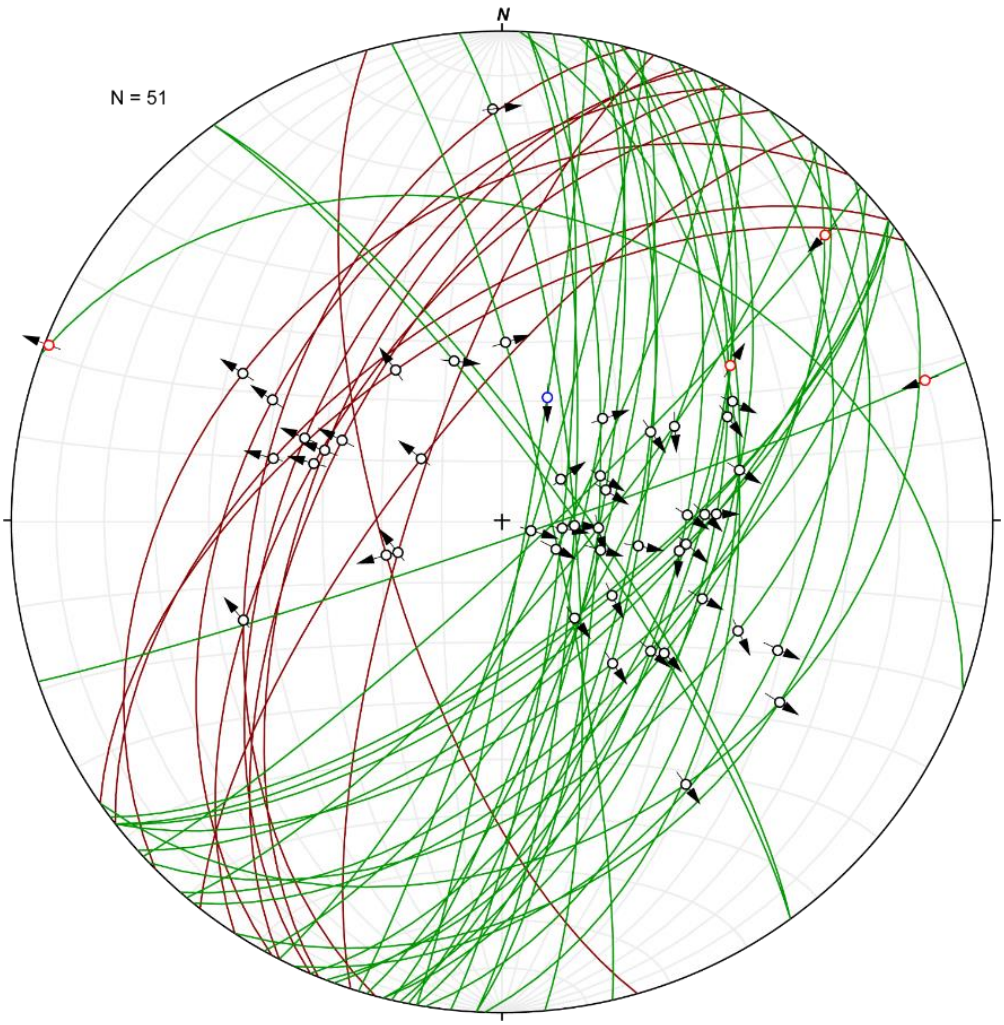

Figure 3.2.5. Lower hemisphere equal-area stereographic projection showing great circles of measured fault planes in the northern Hot Springs Mountains. Data are compiled from Faulds (unpublished data, 2009, 2017) and Jolie et al. (2015). Green planes dip eastward, and red planes dip westward. Orientation of slip directions inferred from kinematic indicators are shown with black arrows and color coded as follows: Black outlines = predominantly normal slip; red outlines = predominantly sinistral slip; blue outlines = predominantly dextral slip. N= number of measurements. Figure demonstrates that the majority of faults in the area strike north-northeast, dip east-southeast, and primarily accommodated normal slip.

corrugations, Riedel shears, and rough facets) on any exposed fault surfaces were measured to constrain sense of slip (e.g., Angelier et al., 1985; Petit, 1987). Fault striations and corrugations only indicate the general slip character (e.g., strike-slip vs. vertical offset) but do not constrain the actual sense of slip (e.g., right- vs. left-lateral or normal vs. reverse slip). Therefore, striations must be used in conjunction with other

features, such as rough facets (also referred to as chatter marks) or Riedel shears to determine the sense of slip (Angelier et al., 1985; Allmendinger, 1989)

Given that the structural data collected on minor faults are consistent and representative of the broader strain and stress fields, the principal extension and shortening axes can be constrained (Marrett and Allmendinger, 1990). Adopting the assumptions outlined by Marrett and Allmendinger (1990), TectonicsFP software was used to model the strain axes (Ortner et al., 2002). These strain axes were inverted using the same software to determine the principal compressive stresses (σ_1, σ_2, σ_3), where σ_1 and σ_3 are the maximum and minimum compressive stresses, respectively. This stress inversion analysis allowed for the determination of the stress field and was the main input parameter used in the slip and dilation tendency analyses.

The principle compressive stress directions calculated in the inversion are as follows: P (contraction axis or maximum compressive stress, σ_1) = 232° / 80 (trend/plunge), B (neutral axis or intermediate compressive stress, σ_2) = 025° / 09, and T (extension axis or least compressive stress, σ_3) = 116° / 04 (Figure 3.2.6). These values, particularly the least compressive stress axis (i.e., the general extension direction), are in good agreement with borehole breakout investigations completed at the Desert Peak geothermal field (Hickman and Davatzes, 2010).

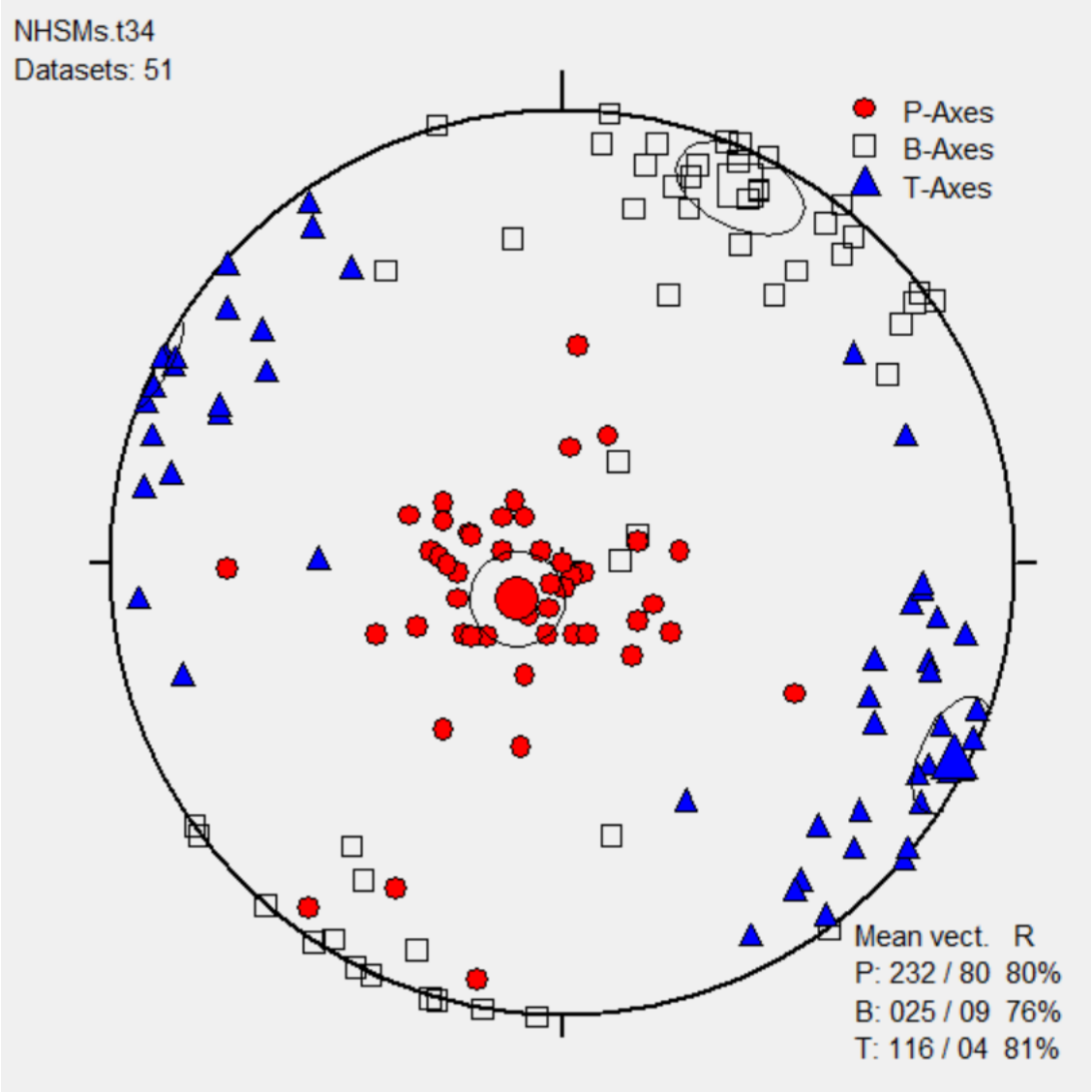

Figure 3.2.6. Lower hemisphere stereographic projection displaying stress directions calculated from kinematic data in the northern Hot Springs Mountains. Red circles indicate the compressive axis (P), white squares indicate the intermediate axis (B), and blue triangles indicate tension axis (T).

3.2.3 Slip and Dilation Tendency Analyses

Slip and dilation tendency analyses techniques were carried out by applying the resolved stress field to the known faults in the area. Slip and dilation tendency analyses can identify faults or fault segments that are critically stressed. Critically stressed fault segments are more likely to slip or dilate. Such faults are most likely to reactivate based

on their orientation in relation to the local stress field and are also more likely to transmit geothermal fluids (Morris et al., 1996; Ferrill et al., 1999; Ferrill and Morris, 2003; Moeck et al., 2009). The presence of damage zones along recently active fault segments serves to increase permeability, which is also critical in transmitting fluids in the crust (Caine et al., 1996; Micklethwaite and Cox, 2004; Moeck et al., 2009). The tendency of a fault surface to slip is controlled by the ratio of shear to normal stress acting on the surface. Given by: $Ts = \tau/\sigma_n$, where Ts is the slip tendency, τ is the resolved shear stress, and σ_n is the resolved normal stress (Morris et al., 1996). The tendency of a fault surface to dilate is controlled by the magnitude and direction of the principal stresses relative to the fault plane. Given by: $TD= (\sigma_1-\sigma_n)/(\sigma_1-\sigma_3)$, where TD is the dilation tendency, σ_1 is the maximum principal compressive stress, σ_3 is the minimum principal compressive stress, and σ_n is the resolved normal stress (Ferrill et al., 1999).

The dilation tendency and slip tendency alone are useful in identifying fault segments that are optimally oriented to transmit geothermal fluids. It has been shown that fault segments with high dilational tendency and comparatively low to high slip tendency are more likely to experience a “hybrid” failure consistent with volume gain (Ferrill et al., 2019). Therefore, in order to fully understand the behavior of critically stressed faults, maximum slip and dilation tendency must be compared in cross plot space (Ferrill et al., 2020). This comparison allows for delineation of fault segments most likely to experience hybrid failure and thus positive dilation (Ferrill et al., 2019) (Figure 3.2.7).

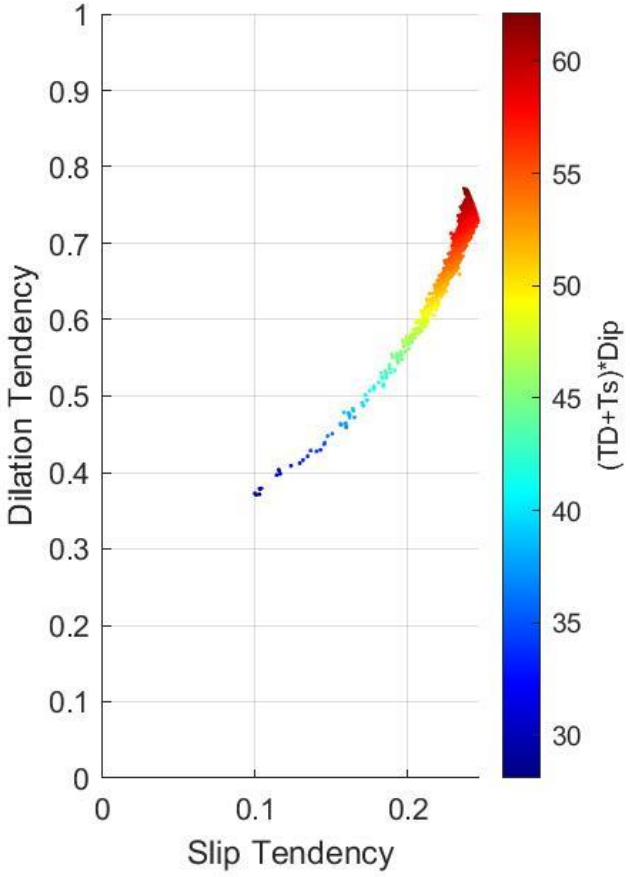

Figure 3.2.7. Cross plot of dilation tendency vs. slip tendency. Values in the red zone fall within the zone consistent with "hybrid" failure according to Ferrill et al. (2020).

The slip and dilation tendency analyses were carried out using a preexisting MATLAB code provided by Drew Siler (USGS) and populated with parameters specific to Desert Queen. Stress magnitudes and orientations used in the analysis were a combination of regionally available data and the local stress field derived for Desert Queen from kinematic fault data. The stress magnitudes used were S_v (σ_1) = 22.6 MPa, S_{hmin} (σ_3) = 13.7 MPa, and S_{hmax} (σ_2) = 18.2 MPa (Hickman and Davatzes, 2010). These data are derived from borehole breakout investigations in well 27-15 at 930 m depth in the nearby Desert Peak geothermal field (Hickman and Davatzes, 2010). The stress

orientations used were S_v = 232°, S_{hmin} = 116°, and S_{hmax} = 25°, as calculated from the inversion of fault kinematic data. All faults were assumed to have normal motion and were assigned dip values of 60°. Due to this assumption, the plunge associated with each stress axis was assumed to be 0° for σ_2 and σ_3, and 90° for σ_1 for this normal faulting stress regime in accordance with Andersonian fault theory (Anderson, 1951). Fault segments were assigned separate values of dilation tendency (Td) and slip tendency (Ts). They were also further attributed with combined Td and Ts, as well as Td+Ts*dip to display slip and dilation in cross plot space according to Ferrill et al. (2020) (Figure 3.2.7). Slip and dilation tendency values were then attributed to the fault map at Desert Queen for visualization of the location of critically stressed fault segments (Figure 3.2.8).

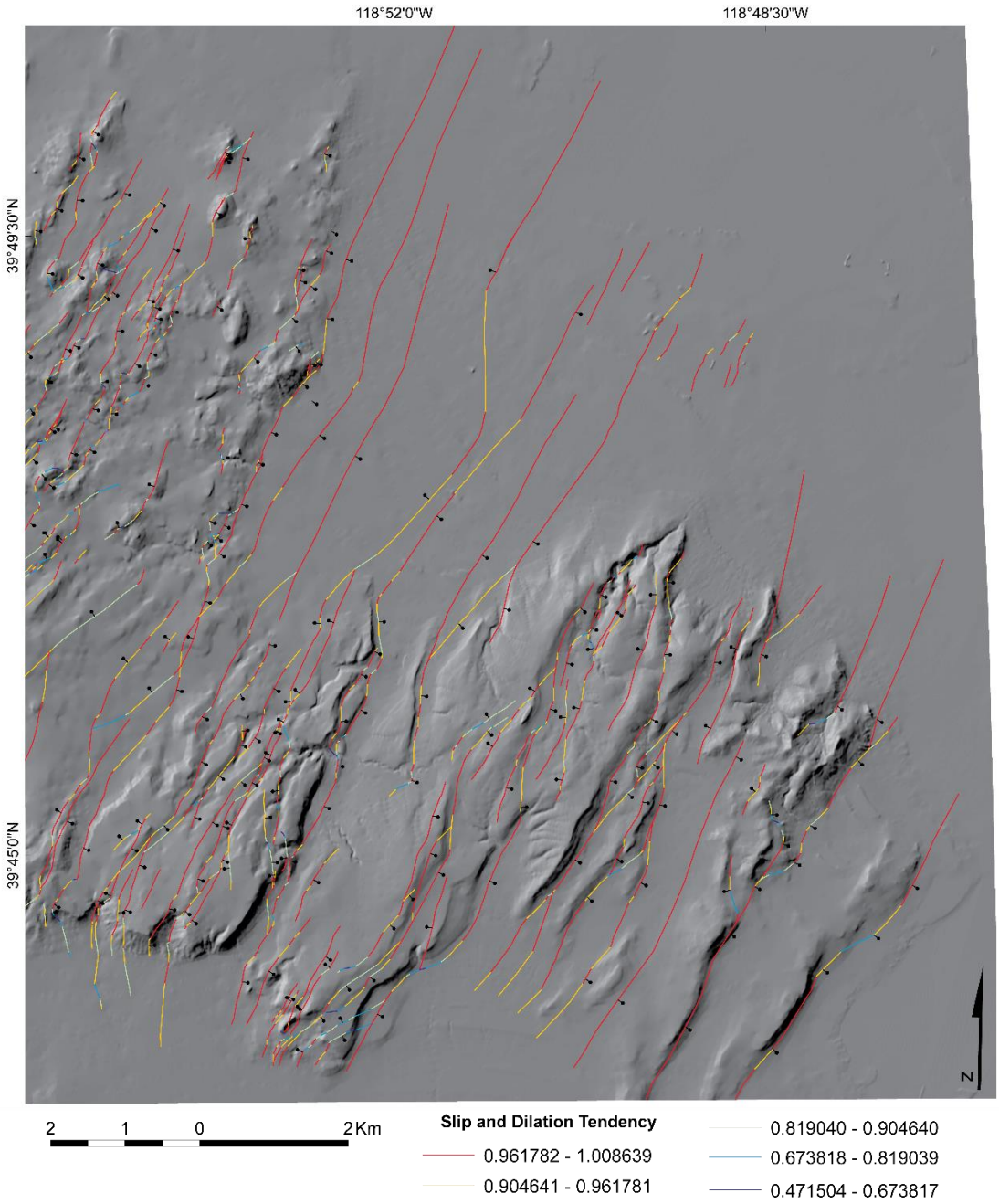

Figure 3.2.8. Slip and dilation tendency fault map. Faults are attributed with combined Td and Ts. Warmer colors represent faults more likely to slip and dilate.

The results of slip and dilation tendency analyses indicate that most of the fault segments at Desert Queen are likely to slip or dilate based in the present-day stress field. Faults striking 026° (simply those that are orthogonal to the calculated S_{hmin} azimuth of 116°) have the highest slip and dilation tendency values. Since most faults mapped in the area strike north-northeast (Figure 3.2.9), many faults that are critically stressed.

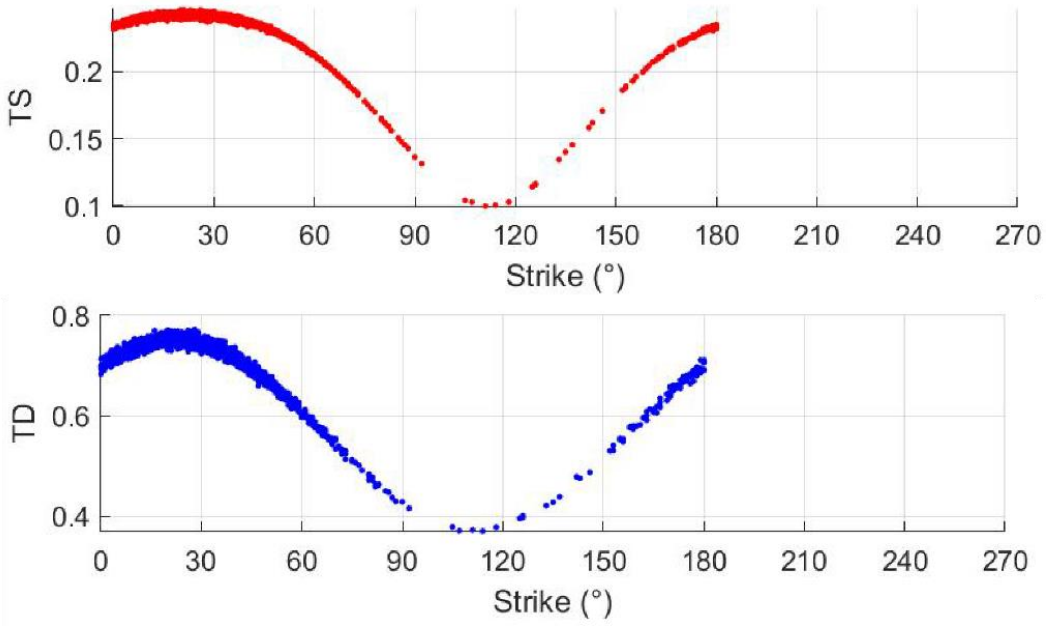

Figure 3.2.9. Slip and dilation tendency vs. strike plots. Most faults strike from 000-060°. Faults striking from ~015-040° have the highest slip and dilation tendency values. Faults striking 116° have the lowest slip and dilation tendency values, as this is the S_{hmin} direction.

3.3 Temperature-Gradient Well Data

All of the drill holes within the Desert Queen study area with temperature data were compiled and attributed with associated temperatures (Appendix C, Table C1). A total of 20 temperature-gradient (TG) wells have been drilled within this area. The majority of these wells were drilled by Phillips Petroleum in the 1970s (Benoit et al.,

1982). Four new TG wells were drilled by Magma Energy in 2010, including the hottest shallow TG well, which has a temperature of 140°C at 140 m depth. TG wells were drilled to depths of 36-302 m, but most have a total depth of less than 100 m. Two stratigraphic holes with temperature data were also compiled within the Desert Queen study area (Strat test 3 and 35-13 on Figure 3.3.1). These were drilled to total depths of 423, 1249, and 2940 m, respectively. These deeper wells contain the hottest bottom hole temperatures, but not the highest temperature gradients.

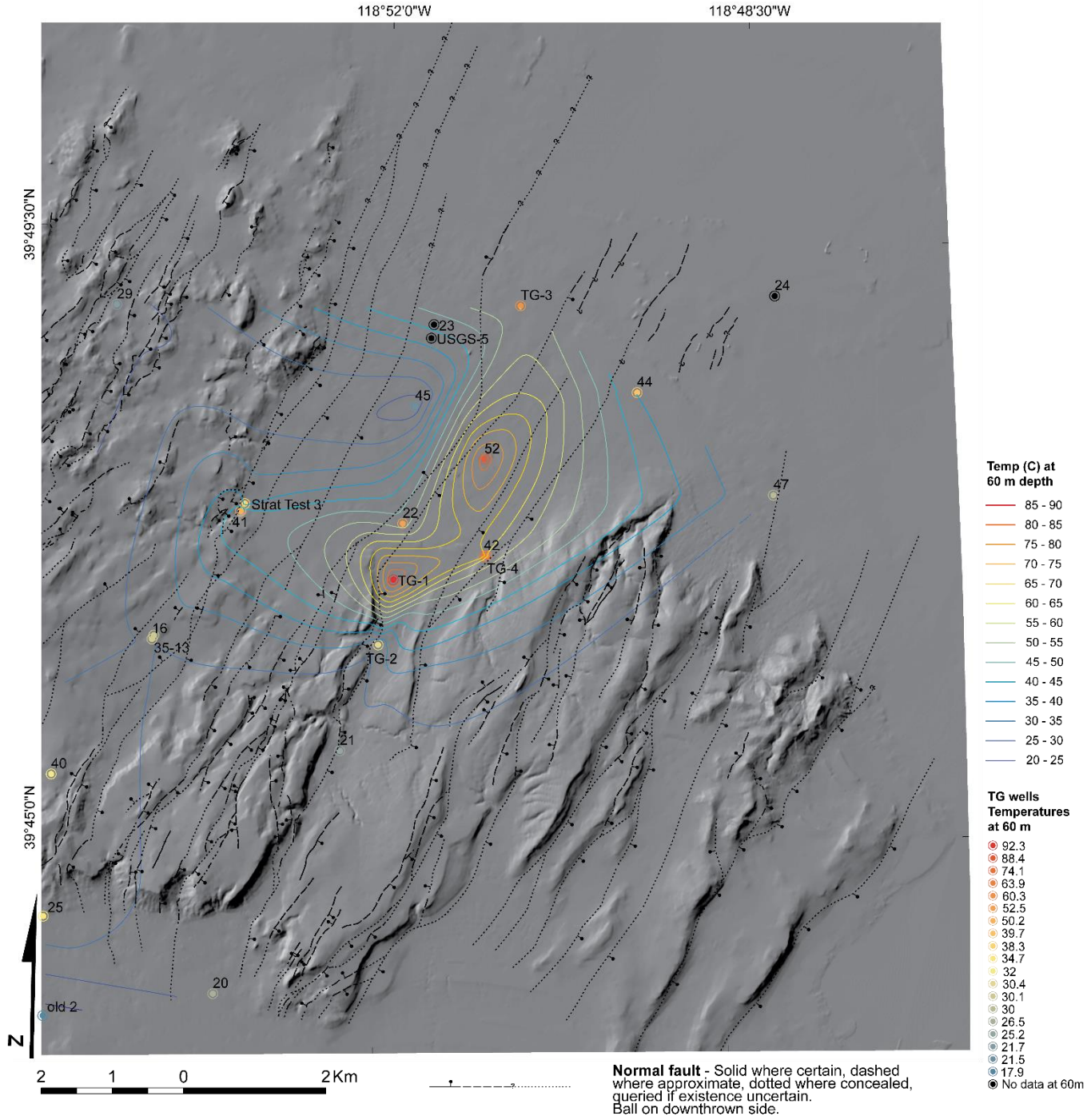

Figure 3.3.1. Locations of wells with temperature data at Desert Queen overlain on DEM hillshade. Well locations are attributed with temperature in °C at 60 m depth and contoured with temperature at 60 m depth. Faults are represented with black lines.

Temperature gradients in wells were used to define temperature anomalies in the Desert Queen study area. Additionally, deeper temperature gradients that are elevated above regional background give preliminary insight into the extent of the deep geothermal reservoir at Desert Queen. The hottest shallow TG wells occur proximal to the Power Line fault (wells TG-1, TG-3, TG-4, 22, 42, and 52 in Figure 3.3.1). One well has moderately high shallow temperature gradients proximal to the Desert Queen fault zone near the southeast termination of the Desert Queen basin (41 in Figure 3.3.1).

3.4 Two-Meter Temperature Survey

A 2 m temperature probe survey was completed by Coolbaugh et al. (2007) across the Desert Peak and Desert Queen areas. This survey was initially used as a test of the 2 m temperature probe method and proved to be a meaningful dataset (Coolbaugh et al., 2007). A total of 117 temperature measurements at 2 m depth were taken within the Desert Queen study area (Figure 3.4.1A) (Appendix C, Table C2). Many variables must be taken into account in considering 2 m temperature data, including solar radiation, climate, and the thermal properties of soils and rocks. Some of these variables were incorporated at Desert Queen by measuring temperatures over a one-year period at certain depths (Coolbaugh et al., 2010). Temperatures at such shallow depths of 2 m can vary by as much as 10-12°C from winter to summer. Thermal diffusivities in different soil and rock types can also allow temperatures at shallow depths to vary on the order of 2-3°C (Coolbaugh et al., 2010).

The 2 m temperature measurements were recalculated against 11 “background” measurements with an average of 22.25°C for the relevant degrees above background

(DAB) of each station (Figure 3.4.1B). DAB value ranges have associated probabilities of a geothermal system as follows: 0-2° = 0, 2-3° = .15, 3-4° = .25, 4-5° = .40, 5-6° = .45, and >6° = .50 (Sladek and Coolbaugh, 2013; Coolbaugh personal communication, 2021). Data points with a DAB of >~3°C are statistically significant thermal anomalies, which may indicate geothermal activity (Sladek and Coolbaugh, 2013).

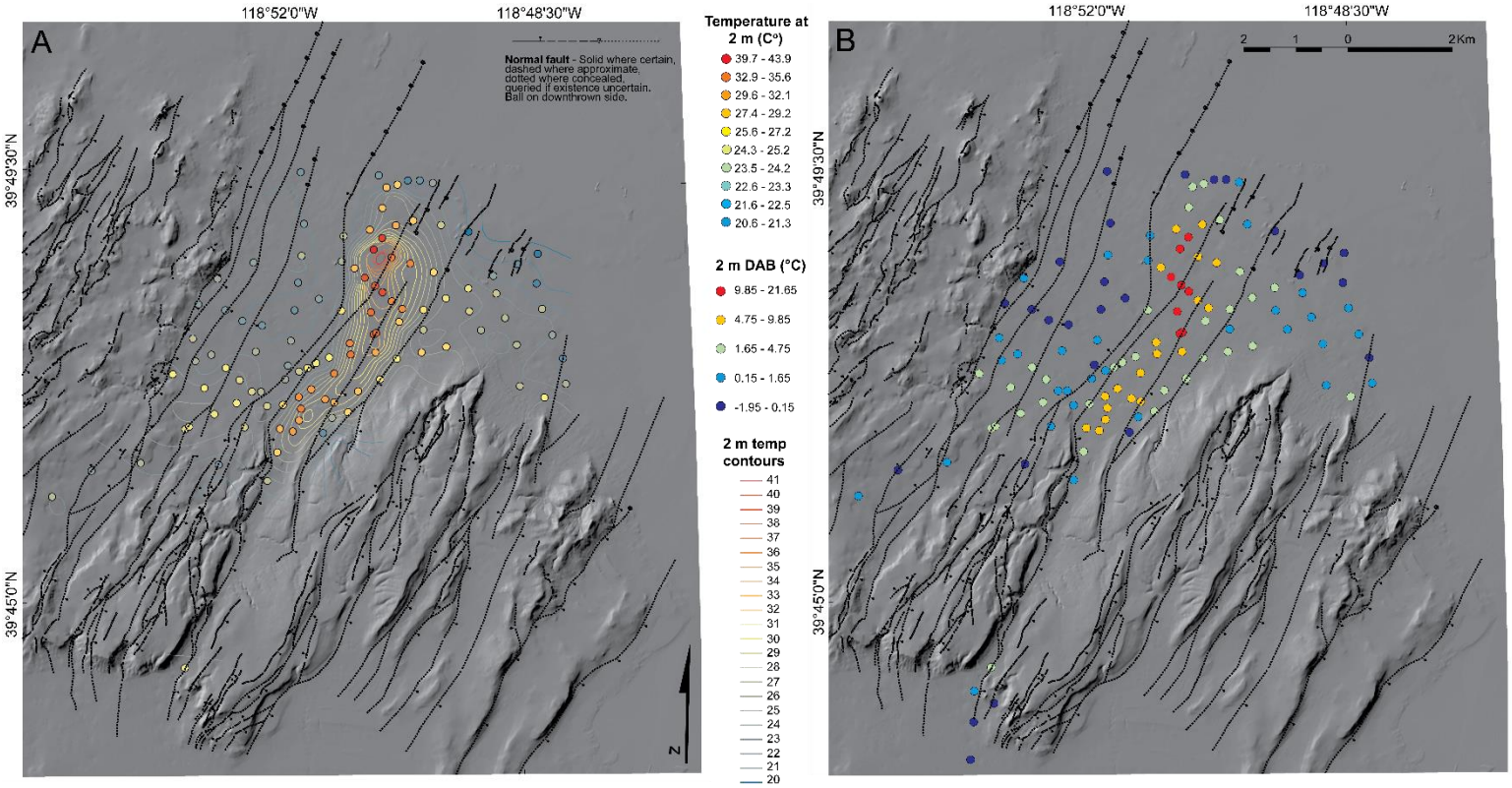

Figure 3.4.1. A) Locations of temperature measurements at 2 m depth attributed with associated temperatures. Temperature contours at 2 m depth are overlain. **B)** Map of 2 m temperatures measurements attributed with calculated degrees above background (DAB) overlain on fault map. The hottest 2 m temperature measurement of 43.9°C is near the center of the Desert Queen basin. A distinct north-northeast trending anomaly is evident proximal to the Power Line fault (easternmost thick black line). There is a more subtle anomaly adjacent to the Desert Queen fault (westernmost thick black line), where it begins to terminate to the south.

The 2 m temperature survey shows two shallow temperature anomalies within the Desert Queen basin. A subtle temperature anomaly exists adjacent to the Desert Queen

fault zone, as it begins to terminate to the south (Figure 3.4.1A). This anomaly is significant at 25°C, which equates to ~3ºC DAB. This anomaly is proximal to the two moderately hot deeper wells drilled adjacent to the Desert Queen fault zone. The second, more distinct 2 m temperature anomaly follows a prominent north-northeast trend adjacent to and along the trace of the Power Line fault (Figure 3.4.1A). This anomaly likely outlines an area of shallow geothermal fluid outflow and ends in the Desert Queen basin with a high temperature of 43.9°C or ~21ºC DAB. It is the hottest 2 m temperature signal measured to date in the Great Basin (M. Coolbaugh, personal communication 2021). There is a general spatial correlation between the distinct 2 m temperature anomaly and the deeper temperature anomaly outlined by the TG wells (Figures 3.3.1 and 3.4.1A).

3.5 Geochemistry and Geothermometry

Some limited geochemical analyses of thermal and non-thermal waters have been conducted at Desert Queen. Three of the TG wells (TG-1, TG-3, and TG-4 in Figure 3.3.1) drilled in 2009 by Magma Energy were analyzed by the Desert Research Institute. These are likely the highest quality analyses completed in the area (Benoit, 2011). Geothermometry of these higher quality analyses was calculated by Benoit (2011) (Table 1). Five additional non-thermal samples were partially analyzed for major components (Garchar and Arehart, 2008). The Desert Queen samples were compared to geochemical samples from the adjacent Desert Peak and Bradys systems (Figure 3.5.1). Evident in these comparisons are the distinct geochemical differences between the three systems in the northern Hot Springs Mountains.

Geothermometry was calculated by Benoit (2010) using an available calculation spreadsheet (Powell and Cumming, 2010) (Table 1). The results of the geothermometry are promising with temperatures ranging from 168- 211°C. Additionally, these results are supported by the agreement between calculated geothermometry and actual measured temperatures observed at Desert Peak and Bradys (Benoit, 2011).

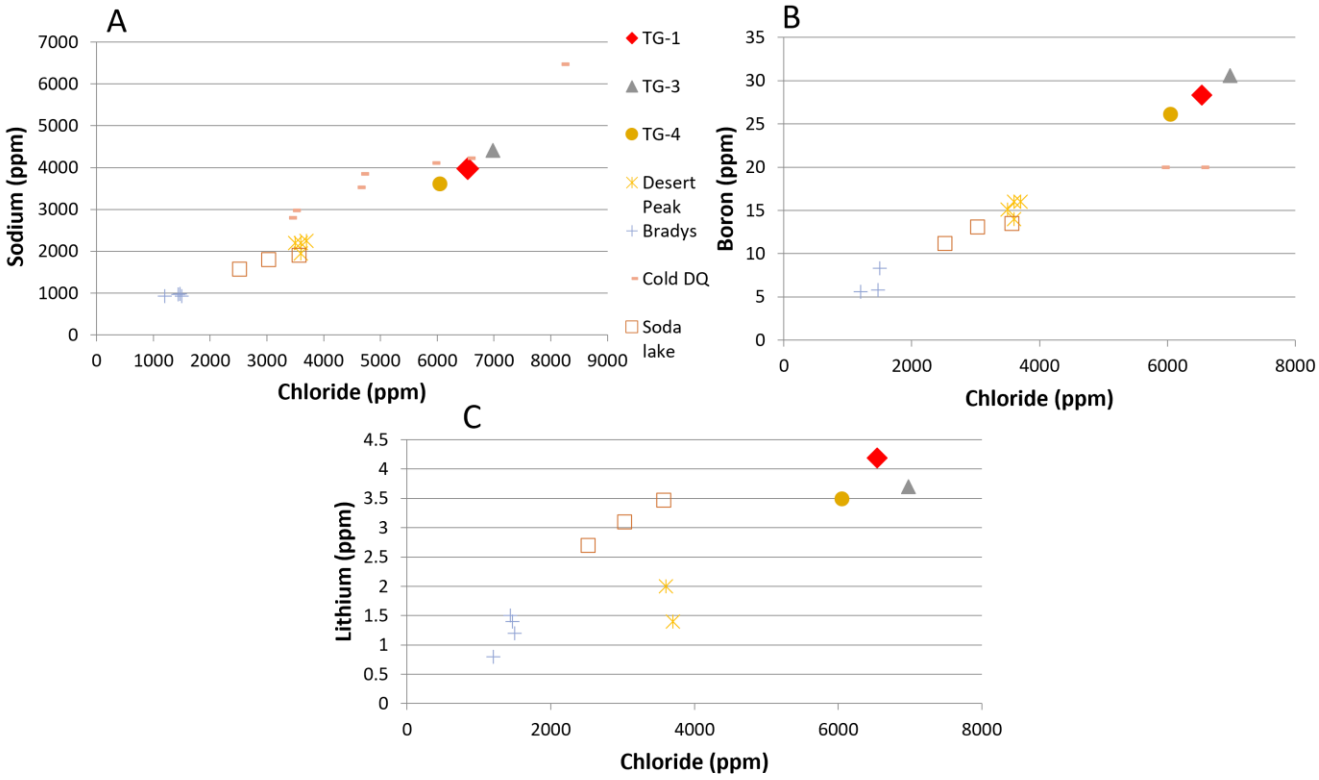

Figure 3.5.1. Plots compiled from Benoit (2011) showing geochemical relationships between the three geothermal systems in the NHSMs as well as Soda Lake (locations in Figure 2.2). A) Sodium vs. Chloride, B) Boron vs. Chloride, C) Lithium vs. Chloride.

Sample	Quartz (°C)	Na-K-Ca (°C)	Na-K-Ca Mg corr (°C)	Fluid entry temp (°C)
Desert Queen TG-1	168	211	209	140

Desert Queen TG-3	98	201	107	
Desert Queen TG-4	127	191	131	
23-1	227	229	228	215 (no flowing log)
Desert Peak 21-2	223	222	222	207
Desert Peak 21-1	213	227	227	207
Bradys Hot Springs	162	193	193	
Brady 8	181	165	165	180 (no flowing log)

Table 1. Geothermometry of selected samples from the NHSMs compiled from Benoit (2010, 2011).

3.6 Geophysical Methods

3.6.1 Gravity Data

Measuring the changes in the gravitational field reveals anomalies that can indicate subsurface faults based on density contrasts, depth, and distribution of offset units (e.g., Romberg, 1958; Blakely and Simpson, 1986). Sharp contrasts in gravity from one area to another reveal subsurface features that may not be evident at the surface. Identifying gravity anomalies and associated gradients in alluvium filled basins is especially useful, because it can reveal the geometry and offset of basin bounding faults, as well as faults concealed under basin fill (Blakely and Simpson, 1986; Athens et al., 2014).

Gravity data in the Desert Queen area have been obtained by multiple sources including 1) Magee Geophysical Services in 2009, 2) UNR/Oppliger in 2003-04, 3) USGS/Ponce from 1997, and 4) Phillips Petroleum in 1979. These data were reprocessed, merged, and leveled by Magee Geophysical services in 2021. A total of 1193 gravity stations were merged and processed into complete Bouguer anomaly and gravity gradient maps. Most of the gravity measurements within the study area were acquired in the 2009 survey by Magee Geophysical services (412 points, Figure 3.6.1A).

The generation of complete Bouguer anomaly (Figure 3.6.1A) and total horizontal gradient gravity (Figure 3.6.1B) maps were of particular importance to refine the location of concealed basin faults and to constrain basin geometries as interpreted in cross sections. Additionally, the complete Bouguer anomaly gravity data from 438 stations within the study area were used for the 3D inversion modeling. The total horizontal gravity gradient map was merged with the regional scale horizontal gravity gradient from Phase I of the Nevada play fairway project (Faulds et al., 2016), allowing for added detail in the regional permeability model of the play fairway analysis completed at Desert Queen (see Section 3.8 below).

The gravity maps define the deepest portion of the Desert Queen basin (bright pink portions in Figure 3.6.1A), as well as the segmentation of the basin by the many fault strands that project into the basin. The most significant gravity low defines the deepest portion of the basin directly adjacent to the exposed Cretaceous basement in the footwall of the Desert Queen fault. Notably, the Power Line fault defines the east side of a narrow horst block that separates the basin into two distinct gravity lows. A broader structural low lies to the northeast of the horst block. The horizontal gravity gradient map displays the very high relative gravity gradient along the Desert Queen fault zone (bright red/pink portion in Figure 3.6.1B), which serves to minimize and thus hinder recognition of gravity gradients in other parts of the study area. This robust gravity gradient is due to the large amount of offset along the Desert Queen fault zone (>2 km), relative to other faults in the area.

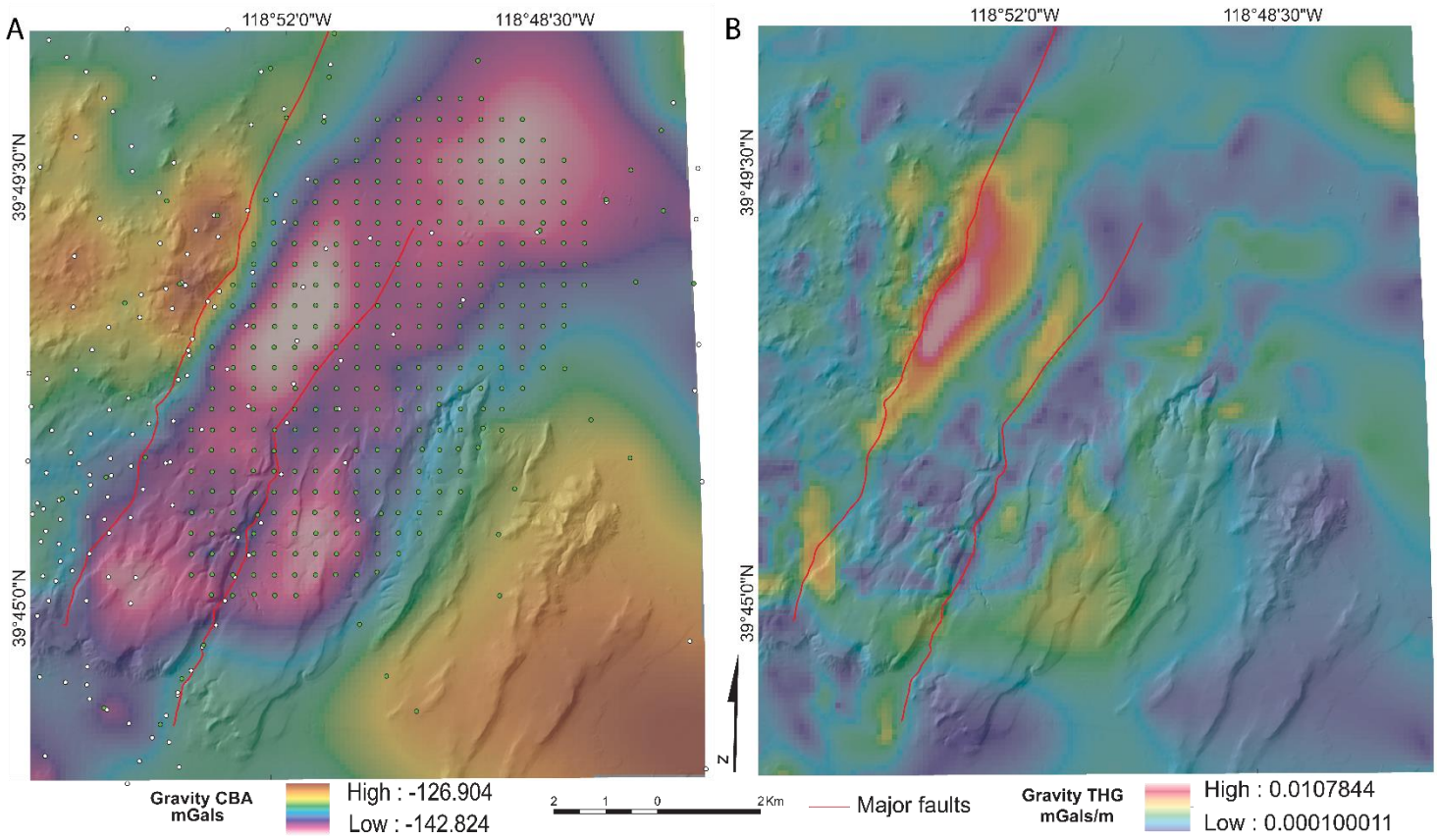

Figure 3.6.1. A) Complete Bouguer anomaly (CBA) map with a terrain correction density of 2.5 g/cm^3 overlain on DEM hillshade. Locations of gravity stations (dots) are superimposed. Green stations are from Magee 2009 survey (412 points). White stations are from four prior surveys (Phillips Petroleum in 1979, Ponce in 1997, and Oppliger in 2003-2004). Gravity values are in milligals, with more negative values indicating relative structural lows and more positive values delineating structural highs. The trace of the main range-front fault strand of the Desert Queen fault is shown (westernmost red line), and the main segment of the Power Line fault is also shown (easternmost red line). CBA map highlights the deepest part of the Desert Queen basin, as well as the segmentation of the Desert Queen basin by a narrow horst block. **B)** Total horizontal gravity gradient map overlain on DEM hillshade. Units are shown in mGals/m, where high values likely represent locations of faults and low values correspond to fault blocks or basins. Main range-front strand of the Desert Queen fault zone (westernmost red line) and main segment of the Power Line fault (easternmost most red line) are shown. Note that the range-front strand of the Desert Queen fault does not correspond to the highest gravity gradient in that area, as the Desert Queen fault zone is made up of 3 to 4 strands that extend across the entire gravity gradient.

3.6.2 Magnetic Data

The magnetic geophysical method measures anomalies in the magnetic field of the Earth over a given survey area. Positive magnetic anomalies can be attributed to rocks that contain abundant magnetic minerals (e.g., magnetite and pyrrhotite) in the subsurface (Telford, 1990). Magnetic anomalies can generally be attributed to intrusive bodies, dikes, volcanic bodies, and faults. Magnetic anomalies must be associated with rocks in the upper crust, as rocks lose their magnetic properties above ~550°C (Telford, 1990). Additionally, low magnetic anomalies can indicate hydrothermal alteration of volcanic rocks due to reduction of magnetic minerals and can ultimately delineate areas of geothermal upwelling, such as at southern Gabbs Valley (Craig, 2018; Craig et al., 2021).

An unmanned aircraft system (UAS) aeromagnetic survey was conducted across most of the Desert Queen basin by Chris Kratt of the Center for Transformative Environmental Monitoring Programs (CTEMPs) lab at the University of Nevada, Reno. Approximately 500 line-km were flown using a GEM GSMP-35U/25U Ultra Light-Weight Potassium Magnetometer deployed beneath a DJI M600 drone. The survey was completed with the magnetometer 50 m above ground level to achieve the highest quality of data possible while maintaining a safe buffer above topography. Magnetic susceptibility measurements were made using a Terraplus KT-10 handheld magnetic susceptibility meter (resolution 1×10^{-6} SI units) for all relevant bedrock units exposed within the survey area (Appendix D, Table D1). The main product of the magnetic data collected at Desert Queen is a total magnetic intensity (TMI) map (Figure 3.6.2). Additionally, Innovate Geothermal Ltd. produced a preliminary 3D magnetic inversion model using the TMI, which was geologically constrained using the three geologic cross

sections (Plate 1) that projected across the magnetic survey area.

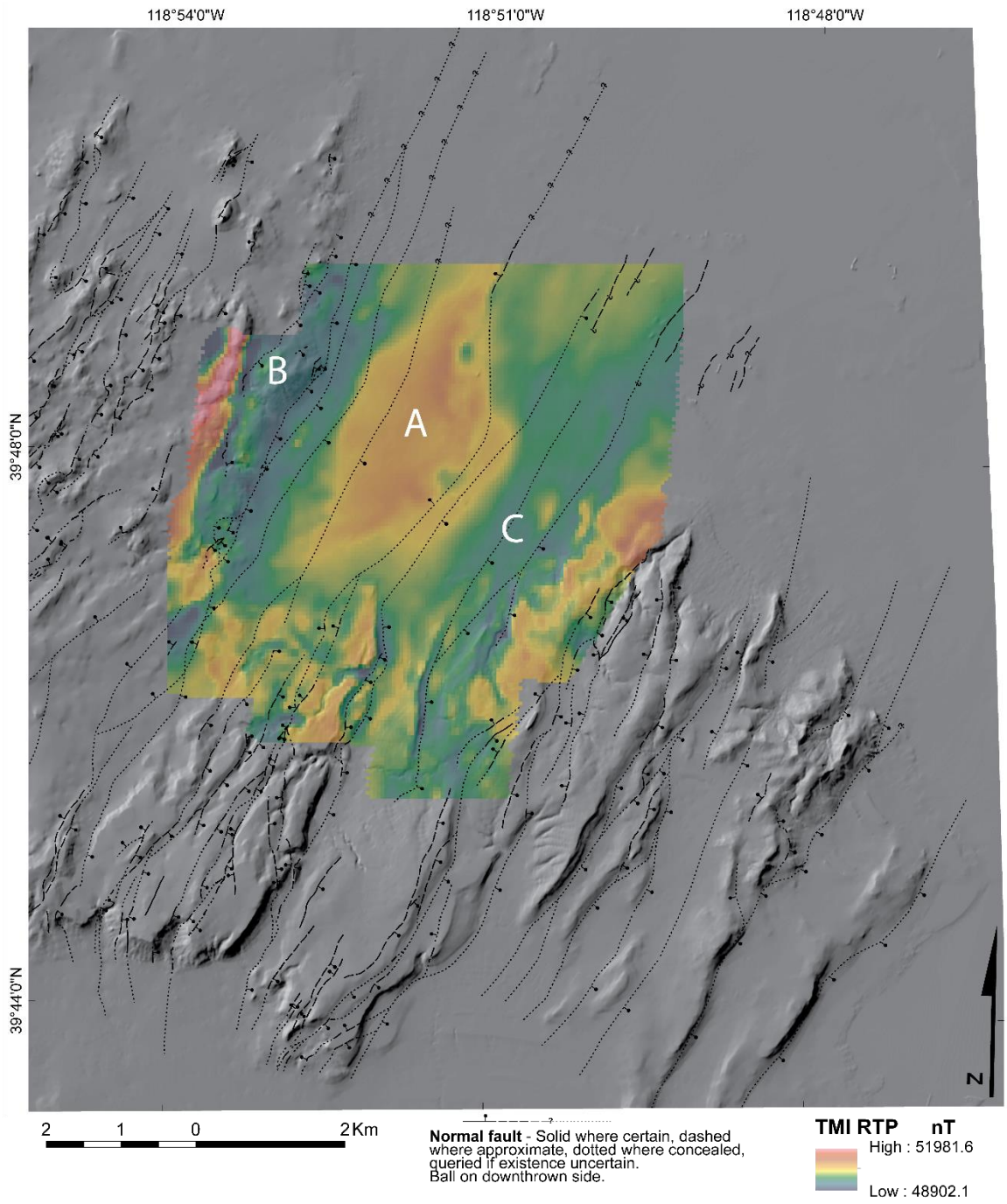

Figure 3.6.2. Total magnetic intensity reduced to pole map overlain on DEM hillshade. colors correspond to high magnetic intensity; cooler colors correspond to lower magnetic intensity. Points of interest discussed in text are annotated with large white letters (A, B, and C).

Used in conjunction with the gravity data, the magnetic data collected at Desert Queen were used to aid in constraining the location of faults beneath basin fill, as well as to better characterize fault geometries in the subsurface. Ultimately, these data allowed for more accurate subsurface interpretations (Plate 1 cross sections). Distinct magnetic lows in areas of interest will be considered in the play fairway analysis.

There are several magnetic anomalies within and proximal to the Desert Queen basin. The most conspicuous anomalies are 1) the distinct high across the presumed deepest portion of the basin, which spatially corresponds with the lowest gravity CBA values (A in Figure 3.6.2), and 2) the area of low magnetic intensity adjacent to the basin and along the range front of the Desert Queen fault (point B in Figure 3.6.2). The area of low magnetic intensity within the footwall of the Desert Queen fault corresponds with the highly altered Eocene-Oligocene sedimentary rocks, as well as the altered andesite unit that overlies the altered sedimentary unit. The large high magnetic anomaly is perplexing, as it occurs over the area of the deepest alluvial basin fill. However, the results of the 3D magnetic inversion model are consistent with the geologic interpretations while still satisfying the total magnetic intensity observed at the surface, but further work is needed to fully understand this anomaly. A relatively narrow, elongated low magnetic anomaly occurs to the east of the Power Line fault and continues along strike into the Desert Queen basin (point C in Figure 3.6.2). Spatially, it roughly corresponds to the 2 m temperature anomaly that follows a similar trend along the east side of the Power Line fault.

3.6.3 3D Gravity and Magnetic Inversion Modeling

Geologically constrained 3D gravity inversion modeling was utilized to assist in the subsurface characterization of the Desert Queen geothermal area. The aim of the 3D gravity modeling was to create a 3D model of rock density that honors the 3D geometry of the major rock units, agrees with measured rock density data, and is consistent with surface gravity measurements. The 3D geologic constraints included: 1) a 3D geologic model, built from 2D geologic cross-sections, that fills a volume 10 km (N-S) x 10 km (E-W) x ~3 km in vertical thickness, and 2) rock density measurements obtained from hand samples in the Desert Queen area. Gravity data consisted of 438 gravity stations with a mean station spacing of ~400 m and an estimated measurement error of 0.05 mGal. The model volume consisted of ~1.5 million cube-shaped cells that varied from 50 m in size (upper half of model volume) to 200 m in size (bottom of model volume). Gravity inversion calculations were performed using open-source SimPEG software (https://simpeg.xyz/).

Multiple rounds of geologically constrained 3D gravity inversion modeling were performed. In each round, the stratigraphic contacts in the 3D geologic model were fixed and the inversion modeling solved for density in each of the model cells. After each inversion round, the density model results were studied, and geologically appropriate adjustments were made to the 3D geologic framework in an effort to improve the agreement between the 3D geology, rock density, and gravity. As part of the 3D gravity inversion model runs, the Lp Norm regularization and reference model scaling factor (see Appendix E) were varied to explore possible alternate solutions in the density model space. For each inversion model output, the misfit was calculated at each gravity station

(misfit is a measure of the difference between the observed gravity data and the calculated gravity response of the 3D density model volume). Overall, for the 3D gravity inversion runs, the RMS misfit ranged from 0.04 – 0.09 mGal, which compares to an estimated measurement error of 0.05 mGal for the gravity data. A detailed explanation prepared by Innovate Geothermal Ltd. can be found in Appendix E.

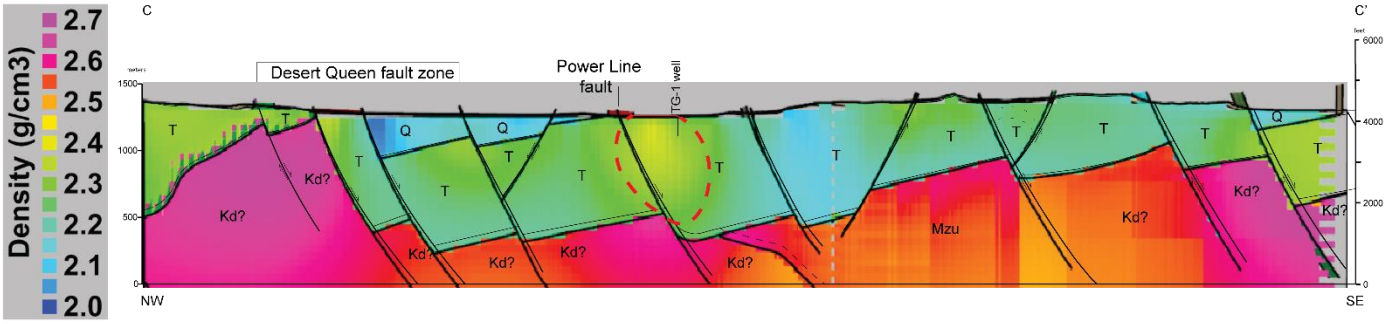

Figure 3.6.3. Generalized geologic cross section D-D' overlain on a profile extracted from the 3D gravity inversion model. Warmer colors equate to higher density regions, and cooler colors to lower density areas. Labeled geologic units are as follows: Q = Quaternary deposits, T = Tertiary volcanic and sedimentary rocks, Kd = Cretaceous diorite, Mzu = undivided Mesozoic basement. Locations of Desert Queen fault zone, Power Line fault, and projected TG-1 well are shown. Red dashed ellipse outlines the conspicuous high-density anomaly that follows the Power Line fault.

Results from the 3D gravity inversion model consist of a geologically constrained 3D density model. Density profiles along the working geologic cross sections (A-D on Figure 2.2.2; Plate 1) were prepared, as well as density anomaly plan view maps at depths of 100, 200, and 300 m. The latest version of the 3D gravity inversion model is in good agreement with both geologic constraints and surface gravity data (Figure 3.6.3). The density profiles generated from the 3D inversion model allowed for interpretation of the diorite pluton beneath the Desert Queen basin, where no data existed prior. Additionally, the density profiles revealed an interesting high-density anomaly centered in the upper ~500 m of the Miocene volcanic and sedimentary section in the footwall of the Power

Line fault. This relatively high-density anomaly is somewhat continuous along the north-northeast strike of the Power Line fault (Figure 3.6.4). Additional density anomalies outlined in this version of the inversion model suggest that some geologic reinterpretations are necessary. Namely, the broad, minor, low-density anomaly throughout the Miocene section beneath the deepest portion of the Desert Queen basin in the hanging wall of the Desert Queen fault zone can be attributed to the presence of large (300-400 m) packages of lower density rocks compared to that shown in the generalized geologic cross section presented in Figure 2.2.3. Low density anomalies in the basement below associated low-density anomalies in the Miocene section may result from lower density material in the Miocene section and/or thicker sections of altererd Eocene-Oligocene sediments than currently shown in the cross sections.

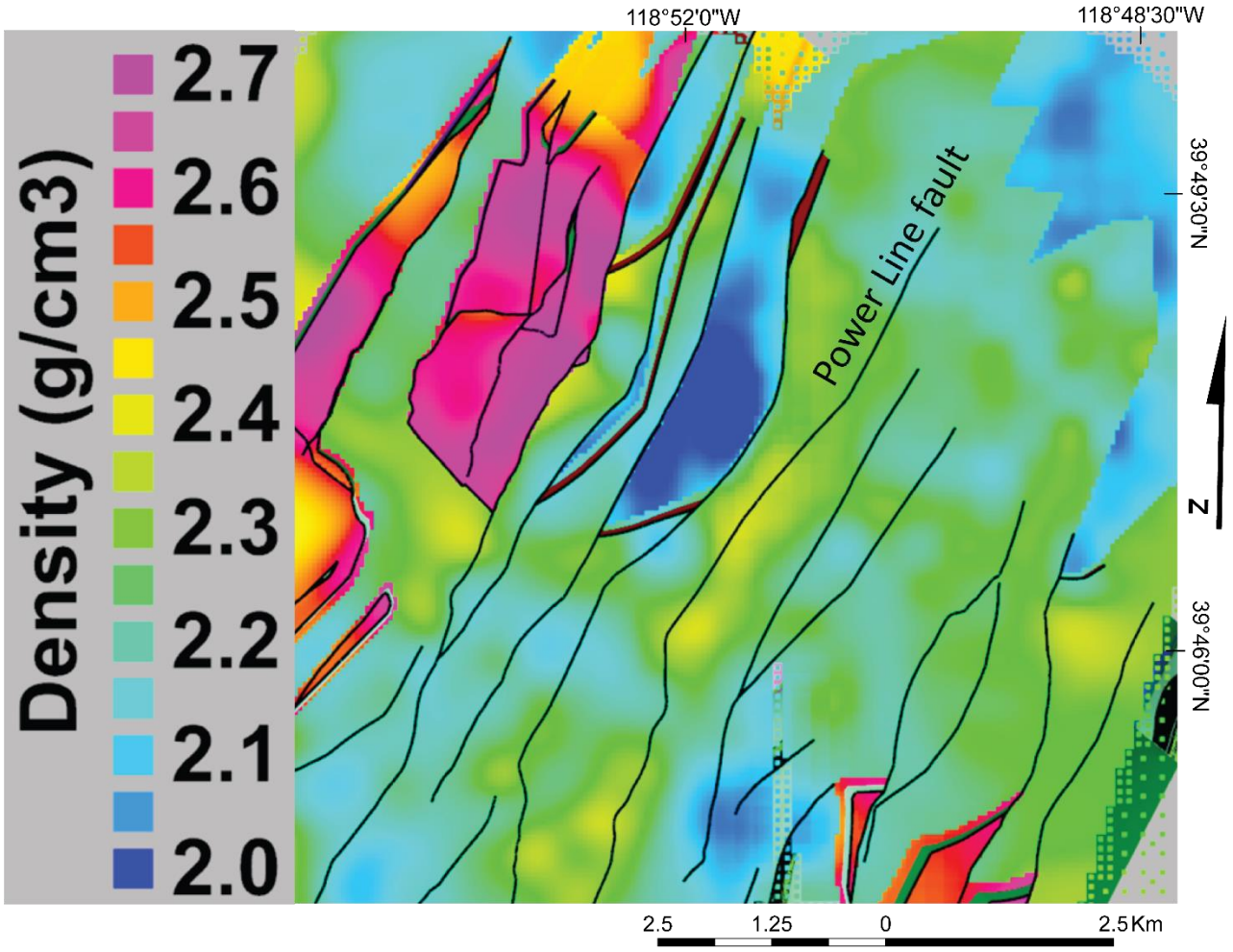

Figure 3.6.4. Plan view density anomaly map at 300 m depth in the 3D gravity inversion model. Note that the relatively high-density anomaly discussed in the text extends along strike of the Power Line fault.

3.6.4 Magnetotelluric Data

The magnetotelluric (MT) geophysical method uses the natural sources of electromagnetic fields (e.g., lightning for fields above 1 Hz and solar activity below 1 Hz) to "image" the electrical conductivity in the subsurface (Vozoff, 1991). Masses of low resistivity (i.e., conductive) delineated with MT can indicate the presence of clay bodies, fluids, and thermal anomalies. This technique is useful in constraining possible

geothermal reservoirs at depth.

A 3D MT inversion was conducted by Quantec Geosciences for Magma Energy in 2010. Resistivity plan maps for depths from 300 m to 15,000 m in varying increments were the only available products from this inversion available in this study (Figure 3.6.5). These maps were used in conjunction with the play fairway analysis favorability model to further delineate potential exploration targets at Desert Queen. There are numerous conductive and resistive anomalies at varying depths within the Desert Queen basin, and as such it is important to consider these resistivity maps carefully alongside the available gravity, magnetic, and temperature gradient grids.

There are a number of distinct resistivity anomalies in the MT depth slices from 300-1200 m depth. A widespread low resistivity anomaly exists over much of the Desert Queen basin down to a depth of ~600 m, where it starts to give way to a moderately conductive body (Figure 3.6.5A, B). At ~900 m depth an elongated north-northeast trending low resistivity (more conductive) anomaly exists directly adjacent to a similarly shaped high resistivity anomaly (Figure 3.6.5C). These two anomalies spatially correlate with the step over from the Desert Queen fault to the Power Line fault. The elliptical shaped less resistive anomaly continues well below the 1200 m depth to at least 2400 m, where it projects slightly to the southwest (Figure 3.6.5D). The broad low resistive anomaly at 300 m depth roughly spatially correlates with the shallow temperature anomaly delineated by temperature-gradient wells and the 2 m temperature survey.

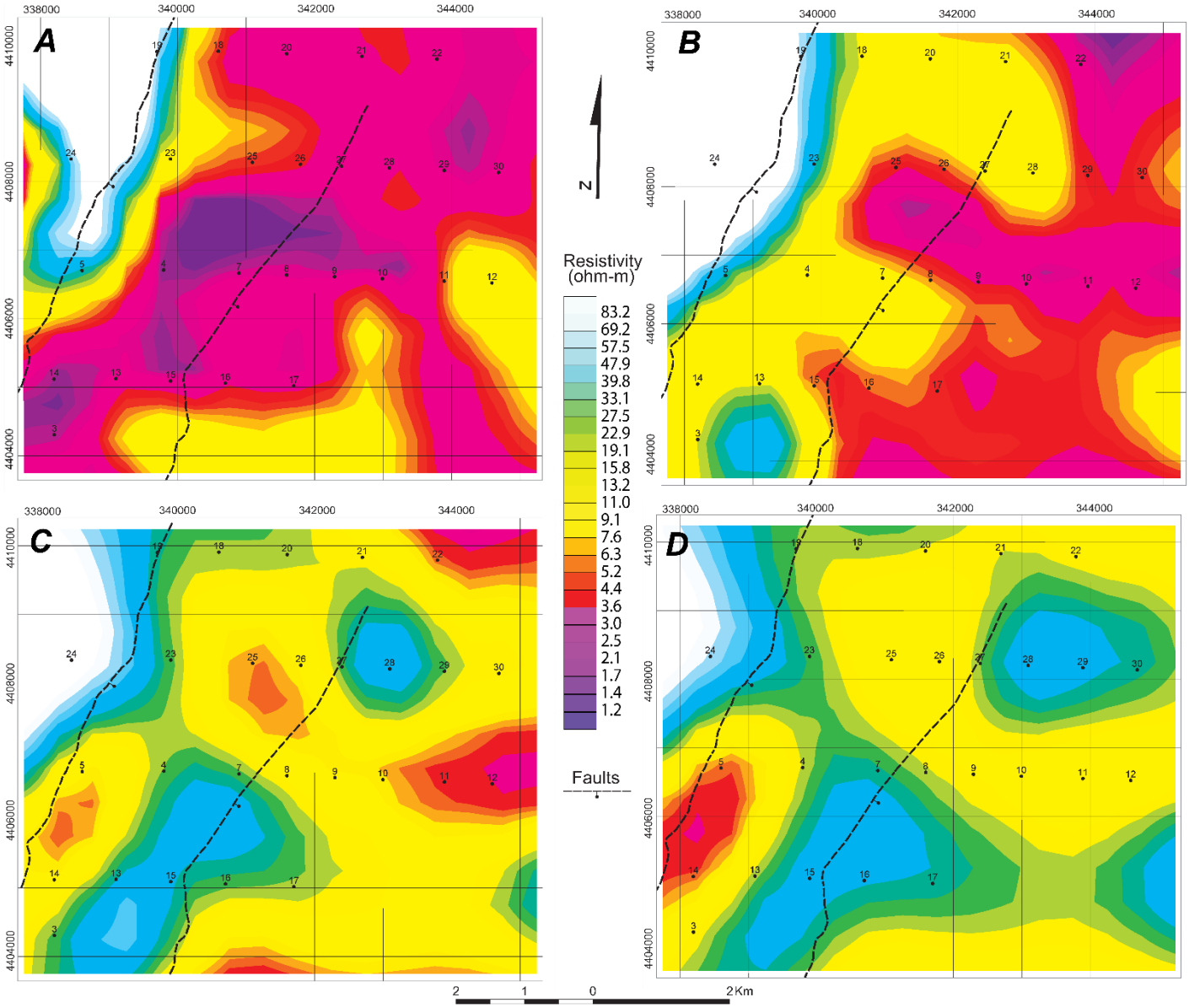

Figure 3.6.5. Magnetotelluric inversion slices over the Desert Queen basin: **A)** 300 m depth, **B)** 600 m depth, **C)** 900 m depth, **D)** 1200 m depth. Grids are in 1 km increments and labeled with UTM coordinates (NAD 83 zone 11N). Resistivity values are in ohm-m with purples and reds representing less resistive bodies (i.e., more conductive), and blues and greens denoting more resistive bodies. The surface traces of the main range-front fault strand of the Desert Queen fault is shown (westernmost dashed line), and the main segment of the Power Line fault is also shown (easternmost dashed line).

3.7 Identification of Favorable Structural Settings

Three favorable structural settings were recognized at Desert Queen based primarily on detailed bedrock and Quaternary geologic mapping and to a lesser extent on gravity data. This included two settings that were not previously identified. In addition, two hybrid settings were denoted in the overlap zones between two of the favorable settings (Figure 3.7.1). The identified favorable settings include: 1) the southern horse-tailing termination of the Desert Queen fault zone (Annotated "A" in Figure 3.7.1), 2) the left step over (i.e., relay-ramp) of the Desert Queen fault zone to the smaller displacement Power Line fault (Annotated "B" in Figure 3.7.1), and 3) the north-northeast termination of the Power Line fault in the Desert Queen basin (Annotated "C" in Figure 3.7.1). The first hybrid structural setting is the overlap zone between the southern termination of the Desert Queen fault and the left step over of the Desert Queen fault to the Power Line fault (Annotated "D" in Figure 3.7.1). The second hybrid structural setting is the overlap zone between the left step over of the Desert Queen fault to the Power Line fault and the termination of the Power Line fault in the Desert Queen basin to the north (Annotated "E" in Figure 3.7.1).

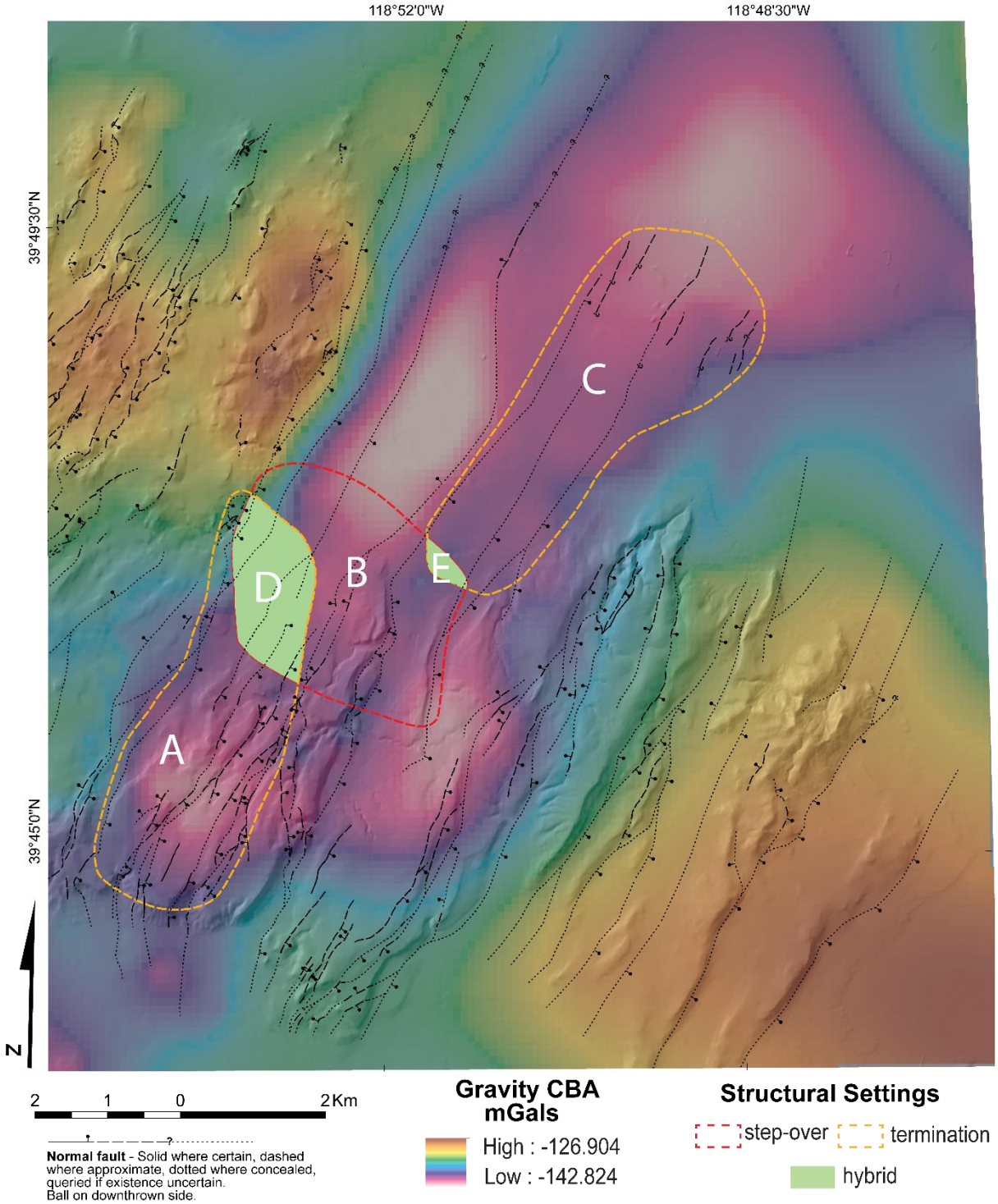

Figure 3.7.1. Complete fault map, as well as the location, type, and extent of favorable structural settings superimposed on CBA graviy map. Details of each structural setting discussed in text are annotated with large white letters (A, B, C, D, and E).

3.8 Play Fairway Analysis

The Nevada play fairway methodology is a technique developed to mitigate exploration risk in geothermal fields by integrating multiple datasets and applying statistical modeling. Phase I of the Nevada play fairway project employed nine parameters: favorable structural setting, location of Quaternary faults, slip and dilation tendency of Quaternary faults, regional strain rates, modeled sub-surface temperature at 3 km depth, age and slip rate on Quaternary faults, gravity data, earthquake density, and geochemical parameters of available springs and wells (Faulds et al., 2016). These parameters were grouped into subsets that defined local-, intermediate-, and regional-scale permeability models. The combined permeability models were then merged with the modeled subsurface temperatures at 3 km depth to produce the geothermal play fairway model. Spatial statistical methods were employed along with a fuzzy logic scheme (e.g., Coolbaugh et al., 2007b) to determine optimal weights for each parameter. The statistical methods were based on 34 benchmarks of relatively high temperature (>130°C) geothermal systems to ultimately generate the best predictive regional model of geothermal potential (Faulds et al., 2016; Figures 1.3 and 3.8.1).

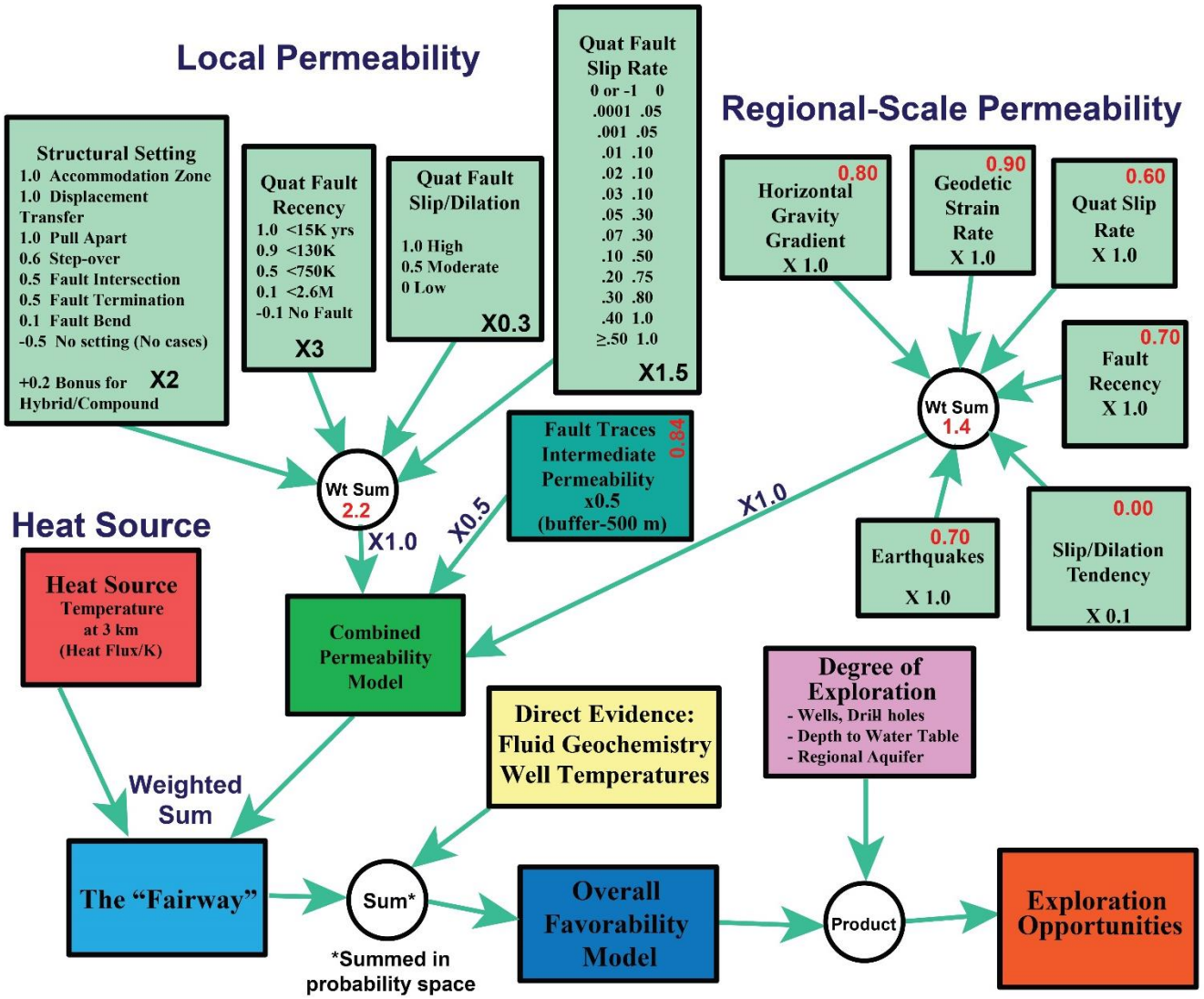

Figure 3.8.1. Phase I play fairway modeling work flow (Faulds et al., 2016). Workflow chart displays how permeabillity inputs are grouped based on scale, as well as how heat source and direct evidence are input into the modeling. Relative, statistically derived weights are shown in red, whereas expert driven weights are shown in black.

Phase II of the Nevada play fairway project focused on five of the highly favorable areas outlined by the results of Phase I. Different techniques were employed to refine the analysis in the detailed study areas, including detailed geologic mapping, Quaternary fault analysis, shallow temperature surveys, detailed gravity surveys, Lidar in

three areas, geochemical analysis of water samples, seismic reflection analysis (where available), finer-scale slip and dilation tendency analysis of Quaternary faults, and 3D modeling (Faulds et al., 2016, 2018). The goal of these more detailed studies was to identify specific areas with high likelihood for permeability and heat, which would guide the selection of individual drill sites at each location. The studies in Phase II revealed that each study site contained multiple favorable structural settings and therefore had multiple potential targets for geothermal production. The play fairway analysis was revised in these detailed study areas to vector into the most promising locations for drilling (Faulds et al., 2018, 2019, 2020; McConville, 2018; Craig, 2018; Craig et al., 2021). The refined analysis utilized the same general methodologies as Phase I (Faulds et al., 2015a) to produce detailed predictive maps. However, the local-scale permeability models were revised to reflect new detailed geologic mapping, geophysical surveys, and additional geochemical data, as well as inclusion of a structural settings quality factor, MT data, 2 m temperature anomalies converted to degrees above background, and the presence of paleo-geothermal features (Faulds et al., 2016, 2018). The refined analysis ultimately led to the generation of play fairway predictive maps, error maps, and direct evidence maps that outlined areas of high favorability in much greater detail than in Phase I (Faulds et al., 2018, 2020).

The fine-scale play fairway analysis conducted at Desert Queen more closely resembles that carried out in Phase II of the Nevada play fairway project (Faulds et al., 2018, 2019; Craig, 2018; Craig et al., 2021). Local-scale permeability was modeled using inputs based on detailed geologic mapping, structural analysis, and slip and dilation tendency of Quaternary faults. Permeability was modeled in much the same way as Phase

I of the Nevada play fairway project (Faulds et al., 2016), with regional-, intermediate-, and detailed-scale permeability parameters weighted in groups. The detailed-scale permeability group included the use of a structural settings quality factor similar to Phase II of the Nevada play fairway project. The most significant change to the play fairway workflow introduced in this study was the modification of the intermediate-scale permeability group to bridge the gap more effectively between regional- and detailed-scale with pertinent new datasets

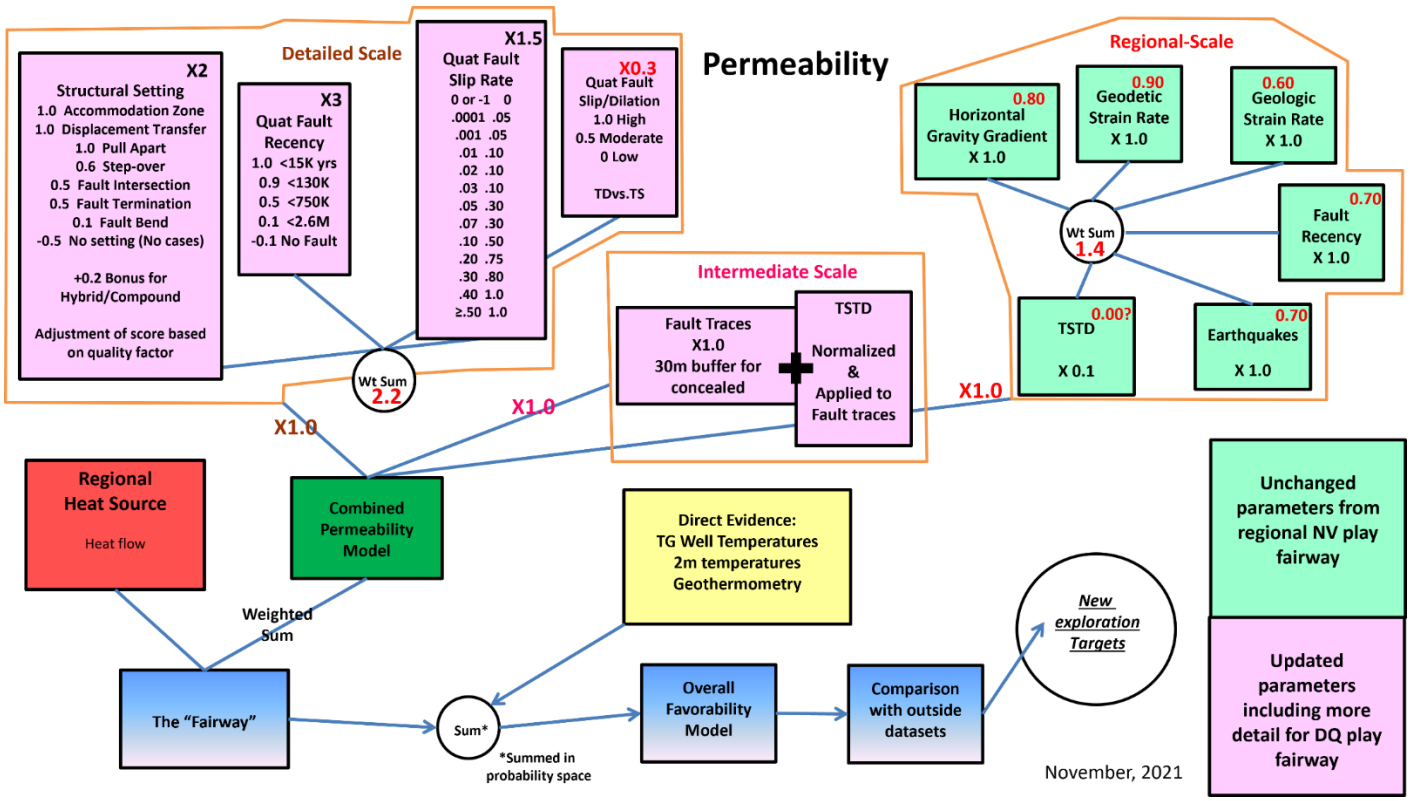

Figure 3.8.2. Desert Queen play fairway analysis workflow chart. Regional-, intermediate-, and detailed-scale permeability parameters are grouped accordingly in the upper part of the chart. Included with each parameter are relative, statistically derived weights (red) and expert driven weights (black). Unchanged parameters from Phase I of the Nevada play fairway project (Faulds et al., 2016) are shown in green. Paramenters updated to include further detail for the Desert Queen area are denoted in purple. Regional heat source data are updated from the Nevada machine learning project (Smith, 2021). Direct evidence parameters are specifc to the Desert Queen area.

The specifics of the Desert Queen play fairway analysis are as follows. The analysis was carried out using the Phase I Nevada play fairway statistical methods for predicting permeability and geothermal potential (Faulds et al., 2015a) (Figure 3.8.1) as a baseline for the finer scale approach. Permeability inputs are weighted in groups based on scale (regional-, intermediate-, and local-scale) and combined into an overall permeability model. The combination of the combined permeability model and heat flow result in a "fairway" map. The "fairway" was then summed in probability space with direct evidence inputs (e.g., temperature data from wells) to produce an overall favorability model. This approach was refined to a finer scale in a similar fashion to that performed in Phases II and III of the Nevada play fairway project at southern Gabbs Valley and northern Granite Springs Valley (Faulds et al., 2016, 2019; Craig et al., 2017, 2021; McConville, 2018; Craig, 2018).

The general workflow of the Phase I Nevada play fairway modeling was preserved, but parameters were updated to incorporate new detailed datasets at Desert Queen (Figure 3.8.2). Input parameters used in regional-scale permeability were retained from the Phase I Nevada play fairway analysis (Faulds et al., 2016) or replaced with updated datasets from the Nevada machine learning project (Brown et al., 2020; Smith et al., 2021; Smith, 2021), where available. For example, the horizontal gravity gradient was updated to include the detailed horizontal gravity gradient map produced for Desert Queen (Figure 3.6.1B). Intermediate-scale permeability was expanded to include the detailed slip and dilation tendency analysis (TSTD) for Desert Queen. The TSTD was normalized and applied to the fault trace buffers. The fault trace buffers were updated such that 1) concealed faults were given a buffer of ±30 m, 2) approximately located

faults were given a buffer of ±20 m, and 3) well-located faults were given a buffer of ±10 m. The updates to the intermediate-scale permeability parameter allowed for the fault traces to better represent the finer scale of the analysis. All of the inputs in the local- or detailed-scale permeability parameter were updated to reflect new detailed data obtained at the finer scale at Desert Queen.

The direct evidence parameters that were combined with the fairway to produce a favorability model of Desert Queen included 1) temperature gradient well data, 2) 2 m temperature data, and 3) geothermometry. Temperature gradient wells were given a buffer of 250 m to allow for their envelope of influence to be significant enough to produce a usable result. The maximum temperatures in each well were compared to predicted temperatures at the same depths based on regional temperature gradients; these were subsequently converted to probability of the occurrence of a geothermal system. The 2 m temperature data were recalculated to degrees above background, based on an assumed background of 22.25°C, and then transformed to probability of occurrence of a geothermal system (e.g., Sladek and Coolbaugh, 2013). Three temperature gradient wells and two artesian wells at Desert Queen had available geothermometry. The best-estimated geothermometer temperature was used based on criteria from Coolbaugh (personal communication, 2021).

4. Discussion

The purpose of this study was to synthesize and refine existing datasets, as well as integrate newly acquired datasets at Desert Queen, into a detailed fine-scale play fairway analysis. Desert Queen hosts a blind geothermal system that was recognized by many

past studies (Benoit et al., 1982; Coolbaugh et al., 2007; Faulds et al., 2010). Existing knowledge and extensive prior exploration at Desert Queen allowed for application of the geothermal play fairway analysis that focused on optimizing continued exploration efforts rather than discovering a previously unknown system. The following sections present an updated structural and geothermal model that allowed for the refining and delineation of new favorable structural settings and identification of areas with the greatest potential for future development. Correlation of the many datasets synthesized in this study are discussed as related to the generation of the play fairway and favorability models. Continued exploration recommendations and potential new targets are also addressed based on interpretations of comparisons of the play fairway maps to additional maps portraying geophysical data and direct evidence (e.g., temperature data from 2 m probes and TG wells) that were not incorporated into the play fairway model.

4.1 Refined Structural Model

Integrating prior geological datasets with newly acquired and reinterpreted data allowed for a thorough characterization of the structural framework of the Desert Queen area. Detailed geologic mapping paired with existing and new geophysical datasets have constrained the locations and geometries of major and minor faults within and proximal to the Desert Queen basin. This permitted identification of numerous favorable structural settings capable of controlling geothermal upwellings in the area.

The detailed geologic map and cross sections finalized in this study elucidate the structural framework and complexity of the Desert Queen area, particularly the Desert Queen basin (Plate 1). The Desert Queen area is characterized by a prominent north-

northeast-trending structural grain consisting of many west-tilted fault blocks cut by multiple north-northeast striking, east dipping normal faults (Plate 1). The Desert Queen fault zone is the most prominent fault zone and consists of four major strands. It has accommodated more than 2 km of down to the east normal displacement and accommodated exposure of the only pre-Tertiary basement rocks in the northern Hot Springs Mountains. The Desert Queen fault zone terminates to the south-southwest in conjunction with the termination of the Desert Queen basin and splays into many smaller faults that cut Parran Mesa in the southern part of the study area (Location A in Figure 3.2.7). Merged gravity data suggest that the Desert Queen fault continues north-northeast beyond the study area as the Desert Queen basin widens to the northeast. The other major fault in the Desert Queen area is the Power Line fault, which bisects Parran Mesa (Figure 2.2.2). The Power Line fault has accommodated much less offset (< 200 m) than the Desert Queen fault in the upper part of the Miocene volcanic and sedimentary section but has likely accommodated much more offset at depth. The Power Line fault projects north-northeast into the Desert Queen basin, where it likely terminates and horsetails into many smaller splays, as evidenced by gravity data. The presumed termination of the Power Line fault occurs in the vicinity of several lineaments that cut the lacustrine sediments in the basin and are interpreted as evidence of Holocene faulting (Figure 2.2.2, Plate 1). These lineaments are essentially the only evidence of Holocene faulting in the Desert Queen study area and spatially correlate with several tufa mounds. Additionally, the interpretation of gravity data within the Desert Queen basin defined a major antithetic north-northeast- to north-striking, west-dipping normal fault, the Gravity fault (Figures 2.2.2 and 4.1.1). This fault adds structural complexity within the basin and bisects the

prominent left step-over/relay ramp between the major strands of the Desert Queen fault zone and the Power Line fault.

Although on first order the Desert Queen area, and in particular the Desert Queen basin, appear to be structurally simple, the area is more complicated than a simple half graben bounded by a major normal fault. The Gravity fault adds another level of complexity to the basin, such that the basin is better characterized as two sub basins separated by a narrow, gently tilted horst block (Figures 2.2.3 and 4.1.1; Plate 1). The horst block is bounded on the west by the Gravity fault and on the east by the Power Line fault. It effectively terminates southward into the Parran Mesa, as the Gravity fault loses displacement (Location A in Figure 4.1.1). Based on gravity data, the narrow horst block eventually closes off the deeper part of the Desert Queen basin, as the Gravity fault either loses displacement or is cut by the Desert Queen fault zone to the north. The shallower, broader part of the Desert Queen basin (Location B in Figure 4.1.1) extends at least another 4 km to the north-northeast. Thus, the Desert Queen basin appears to be a complex composite basin consisting of several individual half grabens that have coalesced into one broad basin as the original discrete half grabens largely filled with sediment.

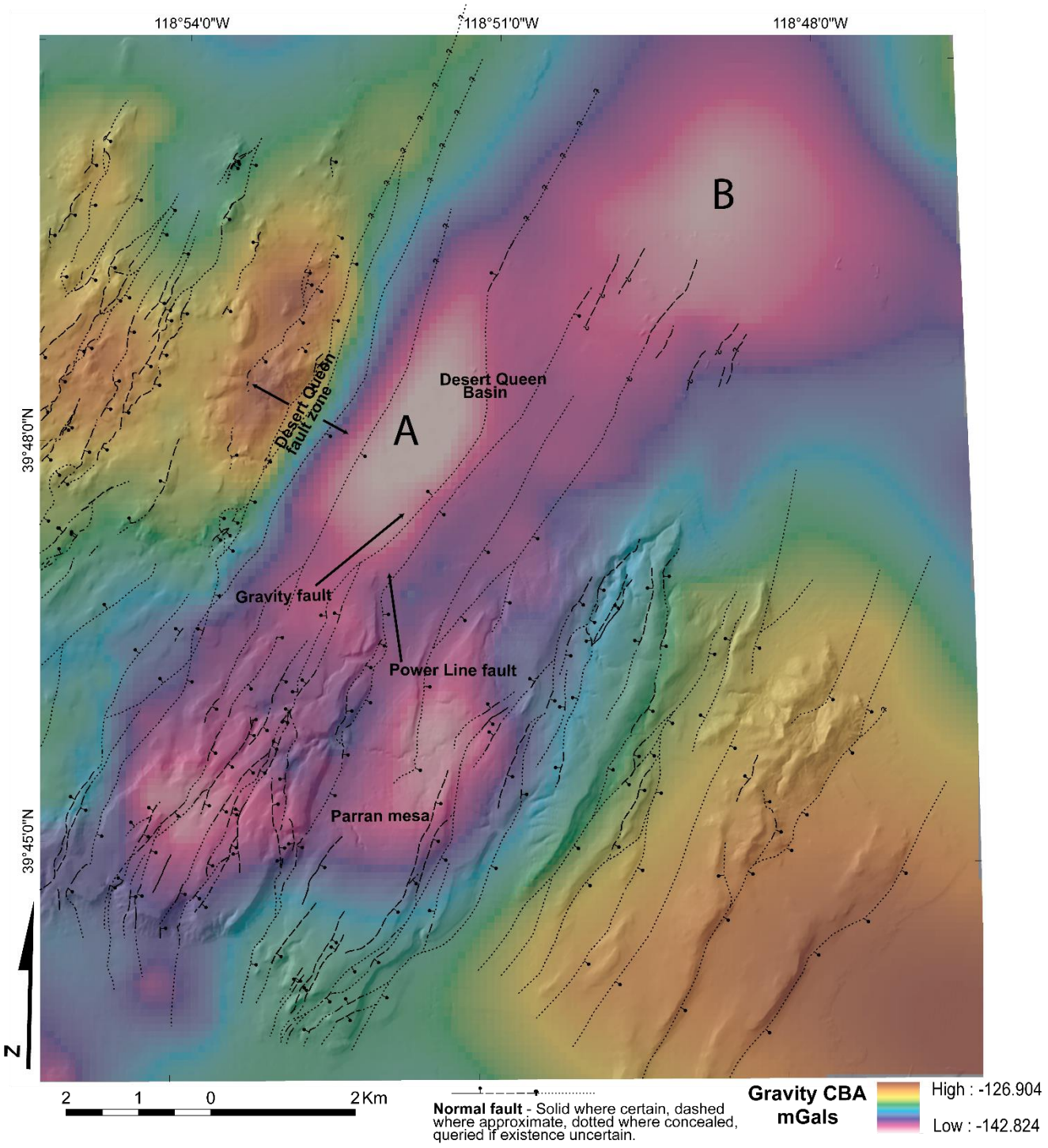

Figure 4.1.1. Detailed fault map overlain on complete Bouguer anomaly gravity map. Gravity lows are interpreted as structural lows. Locations discussed in text are annotated as A and B, respectively.

In addition to revealing details about the basin architecture, the CBA data also highlight some other interesting complexities of the Desert Queen structural and stratigraphic framework. There are two fairly distinct low gravity anomalies associated with Parran Mesa south of the Desert Queen basin (Figure 4.1.1). These can likely be attributed to a thicker package of lower density sedimentary rocks within the Miocene stratigraphic section. The middle part of the Miocene section (~13-10 Ma) temporally correlates with major extension in the region (Faulds and Garside, 2003; Faulds et al., 2010, 2012). Synextensional deposition of the Miocene rocks produced significant lateral variations in thicknesses of the sedimentary and possibly volcanic packages due to growth-fault relations in the developing basins. These low gravity anomalies likely mark an earlier southward continuation of the Desert Queen basin, which has since been infilled with Miocene sedimentary and volcanic rocks. Additionally, there is a significant gravity high that defines the southeastern portion of Parran Mesa (Figure 4.1.1). This portion of Parran Mesa is dominated by thick exposures of dacite domes, flows, and basalt flows and may represent the original eastern shoulder of the Desert Queen basin.

The fault kinematic data synthesized for this study included 12 measurements taken within the Desert Queen study area. These data were previously compiled into a preliminary structural analysis and stress inversion (Faulds unpublished data, 2009). This analysis concluded that the stress field at Desert Queen is a homogenous normal faulting regime. Faults mapped in the field are primarily normal faults, with some faults showing minor components of oblique slip. These observations are consistent with the more regional structural analysis and stress inversion completed in this study. Most faults in the area strike north-northeast, specifically from ~10-35° (Figure 3.2.3). The calculated stress

regime for the northern Hot Springs Mountains in the vicinity of Desert Queen gives a present-day extension direction of 116°. As such, normal faults striking 026° with a dip of 60° have the highest slip tendency. Therefore, most of the faults within the study area have high slip and dilation tendency values. Thus, the Desert Queen area is primed for geothermal activity due to the complex structural framework of the basin, as well as the favorable orientation of most of the faults.

4.2 Geothermal Prospects and Temperature-Gradient Wells

The structural complexity recognized within and proximal to the Desert Queen basin is promising for geothermal favorability. Three main favorable structural settings were recognized at Desert Queen, within and proximal to the basin. These include 1) the horse-tailing southern termination of the Desert Queen fault zone in the western part of Parran Mesa (Location A in Figure 3.2.11), 2) the left step over/relay ramp between the Desert Queen fault zone and the Power Line fault (Location B in Figure 3.2.11), and 3) the horse-tailing northern termination of the Power Line fault into the Desert Queen basin (Location C in Figure 3.2.11). There is significant overlap of two of these structural settings further increasing structural complexity and likely enhancing permeability within these “hybrid” zones (location D in Figure 3.2.11). The overlap between the southern termination of the Desert Queen fault zone and the step over to the Power Line fault is proximal to the deepest known elevated temperature gradient at Desert Queen (Location D in Figure 3.2.11, and well Strat test 3 in Figure 4.2.1). The other overlap between the step over from the Desert Queen fault zone to the Power Line fault and the northern termination of the Power Line fault is proximal to the hottest thermal gradient at Desert

Queen (Location E and well TG-1 in Figure 3.2.11). The colocation of these hybrid settings with significant direct evidence in the form of measured temperatures points to these zones as obvious targets for continued exploration.

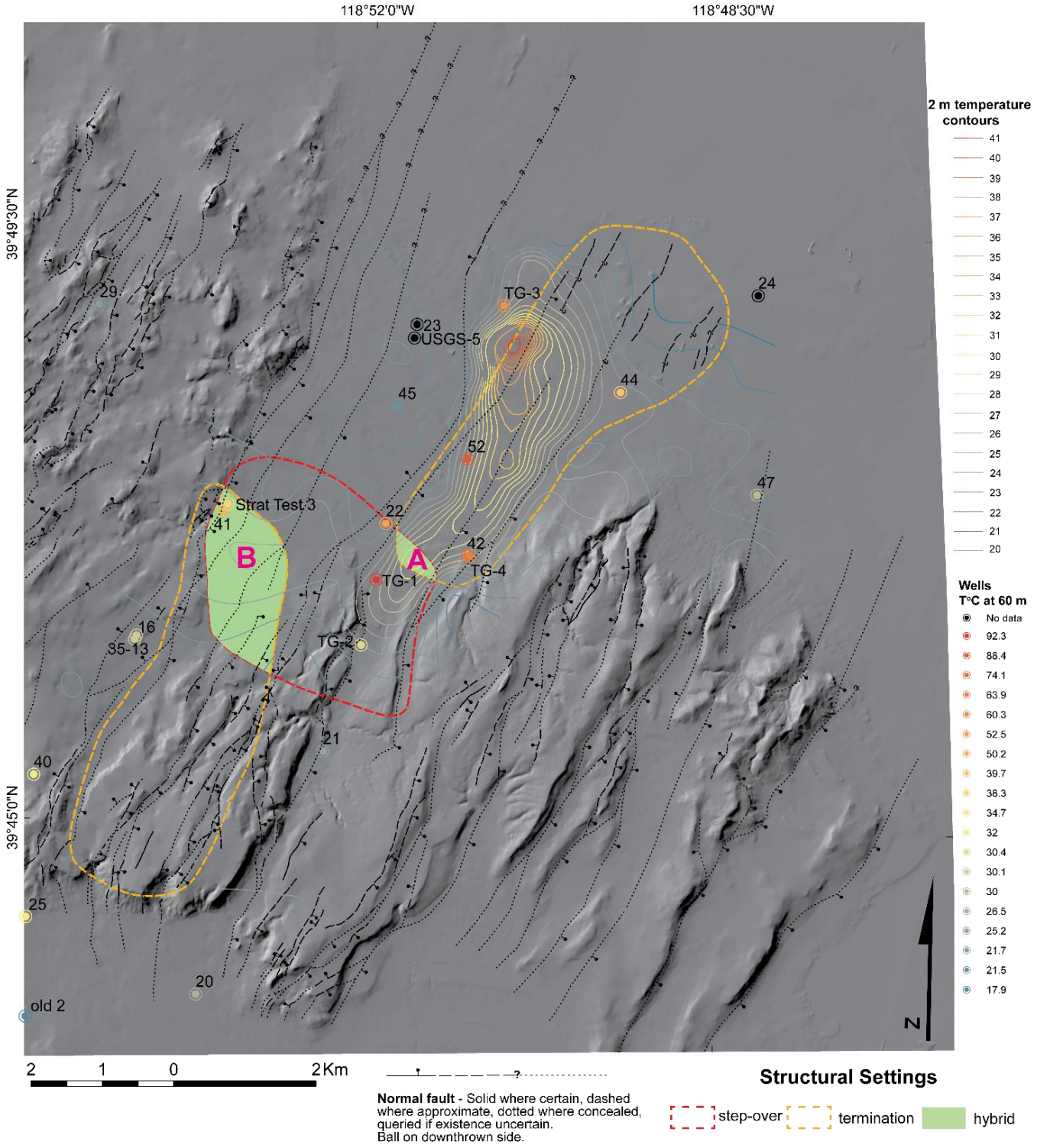

Figure 4.2.1. Structural settings and 2 m temperature contours overlain on DEM hillshade. Detailed fault map is superimposed. Location of wells included (colored according to relative temperature, where warmer colors are hotter wells). Locations discussed in text are labeled with pink letters.

Some additional intricacies exist that also warrant further investigation. For example, the Gravity fault within the basin projects southward into Parran Mesa and bisects the step over from the Desert Queen fault zone to the Power Line fault. As the Gravity fault loses displacement along-side the Desert Queen fault zone, it breaks into at least two mapped splays within the interpreted step-over zone (Figure 4.2.1). The projected intersection of this fault with the Desert Queen fault zone at depth could facilitate fluid flow into the shallow portion of the geothermal system (Figure 4.2.2).

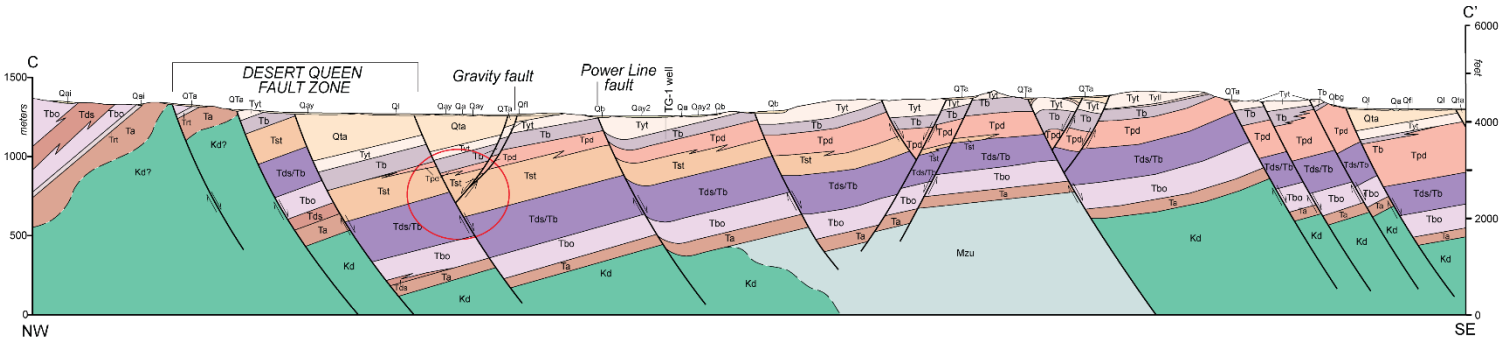

Figure 4.2.2. Cross section D-D' (see Figure 2.2.2 and Plate 1 for location). Location of Desert Queen fault zone, Gravity fault, and Power Line fault are annotated. Red circle denotes fault intersection at depth discussed in text. See plate 1 for unit descriptions.

TG well data at Desert Queen are significant in discerning potential geothermal prospects. Temperatures measured in wells are potential direct evidence of possible geothermal fluid upwellings. A relatively large amount of TG wells has been drilled at Desert Queen (Figure 4.2.1). Well data cover much of the Desert Queen basin, but there are some significant gaps that may warrant potential further investigation or new drilling. Temperature gradients in the Great Basin are generally elevated above global background, due to crustal thinning, and average ~15 to 80°C/km (Blackwell and

Richards, 2004; Coolbaugh et al., 2005; Hinz et al., 2015). Conservatively, a temperature gradient above ~100°C/km was considered anomalous for this region for the purposes of this study.

The four most recent TG wells drilled at Desert Queen (A, Figure 4.2.3) were all drilled along or proximal to the Power Line fault (Figure 4.2.1). The locations of these wells were guided by the 2 m temperature anomaly delineated prior to the ca. 2010 drilling (Coolbaugh et al., 2007, 2010; Figure 3.4.1). In addition to these wells, four older wells drilled in the vicinity of the Power Line fault all exhibit elevated shallow temperatures (Figures 4.2.1 and 4.2.3). It is worth noting, however, that every well in the vicinity of the Power Line fault (A and C, Figure 4.2.3) has a temperature reversal or exhibits isothermal character at some depth other than wells TG-2 and 22 (which may not be drilled deep enough to encounter a potential reversal). The temperature gradients of all wells in the vicinity of the Power Line fault zone are indicative of convective geothermal fluids that likely represent an intersection with an outflow plume.

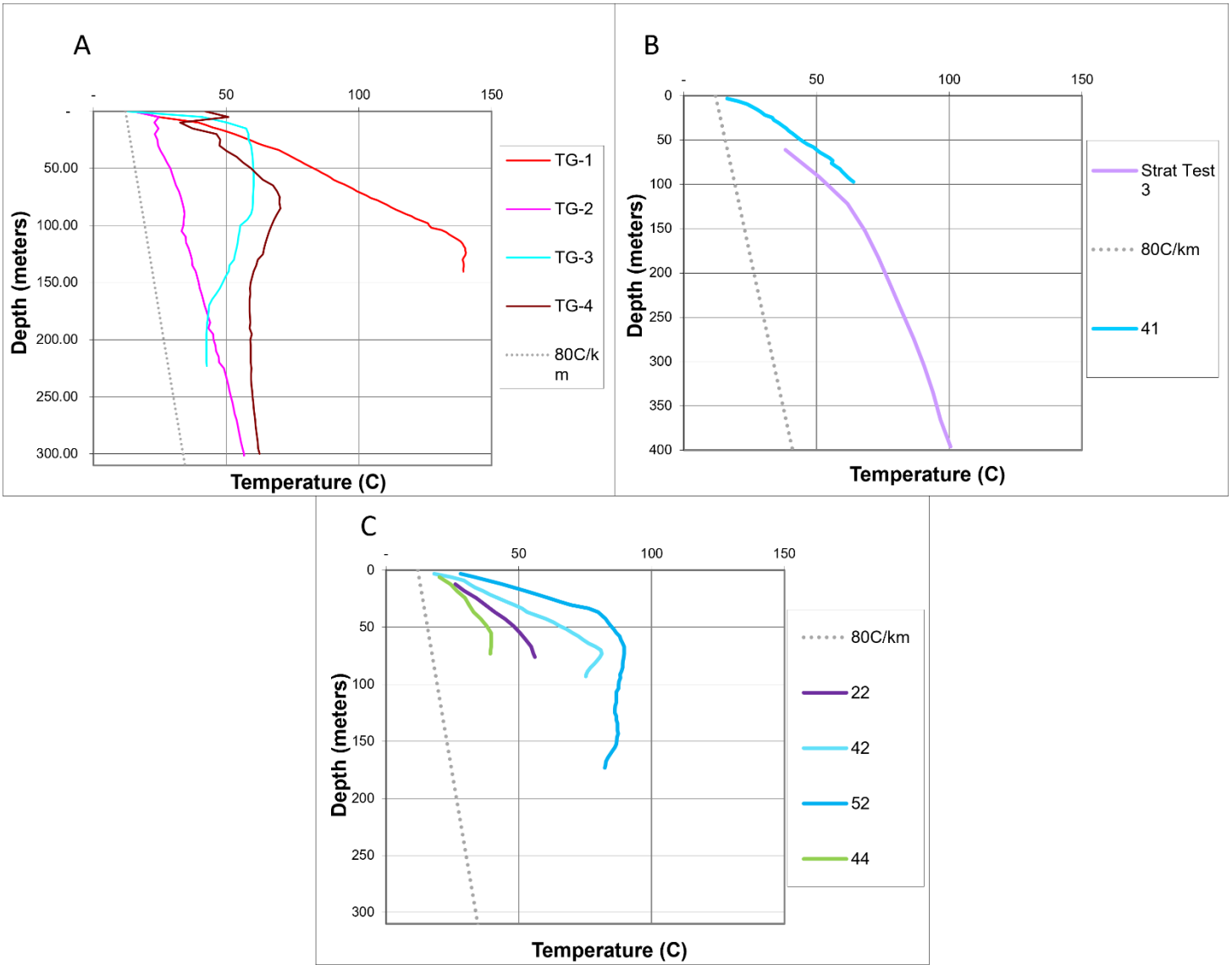

Figure 4.2.3. A) Temperature profiles of the four TG wells drilled in 2010 by Magma Energy. **B)** Temperature profiles of well 41 and Strat Test 3 well. **C)** Selected temperature profiles from older wells in the vicinity of the Power Line fault. TG-1 has the highest thermal gradient of any well at Desert Queen, and it becomes isothermal at a depth of ~120 m. Strat Test 3 has the next highest thermal gradient within the Desert Queen basin. All wells are compared to a relatively high background gradient of 80°C/km.

Given that many of the wells drilled in the area have varying temperature gradients (e.g., temperature reversals, isothermal character at some depth) or are drilled to

less than 100 m depth, the Strat Test 3 well to the west was the only well selected for defining the temperature gradient in the area for greater depths. Strat Test 3 is located adjacent to the range front strand of the Desert Queen fault within one of the hybrid favorable structural settings (Figure 4.2.1). It was drilled to a moderate total depth of ~400 m and exhibits a relatively linear temperature profile indicative of conduction (Figure 4.2.3B). Additionally, the directly adjacent well 41 exhibits a similar temperature profile as Strat Test 3 (Figures 4.2.1 and 4.2.3B). Conveniently, well 41 fills a data gap that exists in Strat Test 3 from 0-60 m below ground level. The linear temperature profile of Strat Test 3 was projected to a depth of 1 km to calculate a temperature gradient of 192°C/km, which is roughly double the background gradient considered for the region. Notably, the occurrence of the hottest shallow temperatures measured in TG wells generally spatially correspond with the 2 m temperature anomaly (Figure 4.2.1). The 2 m temperature survey also delineated a milder shallow anomaly in the vicinity of Strat Test 3 (Figure 4.2.1). The spatial correlation of the 2 m temperature anomaly with deeper temperature anomalies outlined by TG wells delineates a large extent of elevated shallow subsurface temperatures (Figures 3.3.1, 3.4.1, and 4.2.1).

Two major geothermal prospects are identified based on the correspondence favorable structural settings with temperature anomalies derived from TG wells and 2 m temperature data. The first major prospective zone is the small hybrid structural setting just to the north-northeast of the TG-1 well (location A in Figure 4.2.1). Multiple lines of direct evidence and structural complexity point to this zone as a potential geothermal upwelling. The temperature profile in TG-1 also indicates the presence of convective fluids, and TG-1 is the only such well that does not have a temperature reversal in this

area (Figure 4.2.3B). Continued exploration in the vicinity of this location is important to delineate whether the TG-1 well has indeed encountered an upwelling, as well as if the Power Line fault may host an upwelling zone. The second major prospective zone occupies the larger hybrid structural setting to the west (location B in Figure 4.2.1). Within this setting multiple features and lines of evidence suggest a favorable environment for geothermal upwelling, including the hybrid favorable structural setting, the projected intersection of the Gravity fault with the termination Desert Queen fault, and the moderate 2 m temperature anomaly. The highly elevated temperature gradient in Strat Test 3 is promising for geothermal activity, but the conductive temperature profile implies a lack of intersect with convective fluids. This area is still highly prospective, however, and it is possible that a convective system may be present nearby.

4.3 Play Fairway Analysis

The fine-scale geothermal play fairway analysis led to the generation of three predictive maps that are useful for vectoring into favorable areas for geothermal activity at Desert Queen: 1) the “fairway”, 2) direct evidence, and 3) overall favorability model. The fairway map was generated from combining the regional-, intermediate-, and detailed-scale permeability models with regional heat flow. The fairway map is a favorability map that highlights areas where permeability is enhanced based on the conjunction of weighted parameters, the most important of which are the detailed-scale favorable structural settings (Figure 3.7.2). The intermediate-scale permeability parameters were given additional weight in this study as compared to the regional Nevada play fairway analysis due to detailed geologic mapping and geophysical surveys

in the area. The favorability scale generated in the analysis is a unitless scale ranging from -4.38 to +4.13, with negative values (cooler colors, Figure 4.3.1A) representing low favorability, and positive values (warmer colors, Figure 4.3.1A) denoting high favorability. Taken on its own, the fairway map highlights broader zones of potential geothermal activity. The highest fairway scores are generally within the identified favorable structural settings (Figure 4.3.1A). However, the very high gravity gradient along the Desert Queen fault zone (Figure 3.6.1) resulted in a relatively high fairway score in this region (Figure 4.3.1A). Another area of high favorability is proximal to the Holocene fault traces within the inferred termination of the Power Line fault (Location C in Figure 3.2.11; Figure 2.2.2).

Something to consider in further play fairway analyses at this scale are the usage of abrupt favorable structural setting boundaries. The resulting fairway model indicates relatively high favorability directly adjacent to relatively low favorability across the structural settings boundary. This could be remedied by applying a gradational boundary around each structural setting polygon, buffered according to certainty. This is probably more realistic considering that delineation of the boundaries of the favorable structural settings is somewhat subjective.

The direct evidence map (Figure 4.3.1B) was generated using three inputs, TG well data, 2 m temperature data, and geothermometry. Higher probabilities on this map are calculated relative to regional temperature gradients and degrees above background of 2 m temperatures. The scale for the direct evidence model is simply the probability of occurrence of a geothermal system from 0-100%. The highest direct evidence score of 85 correlates with the hottest TG well (TG-1, Figures 3.3.1 and 4.3.1B). The pronounced 2

m temperature anomaly at Desert Queen has a large influence in the direct evidence model with a score of 50 over most of its extent (Figures 3.4.1 and 4.3.1B).

The overall favorability model (Figure 4.3.1C) was generated by combining the fairway model with direct evidence. The favorability model serves as the most useful tool in targeting potential zones of geothermal activity/upwelling of geothermal fluids. Areas with high favorability scores (>0.40) denote high permeability potential due to structural complexity and favorably oriented faults, as well as promising direct evidence in the form of measured temperatures. Evident in the favorability model are two potential targets with the highest scores of >0.83 (light pink colors in Figure 4.3.1C). These two areas correspond with the hottest TG wells in the area (Figure 4.2.1), as well as the two hybrid favorable structural settings (Locations D and E in Figure 4.2.1).

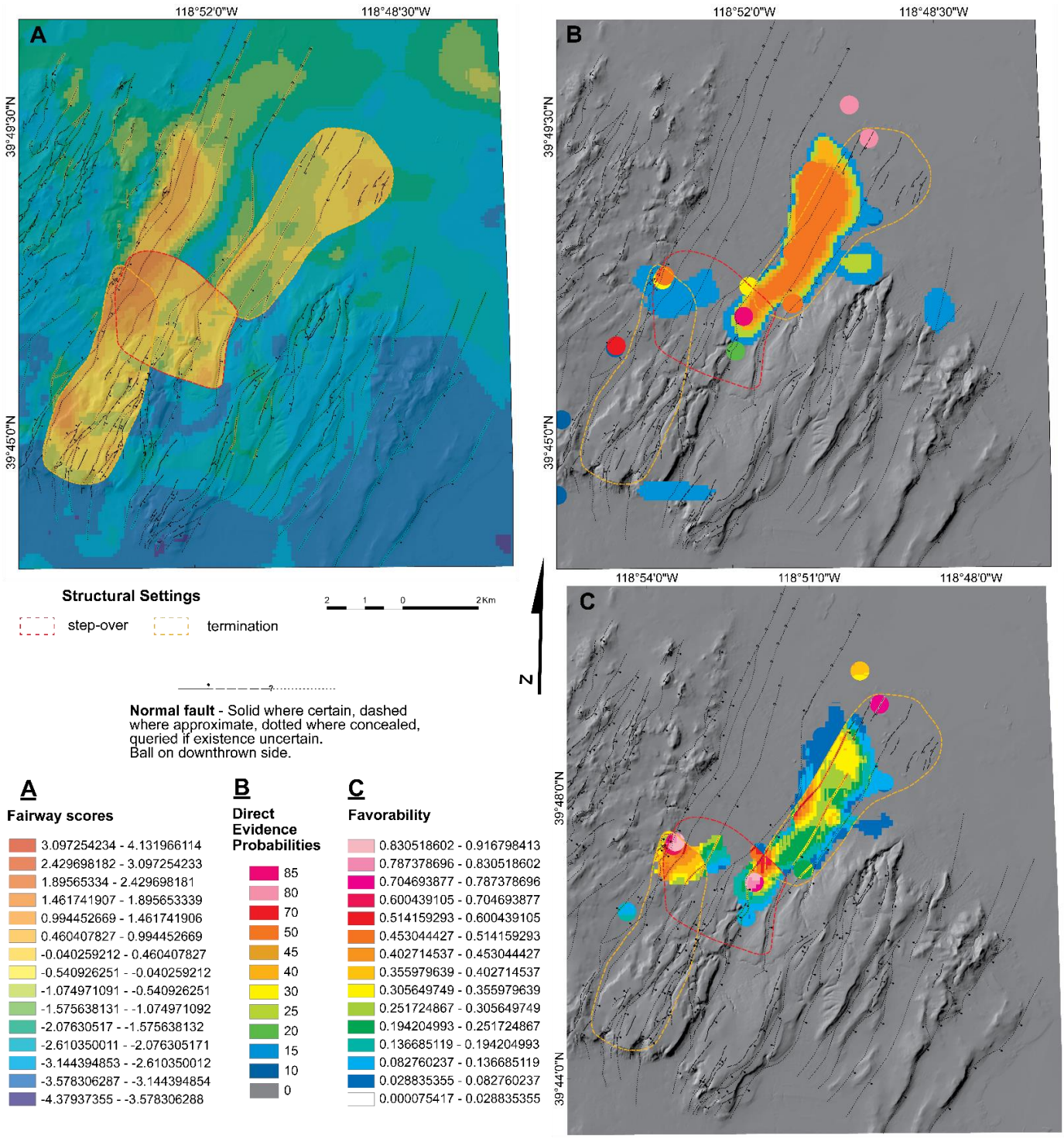

Figure 4.3.1. A) Desert Queen play fairway map overlain on DEM hillshade. Warm colors indicate higher fairway values. **B)** Direct evidence, play fairway map overlain on DEM hillshade. Inputs into direct evidence probabilities are TG wells, 2 m temperatures, and geothermometry. Warmer colors indicate higher probability of occurrence of a >130°C geothermal system. **C)** Play fairway favorability model. Warmer colors equate to higher geothermal favorability. Detailed fault map and outlines of favorable structural settings are superimposed.

4.4 Additional Comparisons

Datasets not included in the play fairway analysis that may potentially indicate the presence of geothermal activity were compared with the favorability model to add further clarity and certainty to the results. The two datasets most indicative of potential geothermal activity that were not included as a parameter in the play fairway analysis were magnetic and MT data (Figures 3.6.2 and 3.6.5).

The two highest favorability zones spatially correlate with the magnetic low anomalies (labeled as A and B in Figure 4.4.1). The broader high favorability zone is proximal to the southern end of the elongated broad magnetic low that covers the altered basement rocks exposed in the footwall of the Desert Queen fault at location A. It is also proximal to a more localized magnetic low that straddles the boundary of the Desert Queen fault termination and presumably extends to the southwest. At location B the higher favorability scores extend just to the north of a very small magnetic low at the intersection of two strands of the Power Line fault.

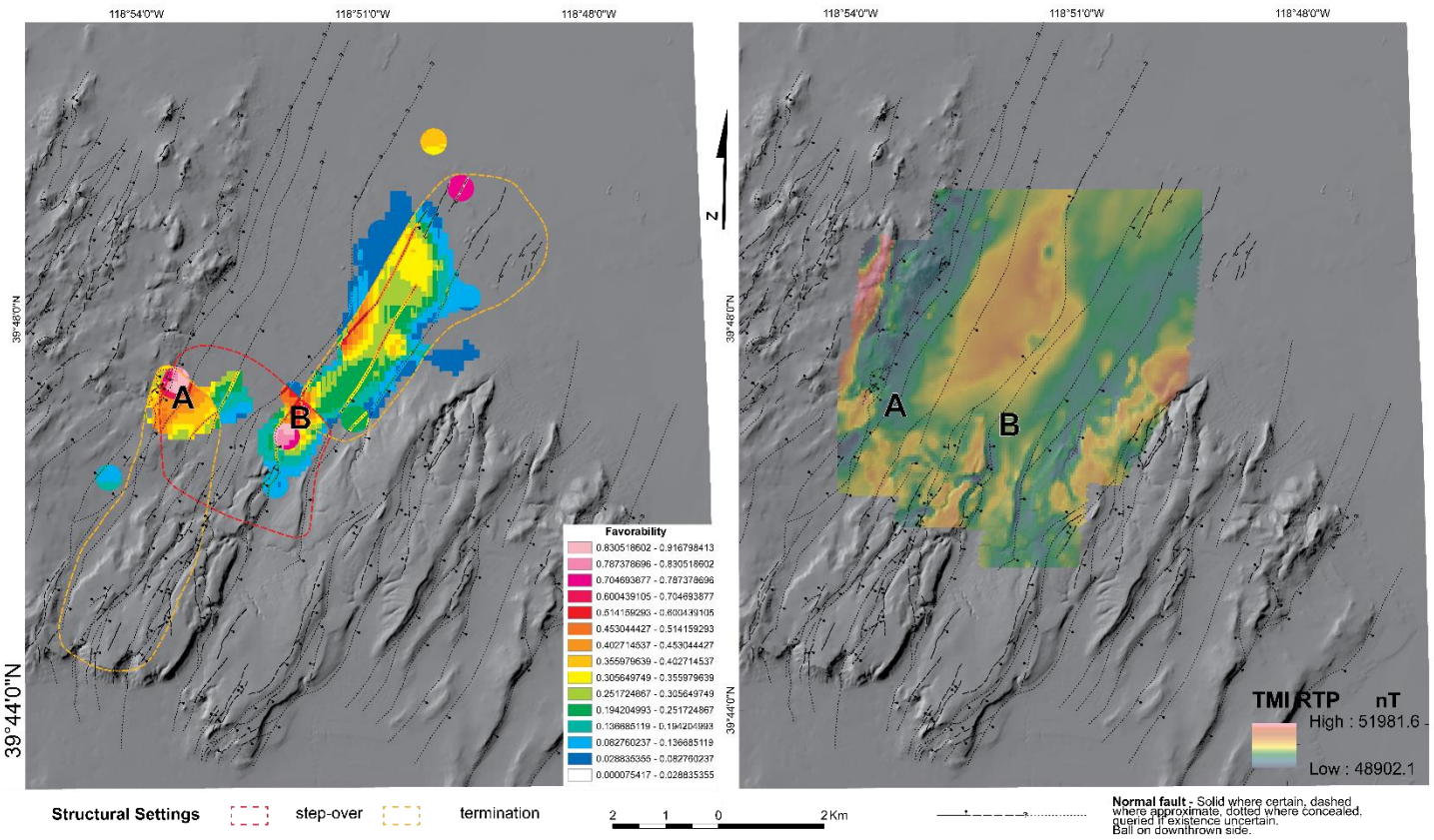

Figure 4.4.1. Spatial comparison between favorability and magnetic maps. Locations discussed in text are denoted.

More profound is the direct correlation of the two high favorability zones with anomalies outlined in the MT data. Location A is directly correlative with the elliptical low resistive anomaly that occurs from ~900 m depth to at least 2400 m depth (Figures 3.6.5 and 4.4.2). Interestingly, location B directly corresponds with the elongated high resistive anomaly just to the southeast of the low resistive anomaly at depths of 900-1200 m. Location A and B both reside within the broader low resistivity anomaly that covers the Desert Queen basin at shallow depths of 300-600 m (Figure 3.6.5A, B). The implications of these spatial relationships are potentially very promising. The direct correlation of high predicted geothermal favorability with a distinct elliptical low

resistivity anomaly at location A may indicate clay alteration at depth that may result from upwelling geothermal fluids in this location.

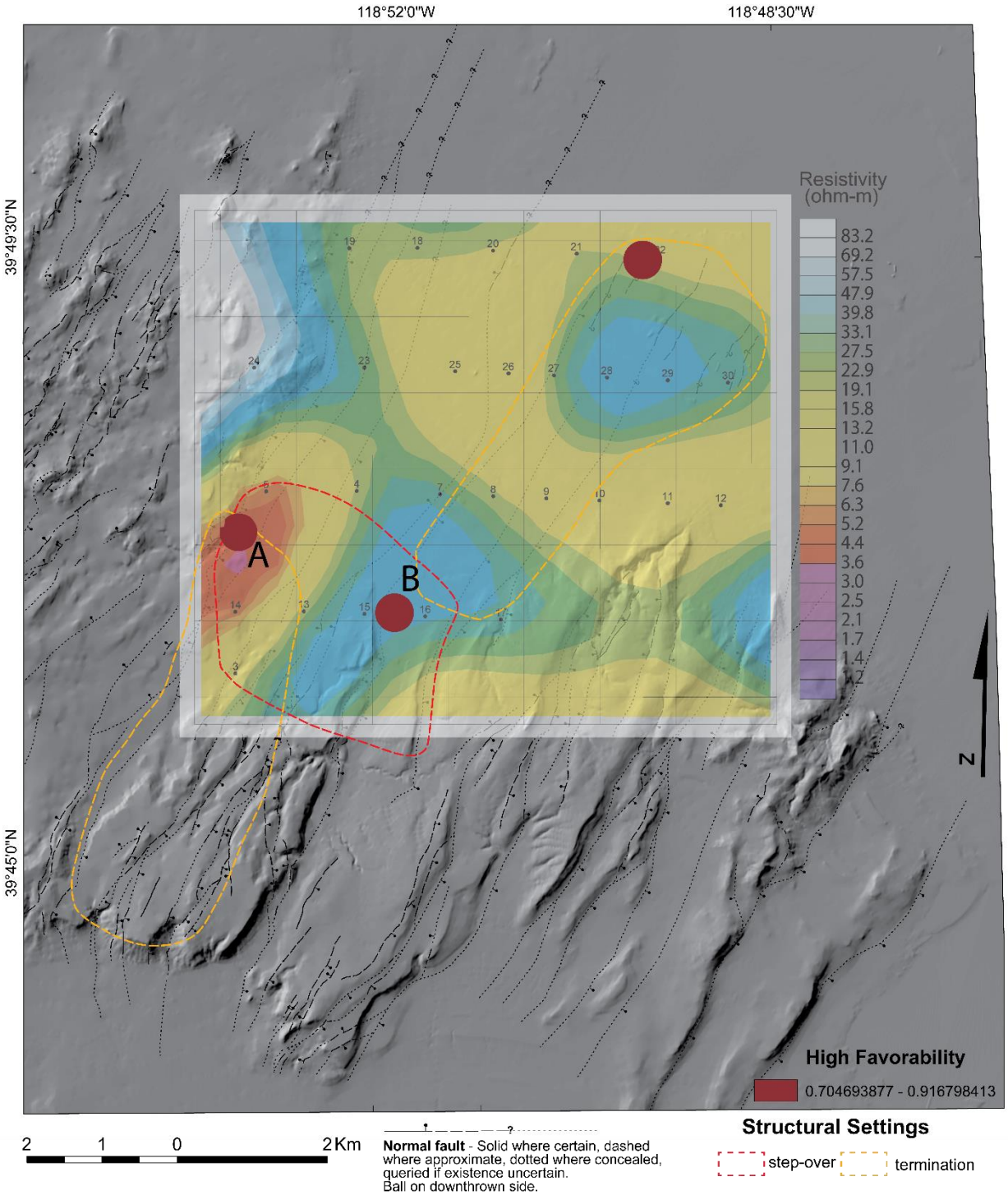

Figure 4.4.2. MT depth slice at 1200 m, high favorability areas (>0.70), and favorable structural settings.

4.5 Continued Exploration

The two highly favorable zones described above represent very promising sites for future exploration efforts and potential drilling at Desert Queen. Additional TG drilling at location A is important to confirm the deeper convective fluids at this location. Placing two TG wells to intersect the Power Line fault both to the north and south of TG-1 at depths of ~500 m would be optimal in targeting a potential upwelling zone along the fault. Exploration efforts at location B would benefit from three to four deeper TG wells (300-500 m depth) (Figure 4.5.1). A well placed just to the east of Strat Test 3 would be important to determine if convective fluids are present in the vicinity, as Strat Test 3 intersects the Desert Queen range-front fault strand at a relatively shallow depth. Two to three additional wells to the east-southeast of Strat Test 3 within the high favorability zone (Figure 4.3.1C), drilled progressively deeper from west to east to target each strand of the Desert Queen fault zone at depth (Figure 4.5.1), would serve to elucidate any potential fluid flow pathways in this area. A promising deeper TG drill target in this area would be the intersection of the terminating and horse-tailing Desert Queen fault zone with the antithetic Gravity fault at depth. This intersection is estimated at a depth of 550 m and thus may be an economically viable target. This potentially high permeability zone could represent one of the main fluid flow pathways at Desert Queen. If this target proves to be fruitful, a slim hole drilled to basement depths (~1000-1200 m) in this area (Figure 4.5.1) may encounter the geothermal reservoir.

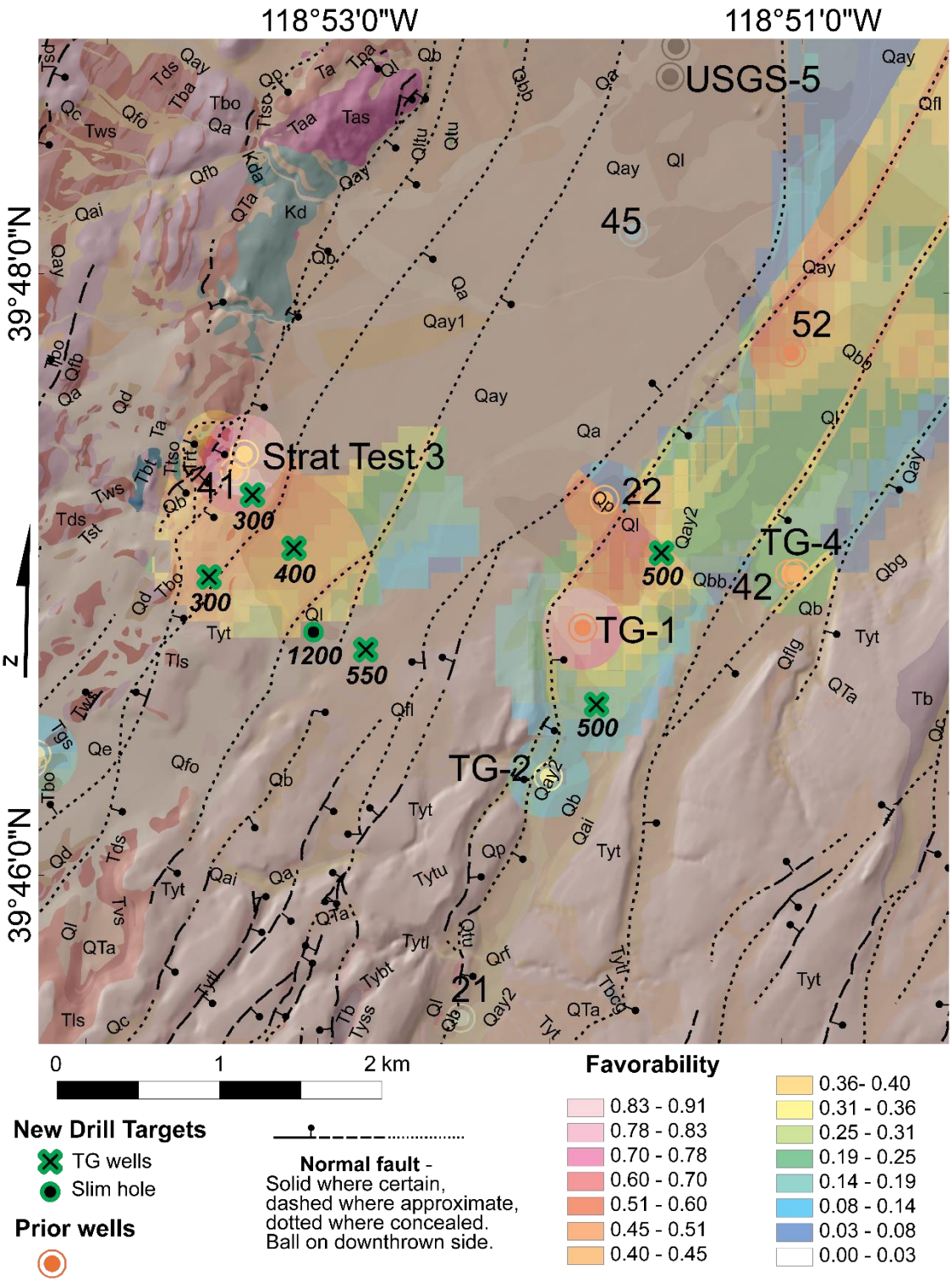

Figure 4.5.1. Proposed new drill targets discussed in text superimposed on detailed geologic map and play fairway favorability model. New drill targets are labeled with proposed total depths in meters. See plate 1 for geologic unit descriptions.

5. Conclusion and Recommendations

This study has expanded prior exploration at Desert Queen by synthesizing existing and integrating new geological, geochemical, geophysical, and well data. This multidisciplinary approach has greatly elucidated the structural framework and potential structural controls on geothermal activity. Additionally, the deployment of geothermal play fairway analysis at a fine scale at Desert Queen has delineated two particularly favorable zones capable of hosting geothermal fluids. These results should reduce the risk in future drilling and exploration, as multiple lines of evidence allow for increased certainty in the presence of geothermal fluids in these areas. As such, continued exploration with the new drill targets have been recommended based on the results of this study.

The Desert Queen basin is a complex composite basin consisting of at least two half grabens bisected by a narrow horst block. The major Desert Queen fault zone, which bounds the western edge of the basin, consists of as many as four strands that lose displacement southward as the basin terminates. This results in structurally complex basin margins consisting of fault terminations, subsurface intersections, and step overs. Five favorable structural settings have been recognized within and proximal to the Desert Queen basin, two of which are hybrid overlaps (locations A and B, Figure 4.2.1). Additionally, elevated temperature gradients have been measured within the Desert Queen basin.

Location A (Figure 4.2.1) is a highly favorable zone defined by the play fairway analysis. This location is marked by overlap between the step over/relay ramp between

the Desert Queen fault zone and the Power Line fault, elevated 2 m temperatures, an elongated magnetic low anomaly, a shallow low resistivity anomaly, and multiple TG wells with elevated gradients. Furthermore, the TG-1 well is drilled just to the south of this location and has intersected convective, higher temperature fluids (143^{o}C) at a shallow depth (~140 m). The second location recognized as highly favorable by the play fairway analysis is location B (Figure 4.2.1). This location is a similar setting to location A, where the southern termination of the Desert Queen fault zone overlaps with the step over/relay ramp between the Desert Queen fault zone and the Power Line fault. Multiple lines of evidence point to this area hosting geothermal fluids, such as a moderate 2 m temperature anomaly, a magnetic low, a deeper low resistivity anomaly, and a deep well with an elevated temperature gradient. Although the well in this area has a conductive temperature gradient and does not intersect a geothermal upwelling, the elevated gradient and temperature may indicate the presence of a nearby upwelling. Location B is also proximal to the inferred intersection of the Desert Queen fault zone and the Gravity fault at depth. New drill targets were placed based on the above lines of evidence, as well as the consideration of fault intersections at the surface and at depth. New drill targets recommended in this study serve to target potential geothermal upwellings and reduce the risk of future drilling in encountering the geothermal reservoir at depth.

This study has shown that the geothermal play fairway analysis is a useful tool in the middle to late stages of exploration, particularly in a blind geothermal system, where distinct favorable areas that represent high permeability and high heat zones can be delineated. Desert Queen has been subject to substantive exploration and is a relatively data dense prospect with high measured temperatures (140°C) and promising

geothermometry (~200°C). The synthesis of these data into a fine-scale play fairway analysis has suggested multiple potential upwellings at Desert Queen that may be capable of hosting a geothermal power plant.

References

Angelier, J., Colletta, B., and Anderson, R.E., 1985, Neogene paleostress changes in the Basin and Range: A case study at Hoover Dam, Nevada-Arizona: Geological Society of America Bulletin, v. 96, p. 347–361, doi: 10.1130/0016-7606(1985)96<347:NPCITB>2.0.CO;2.

Athens, N.D., Ponce, D.A., Jayko, A.S., Miller, M., McEvoy, B., Marcaida, M., Mangan, M.T., Wilkinson, S.K., McClain, J.S., Chuchel, B.A., and Denton K.M, 2014, Magnetic and gravity studies of Mono Lake, east-central California: U.S. Geological Survey Open File Report 2014-1043, 14 p.

Atwater, T., and Stock, J., 1998, Pacific–North America plate tectonics of the Neogene southwestern United States: An update: International Geology Review, v. 40, p.375–402.

Allmendinger, R.W., Gephart, J.W., Marrett, R.A., 1989, Notes on fault slip analysis: Geological Society of America short course on “quantitative interpretation of joints and faults”, 59 p.

Augustine, C., Ho, J., and Blair, N., 2019, GeoVision analysis supporting task force report: Electric sector potential to penetration. Golden, CO: National Renewable Energy Laboratory.NREL/ TP-6A20-71833, 93 p.

Axelrod, D. 1., 1956, Mio-Pliocene floras from west-central Nevada: University of California Publication in Geologic Science, v. 33, p. 1-322.

Bell, J.W., Caskey, S.J., Ramelli, A.R., and Guerrieri, L. 2004, Pattern and rates of faulting in the central Nevada seismic belt, and paleoseismic evidence for prior beltlike behavior: Bulletin of the Seismological Society of America, v. 94, no. 4, p. 1229–1254, doi:10.1785/012003226.

Bell, J., and Ramelli, A., 2007, Active faults and neotectonics at geothermal sites in the western Basin and Range: Preliminary results: Geothermal Resources Council Transactions, v. 31, p. 375–378.

Bennett, R.A., Wernicke, B.P., Niemi, N.A., Friedrich, A.M., and Davis, J.L., 2003, Contemporary strain rates in the northern Basin and Range province from GPS data: Tectonics, v. 22, 31 p. doi:10.1029/2001TC001355.

Benoit, W.D., Hiner, J.E., and Forest, R.T., 1982, Discovery and geology of the Desert Peak geothermal field: A case history: Nevada Bureau of Mines and Geology Bulletin, 82 p.

Benoit, D., 2010, Desert Queen Chemistry Results and Interpretation: unpublished report, 2 p.

Benoit, D., 2011, The Desert Queen geothermal prospect: unpublished report, 17 p.

Blackwell, D.D., Richards, M., Wisian, K.W., and Steele, J.L, 1999, System specific geothermal gradient/heat flow data base for the western United States: Geothermal Resources Council Transactions, v. 23, p. 461-466.

Blackwell, D.D., and Richards, M., 2004, Geothermal map of North America: American Association of Petroleum Geologists, map item number 423, scale 1:6,500,000

Blakely, R.J., and Simpson, R.W., 1986, Approximating edges of source bodies from magnetic or gravity anomalies: Geophysics, v. 51, p. 1494-1498

Brown, E.H., and Gehrels, G.E., 2007, Detrital zircon constraints on terrane ages and affinities and timing of orogenic events in the San Juan Islands and North Cascades, Washington: Canadian Journal of Earth Sciences, v. 44, p. 1375–1396, doi:10.1139/e07-040.

Brown, S., Coolbaugh, M., DeAngelo, J., Faulds, J., Fehler, M., Gu, C., Queen, J., Treitel, S., Smith, C., and Mlawsky, E., 2020, Machine learning for natural resource assessment: An application to the blind geothermal systems of Nevada: Geothermal Resources Council Transactions, v. 44, p. 920-932.

Caine, J.S., Evans, J.P., and Forster, C.B., 1996, Fault zone architecture and permeability structure: Geology, v. 24, p. 1025–1028, doi: 10.1130/0091-7613(1996)024<1025:FZAAPS>2.3.CO.

Cockett, R., Kang, S., Heagy, L.J., Pidlisecky, A., and Oldenburg, D.W., 2015. SimPEG: An open source framework for simulation and gradient based parameter estimation in geophysical applications: Computers & Geosciences, v. 85, p. 142–154.

Colgan, J.P., Dumitru, T.A., and Miller, E.L., 2004, Diachroneity of Basin and Range extension and Yellowstone hotspot volcanism in northwestern Nevada: Geology, v. 32, p. 121-124.

Coolbaugh, M., Zehner, R., Kreemer, C., Blackwell, D., Oppliger, G., Sawatzky, D., Blewitt, G., Pancha, A., Richards, M., Helm-Clark, C, Shevenell, L., Raines, G., Johnson, G., Minor, T., and Boyd, T, 2005, Geothermal potential map of the Great Basin, western United States: Nevada Bureau of Mines and Geology Map 151.

Coolbaugh, M.F., Raines, G.L., Zehner, R.E., Shevenell, L., and Williams, C.F., 2006, Prediction and discovery of new geothermal resources in the Great Basin: Multiple evidence of a large undiscovered resource base: Geothermal Resources Council Transactions, v. 30, p. 867–874.

Coolbaugh, M., Sladek, C., Faulds, J., Zehner, R., and Oppliger, G., 2007, Use of rapid temperature measurements at a 2-meter depth to augment deeper temperature gradient drilling: Proceedings, 32nd Workshop on Geothermal Reservoir Engineering, Stanford University, Stanford, California, SGP-TR-183, p. 109-116.

Coolbaugh, M., Lechler, P., Sladek, C., and Kratt, C., 2009, Carbonate tufa columns as exploration guides for geothermal systems in the Great Basin: Geothermal Resources Council Transactions, v. 33, p. 461–466.

Coolbaugh, M.F.,Sladek, C., and Kratt, C., 2010, Compensation for seasonal and surface effects of shallow (two-meter) temperature measurements: Geothermal Resources Council Transactions, v. 34, p. 850-856.

Craig, J.W., Faulds, J.E., Shevenell, L.A., and Hinz, N.H., 2017, Discovery and analysis of a potential blind geothermal system in southern Gabbs Valley, western Nevada: Geothermal Resource Council Transactions, v. 41, p. 2258 - 2264.

Craig, J.W., 2018, Discovery and analysis of a blind geothermal system in southeastern Gabbs Valley, western Nevada [M.S. Thesis]: University of Nevada, Reno, 110 p.

Craig, J.W., Faulds, J.E., Hinz, N.H., Earney, T.E., Schermerhorn, W.D., Siler, D.L., Glen, J.M., Peacock, J., Coolbaugh, M.F., and Deoreo, S.B., 2021, Discovery and analysis of a blind geothermal system in southeastern Gabbs Valley, western Nevada, USA: Geothermics, v. 97,18 p.

Davis, D.W., Williams, I.S., and Krogh, T.E., 2003, Historical development of zircon geochronology: Reviews in Mineralogy and Geochemistry, v. 53, no. 1, p. 145-181.

Dickinson, W.R., and Gehrels, G.E., 2009, Use of U–Pb ages of detrital zircons to infer maximum depositional ages of strata: A test against a Colorado Plateau Mesozoic database: Earth and Planetary Science Letters, v. 288, p. 115–125, doi:10.1016/j.epsl.2009.09.013.

Doust, H., 2010, The exploration play: what do we mean by it?: American Association of Petroleum Geologist Bulletin, v. 94, p. 1657-1672.

Faulds, J.E., and Varga, R., 1998, The role of accommodation zones and transfer zones in the regional segmentation of extended terranes, in Faulds J.E., and Stewart, J.H., eds., Accommodation Zones and Transfer Zones: The Regional Segmentation of the Basin and Range Province: Geological Society of America Special Paper 323, p. 1-45.

Faulds, J.E., and Garside, L.J., 2003, Preliminary geologic map of the Desert Peak – Brady geothermal fields, Churchill County, Nevada: Nevada Bureau of Mines and Geology Open-File Report 03-27.

Faulds, J.E., Coolbaugh, M.F., Blewitt, G., and Henry, C.D., 2004, Why is Nevada in hot water? Structural controls and tectonic model of geothermal systems in the northwestern Great Basin: Geothermal Resources Council Transactions, v. 28, p. 649–654.

Faulds, J.E., Henry, C.D., and Hinz, N.H., 2005, Kinematics of the northern Walker Lane: An incipient transform fault along the Pacific–North American plate boundary: Geology, v. 33, p. 505-508, doi:10.1130/G21274.1.

Faulds, J.E., Coolbaugh, M.F., Vice, G.S., and Edwards, M.L., 2006, Characterizing structural controls of geothermal fields in the northwestern Great Basin: A progress report: Geothermal Resources Council Transactions, v. 30, p. 69–76.

Faulds, J.E., and Henry, C.D., 2008, Tectonic influences on the spatial and temporal evolution of the Walker Lane: An incipient transform fault along the evolving Pacific – North American plate boundary, in Spencer, J.E., and Titley, S.R., eds, Ores and orogenesis: Circum Pacific tectonics, geologic evolution, and ore deposits: Arizona Geological Society Digest, p. 437–470.

Faulds, J. E., and Green, H., 2009, Stratigraphic and structural framework of the Desert Queen Mine area, Hot Springs Mountains, Churchill County, Nevada: implications for geothermal resources (Final Draft Report): Unpublished Report for Magma Energy (U.S.) Corp., 15 p.

Faulds, J.E., Coolbaugh, M.F., Benoit, D., Oppliger, G., Perkins, M., Moeck, I., and Drakos, P., 2010, Structural controls of geothermal activity in the northern Hot Springs Mountains, western Nevada: The tale of three geothermal systems (Brady's, Desert Perk, and Desert Queen): Geothermal Resources Council Transactions, v. 34, p. 675-683.

Faulds, J.E., Hinz, N.H., Coolbaugh, M.F., Cashman, P.H., Kratt, C., Dering, G., Edwards, J., Mayhew, B., and Mclachlan, H., 2011, Assessment of favorable structural settings of geothermal systems in the Great Basin, western USA: Geothermal Resources Council Transactions, v. 35, p. 777–783.

Faulds. J.E., Hinz, N., Kreemer, C., and Coolbaugh, M., 2012, Regional patterns of Geothermal activity in the Great Basin region, western USA: Correlation with strain rates and distribution of geothermal fields: Geothermal Resources Council Transactions, v. 36, p. 897-902.

Faulds, J.E., Hinz, N.H., Coolbaugh, M.F., Shevenell, L.A., Siler, D.L., dePolo, C.M., Hammond, W.C., Kreemer, C., Oppliger, G., Wannamaker, P., Queen, J.H., and Visser, C., 2015, Integrated geologic and geophysical approach for establishing geothermal play fairways and discovering blind geothermal systems in the Great Basin region, western USA: Final submitted report to the Department of Energy (DE-EE0006731), 106 p.

Faulds, J.E., and Hinz, N.H., 2015, Favorable tectonic and structural settings of geothermal systems in the Great Basin region, western USA: Proxies for discovering blind geothermal systems: Proceedings, World Geothermal Congress, Melbourne, Australia, 19-25 April, 2015, 6 p.

Faulds, J. E., Hinz, N.H., Coolbaugh, M.F., Shevenell, L.A., and Siler D.L, 2016, The Nevada play fairway project — Phase II: Initial search for new viable geothermal systems in the Great Basin region, western USA: Geothermal Resources Council Transactions, v. 40, p. 535-540.

Faulds, J.E., Hinz, N., dePolo, C., Hammond, W., Kreemer, C., Shevenell, L., Coolbaugh, M., Queen, J., Siler, D., Visser, C., and Wannamaker, P., 2018, Discovering blind geothermal systems in the Great Basin region: An integrated geologic and geophysical approach for establishing geothermal play fairways: Final report for budget period 2 (DE-EE0006731): Department of Energy, 110 p.

Faulds, J.E., Hinz, N.H., Coolbaugh, M.F., Ramelli, A., Glen, J.M, Ayling, B.A., Wannamaker, P.E., Deoreo, S.B., Siler, D.L., and Craig, J.W., 2019, Vectoring into potential blind geothermal systems in the Granite Springs Valley area, western Nevada: Application of the play fairway analysis at multiple scales: Proceedings 44th Workshop on Geothermal Reservoir Engineering, Stanford University, Stanford, California, SGP-TR-214, p. 74-84.

Faulds, J.E., Ayling, B., Craig, J., Hinz, N., Glen, J., Siler, D., Coolbaugh, M., Witter, J., and McConville, E., 2020, Final technical report: Discovering blind geothermal systems in the Great Basin region: An integrated geologic and geophysical approach for establishing geothermal play fairways: Final report for all budget periods (DE-EE0006731): Department of Energy, 73 p.

Faulds, J.E., Coolbaugh, M.F., and Hinz, N.H., 2021, Inventory of structural settings for active geothermal systems and late Miocene (~8 ma) to Quaternary epithermal

mineral deposits in the Basin and Range province of Nevada: Nevada Bureau of Mines and Geology Report 58, 28 p.

Ferrill, D.A., Winterle, J., Wittmeyer, G., Sims, D., Colton, S., Armstrong, A., and Morris, A.P., 1999, Stressed rock strains groundwater at Yucca Mountain, Nevada: GSA Today, v. 9, p. 1–8.

Ferrill, D.A., and Morris, A.P., 2003, Dilational normal faults: Journal of Structural Geology, v. 25, p. 183–196, doi:10.1016/S0191-8141(02)00029-9.

Ferrill D.A., Smart, K.J., and Morris, A.P., 2019, Fault failure modes, deformation mechanisms, dilation tendency, slip tendency, and conduits v. seals: Geological Society of London Special Publication 496, p.75-98.

Ferrill, D.A., Smart, K.J., and Morris, A.P., 2020, Resolved stress analysis, failure mode, and fault-controlled fluid conduits: Solid Earth, v. 11, p. 899-908.

Forson, C., Steely, A. N., Cladouhos, T.T., Swyer, M.W., Davatzes, N., Anderson, M., Ritzinger, B., Glen, J., Peacock, J., Schermerhorn, W., Burns, E., and Stelling, P., 2017, Geothermal play-fairway analysis of Washington state prospects: Phase 2 results: Geothermal Resources Council Transactions, v. 41, p. 47.

Fosdick, J.C., and Colgan, J.P., 2008, Miocene extension in the East Range, Nevada: A two-stage history of normal faulting in the northern Basin and Range: Geological Society of America Bulletin, v. 120, p. 1198–1213, doi:10.1130/B26201.1.

Fullagar, P.K., and Pears, G.A., 2007, Towards geologically realistic inversion: Proceedings of Exploration 07: Fifth Decennial International Conference on Mineral Exploration, Toronto. 444–460.

Fullagar, P.K., Pears, G.A., and McMonnies, B., 2008, Constrained inversion of geologic surfaces— Pushing the boundaries: The Leading Edge, v. 27, p. 98–105.

Garcher, L., and Arehart, G., 2008, Origin and characterization of geothermal waters at Desert Queen, Nevada: Geothermal Resources Council Transactions, v. 32, p. 147 – 151.

Gehrels, G.E., Dickinson, W.R., Darby, B.J., Harding, J.P., Manuszak, J.D., Riley, B.C., Spurlin, M.S., Finney, S.C., Girty, G.H., Harwood, D.S. and Miller, M.M., 2000, Tectonic implications of detrital zircon data from Paleozoic and Triassic strata in western Nevada and northern California: Geological Society of America Special Paper 347, p. 133-150.

Grant, S., Milton, N, and Thompson, M., 1996, "Play fairway analysis and risk mapping: An example using the middle Jurassic Brent group in the northern North Sea: Norwegian Petroleum Society Special Publications, v. 6, p. 167-181.

Hammond, W.C., Kreemer, C., and Blewitt, G., 2009, Geodetic constraints on contemporary deformation in the northern Walker Lane: Central Nevada seismic belt postseismic relaxation, in Oldow, J.S., and Cashman, P.H., eds., Late Cenozoic structure and evolution of the Great Basin – Sierra Nevada transition: Geological Society of America Special Paper 447, p.33-54, doi: 10.1130/2009.2447(03).

Henry, C.D., and Perkins, M.E., 2001, Sierra Nevada–Basin and Range transition near Reno, Nevada: Two-stage development at 12 and 3 Ma: Geology, v. 29, p. 719-722.

Hickman, S.H., and Davatzes, N.C., 2010, In-situ stress and fracture characterization for planning of an EGS stimulation in the Desert Peak Geothermal field, Nevada: Proceedings, Thirty-Fifth Workshop on Geothermal Reservoir Engineering Stanford University, Stanford, California, SGP-TR-188

Jolie, E., Moeck, I., and Faulds, J.E., 2015, Quantitative structural–geological exploration of fault-controlled geothermal systems—A case study from the Basin-and-Range Province, Nevada (USA): Geothermics, v. 54, p. 54–67, doi:10.1016/j.geothermics.2014.10.003.

Lautze, N., Thomas, D., Hinz, N., Apuzen-Ito, G., Frazer, N., and Waller, D., 2017, Play fairway analysis of geothermal resources across the State of Hawaii: 1. Geological, geophysical, and geochemical datasets: Geothermics, v. 70, p. 376-392.

Li, Y., and Oldenburg, D.W., 1998. 3-D inversion of gravity data: Geophysics, v. 63, p. 109–119.

Linde, G.M., Trexler, J.H., Cashman, P.H., Gehrels, G., and Dickinson, W.R., 2016, Detrital zircon U-Pb geochronology and Hf isotope geochemistry of the Roberts Mountains allochthon: New insights into the early Paleozoic tectonics of western North America: Geosphere, v. 12, no. 3, p. 1016-1031, doi:10.1130/GES01252.1.

Magoon, L. B., and Dow, W.G., 1994, The petroleum system, in Magoon, L. B. and Dow, W.G., eds., The petroleum system— From source to trap: American Association of Petroleum Geologists Memoir 60, p. 3 – 24.

Marrett, R., and Allmendinger, R.W., 1990, Kinematic analysis of fault-slip data: Journal of Structural Geology, v. 12, p. 973–986, doi:10.1016/0191-8141(90)90093-E.

McConville, E.G., Faulds, J.E., Hinz, N.H., Ramelli, A.R., Shevenell, L., Siler, D.L., and Bourdeau-Hernikl, J., 2017, A play fairway approach to geothermal exploration in Crescent Valley, Nevada: Geothermal Resource Council Transactions, v. 41, 9 p.

McConville, E.G., 2018, Detailed analysis of geothermal potential in Crescent Valley, north-central Nevada [M.S. thesis]: University of Nevada, Reno, 124 p.

Micklethwaite, S., and Cox, S.F., 2004, Fault-segment rupture, aftershock-zone fluid flow, and mineralization: Geology, v. 32, p. 813-816, doi:10.1130/G20559.1.

Moeck, I., Kwiatek, G., and Zimmermann, G., 2009, Slip tendency analysis, fault reactivation potential and induced seismicity in a deep geothermal reservoir: Journal of Structural Geology, v. 31, p. 1174–1182, doi:10.1016/j.jsg.2009.06.012.

Morris, A., Ferrill, D.A., and Henderson, D.B., 1996, Slip tendency analysis and fault reactivation: Geology, v. 24, no. 3, p. 275-278.

Nash, G.D., and Bennett, C.R., 2015, Adaptation of a petroleum exploration tool to geothermal exploration: Preliminary play fairway model of Tularosa Basin, New Mexico, and Texas: Geothermal Resources Council Transactions, v. 39, p. 743-749.

Ortner, H., Reiter, F., and Acs, P., 2002, Easy handling of tectonic data: The programs TectonicsVB for Mac and TectonicsFP for Windows: Computers and Geoscience, v. 28, p. 1193-1200.

Petit, J.P., 1987, Criteria for the sense of movement on fault surfaces in brittle rocks: Journal of Structural Geology, v. 9, p. 597–608, doi:10.1016/0191-8141(87)90145-3.

Rainbird, R.H., Hamilton, M.A., and Young, G.M., 2001, Detrital zircon geochronology and provenance of the Torridonian, NW Scotland: Journal of the Geological Society, v. 158, p. 15–27, doi:10.1144/jgs.158.1.15.

Romberg, F.E., 1958, Key variables of gravity: Geophysics, v. 23, no. 4, p. 684-700.

Shervais, J.W., Glen, J.M., Nielson, D., Garg, S., Dobson, P., Gasperikova, E., Sonnenthal, E., Visser, C., Liberty, L.M., Deangelo, J., Siler, D., and Evans, J.P., 2016, Geothermal play fairway analysis of the Snake River Plain: Phase 1, Proceedings, 41st Workshop on Geothermal Reservoir Engineering Stanford University, Stanford, California, SGP-TR-209.

Smith, C.M., 2021, Machine learning techniques applied to the Nevada geothermal play fairway analysis [M.S. Thesis]: University of Nevada, Reno, 130 p.

Smith, C.M., Faulds, J.E., Brown, S., Coolbaugh, M., Lindsey, C., Treitel, S., Ayling, B., Fehler, M., Gu, C., Mlawsky, E., 2021, Characterizing signatures of geothermal exploration data with machine learning techniques: An application to the Nevada play fairway analysis: Proceedings, 46th Workshop on Geothermal Reservoir Engineering, Stanford University, California, SGP-TR-218, 13 p.

Stewart, J.H., Gehrels, G.E., and Barth, A.P., 2001, Detrital zircon provenance of Mesoproterozoic to Cambrian arenites in the western United States and northwestern Mexico: Geological Society of America Bulletin, v. 113, no. 10, p. 1343-1356.

Stewart, J.H., and Perkins, M. E., 1999, Stratigraphy, tephrochronology, and structure of part of the Miocene Truckee Formation in the Trinity Range-Hot Springs Mountains area, Churchill County, west-central Nevada: USGS-open file report 99-330, 23 p.

Siler, D.L., Witter, J.B., Craig, J.W., Faulds, J.E., Glen, J.M., Earney, T.E., Schermerhorn, W.D., Peacock, J.R., Fournier, D., 2020, Using 3D gravity inversion modeling to iteratively refine 3D geologic maps: The Nevada play fairway project, southern Gabbs Valley, Nevada: Geothermal Resources Council Transactions, v. 44, 20 p.

Sladek, C., and Coolbaugh, M.F., 2013, Development of online map of 2 meter temperatures and methods for normalizing 2 meter temperature data for comparison analysis: Geothermal Resources Council Transactions, v. 37, p. 333-336.

Surpless, B.E., Stockli, D.F., Dumitru, T.A., and Miller, E.L., 2002, Two-phase westward encroachment of Basin and Range extension into the northern Sierra Nevada: Tectonics, v. 21, no. 1,1002, 13 p, doi: 10.1029/2000TC001257.

Thatcher, W., Foulger, G.R., Julian, B.R., Svarc, J., Quilty, E., and Bawden, G.W., 1999, Present day deformation across the Basin and Range province, western United States: Science, v. 283, p. 1714–1718.

Trexler, J.H., Cashman, P.H., Henry, C.D., Muntean, T., Schwartz, K., TenBrink, A., Faulds, J.E., Perkins, M., and Kelly, T., 2000, Neogene basins in western Nevada document the tectonic history of the Sierra Nevada–Basin and Range transition zone for the last 12 Ma, *in* GSA Field Guide 2: Great Basin and Sierra Nevada, Geological Society of America, v. 2, p. 97–116, doi:10.1130/0-8137-0002-7.97.

Trevor, M.S., and Wesnousky, S.G., 2001, The neotectonics character of the Granite Springs Valley and Bradys fault zones, western Basin and Range: Seismological Research Letters, v. 72, p. 256.

U.S. Geological Survey and California Geological Survey, 2010, Quaternary fault and fold database for the United States: http//earthquake.usgs.gov/hazards/qfaults/.

Vozoff, K., 1991, The Magnetotelluric method, in Nabighian, M.N., ed., Electromagnetic methods in applied geophysics: Society of Exploration Geophysics, p. 641–712, doi: http://dx.doi.org/10.1017/CBO9781139020138.

Wannamaker, P.E., Pankow, K.L., Moore, J.N., Nash, G.D., Maris ,V., Simmons, S.F., Hardwish, C.L., Trow, A., and Allis, R., 2017, Phase II activities in play fairway analysis for structurally controlled geothermal systems in the eastern Great Basin extensional regime, Utah: 42nd Workshop of Geothermal Reservoir Engineering, Stanford University, Stanford, California, SGP-TR-212, p. 1-12.

Wesnousky, S.G., Barron, A.D., Briggs, R.W., Caskey, S.J., Kumar, S., and Owen, L., 2005, Paleoseismic transect across the northern Great Basin: Journal of Geophysical Research, v. 110, p. 1–25, doi: 10.1029/2004JB003283.

Williams, C.F., Reed, M.J., Mariner, R.H., DeAngelo, J., and S.P. Galanis, 2008, Assessment of moderate- and high-temperature geothermal resources of the United States: U.S. Geological Survey Fact Sheet 2008-3082, 4 p.

Wisian, K.W., Blackwell, D.D., and Richards, M., 1999, Heat flow in the western United States and extensional geothermal systems: Proceedings, Twenty-Fourth Workshop on Geothermal Reservoir Engineering, Stanford University, Stanford, California, January 25-27, 8 p.

Witter, J.B., Glen, J.M.G., Siler, D.L., and Fournier, D., 2018, 2D and 3D potential field mapping and modelling at the Fallon FORGE site, Nevada, USA: Geothermal Resources Council Transactions, V.42, p. 1194–1214.

Witter, J.B., Siler, D.L., Faulds, J.E., and Hinz, N.H., 2016, 3D geophysical inversion modeling of gravity data to test the 3D geologic model of the Bradys geothermal area, Nevada, USA: Geothermal Energy, v. 4, p. 21, https://doi.org/10.1186/s40517-016-0056-6

Appendix A: Geochronological Data

Table A1. Igneous zircon age data.

	Apparent ages (Ma)						
Analysis	207Pb*	±	206Pb*	±	Best age	±	Conc
	235U	(Ma)	207Pb*	(Ma)	(Ma)	(Ma)	(%)
JD-01 - SPOT 1	101.3904091	1.56016514	108.238144	20.79159355	101.1001956	1.360472294	93.40533004
JD-01 - SPOT 2	103.3282667	1.40733596	84.36180624	18.604604	104.1514526	1.23864715	123.4580638

JD-01 - SPOT 3	101.4001139	1.584737428	93.53218637	20.76273114	101.7360789	1.40224168	108.7711972
JD-01 - SPOT 4	103.4292672	1.327189735	116.9837709	17.27899417	102.840925	1.15594767	87.91042055
JD-01 - SPOT 5	103.0111506	1.568120281	114.0915789	17.72138843	102.5319494	1.437690283	89.86811334
JD-01 - SPOT 6	94.0632748	1.591885656	121.1546102	27.16074367	92.9978581	1.242607828	76.75965279
JD-01 - SPOT 7	22.29847885	0.624088971	133.0659312	52.57840552	21.28421197	0.368439523	15.99523767
JD-01 - SPOT 8	102.6980945	1.156016075	91.78213972	13.05679536	103.1683977	1.071969084	112.4057448
JD-01 - SPOT 9	102.713635	1.407294089	90.50008065	16.43369958	103.2406979	1.293585246	114.0780176
JD-01 - SPOT 10	104.069025	1.311326662	112.6152034	17.9598965	103.6958182	1.117057004	92.07976823
JD-01 - SPOT 11	100.853172	1.407723442	101.6886465	21.82674672	100.8188199	1.139725006	99.14461783
JD-01 - SPOT 12	102.159075	1.55181391	139.6526408	22.40726966	100.5587564	1.276758036	72.00634072
JD-01 - SPOT 13	103.3060339	1.401583741	115.7004627	17.01653804	102.7704023	1.255209935	88.82453871
JD-01 - SPOT 14	101.6621006	1.332970157	116.7187505	19.49449881	101.0216669	1.104965396	86.55136081
JD-01 - SPOT 15	141.9031398	4.346548891	759.6407799	47.92424127	107.7352727	2.530321808	14.1823972
JD-01 - SPOT 16	101.1661441	1.421589532	100.3930407	15.41992495	101.1981596	1.329838992	100.8019668
JD-01 - SPOT 17	103.7755108	1.80871129	96.35757477	26.15387673	104.0991744	1.510718718	108.0342409
JD-01 - SPOT 18	102.3659482	1.038165203	105.7826016	13.68820528	102.2182921	0.907655726	96.63053335
JD-01 - SPOT 19	102.7300406	1.738949995	103.4955461	21.33185688	102.6969747	1.562997167	99.22840017
JD-01 - SPOT 20	106.6697439	1.727532921	180.3797695	21.22141049	103.3963092	1.479858745	57.32145546
JD-01 - SPOT 21	103.0701609	1.643261104	121.9119554	17.5646807	102.2568143	1.523407663	83.8775934
JD-01 - SPOT 22	103.3414345	1.389048629	97.15398917	16.81583755	103.6089247	1.256410479	106.6440252
JD-01 - SPOT 23	106.4847852	1.542218661	82.67890229	20.21443923	107.550791	1.34938517	130.0825096
JD-01 - SPOT 24	102.7371169	1.237664503	148.1025886	17.37906375	100.7918702	1.027193686	68.05544129
JD-01 - SPOT 25	105.0295843	1.473016177	128.068177	17.43336099	104.0177063	1.317830061	81.22057226
JD-01 - SPOT 26	106.3262303	1.851542201	105.7780365	25.65363493	106.3497023	1.560006579	100.540439
JD-01 - SPOT 27	102.8078484	1.320845228	78.68306303	13.80491244	103.8504767	1.256090094	131.9858083
JD-01 - SPOT 28	100.5023547	1.203105543	80.00507775	16.65789561	101.3675775	1.048979887	126.7014299
JD-01 - SPOT 29	100.0338492	1.2610125	121.4291434	15.78594309	99.13882453	1.123682936	81.64335329
JD-01 - SPOT 30	100.9945474	1.377337009	112.9443451	16.7574423	100.4898792	1.240708912	88.97291772
JD-01 - SPOT 31	135.0578465	4.589940451	653.6790249	72.48929396	107.4070787	1.417395688	16.43116493
JD-01 - SPOT 32	1187.728974	10.3185577	1213.013628	15.73800495	1213.013628	15.73800495	96.77541245
JD-01 - SPOT 33	108.6510826	2.46758291	253.6331442	45.29556061	102.1485566	1.380305035	40.27413565
JD-01 - SPOT 34	101.7972381	1.587023336	108.4424696	18.30559158	101.5130816	1.454242958	93.61007914
JD-01 - SPOT 35	102.4207768	1.360957157	116.0749176	17.8969579	101.8345985	1.184635691	87.73178618
JD-02 - SPOT 1	105.2190437	1.511835114	195.5491039	20.91969077	101.2726295	1.221766443	51.78884866
JD-02 - SPOT 2	101.0412512	1.224148622	113.2562257	17.59859925	100.5247891	1.029324032	88.75873128
JD-02 - SPOT 3	105.74113	1.465707667	214.5694867	19.68451578	100.9720622	1.188786224	47.05797818
JD-02 - SPOT 4	100.5007789	1.525480829	107.7444326	21.91735782	100.1965889	1.288666123	92.99467876
JD-02 - SPOT 5	101.8325272	1.504678249	70.50234262	19.17375755	103.1762455	1.358834624	146.3444215
JD-02 - SPOT 6	101.5755277	1.331561333	101.3177768	17.44422938	101.5855311	1.172641913	100.2642718
JD-02 - SPOT 7	104.7475114	1.73395847	192.5461606	24.11818748	100.9279489	1.402405237	52.41753384

JD-02 - SPOT 8	103.9583011	1.624676112	129.6197767	24.0542828	102.8410976	1.31422353	79.34059152
JD-02 - SPOT 9	101.6059271	1.524910771	141.1347752	13.67151328	99.9293858	1.453358284	70.80422642
JD-02 - SPOT 10	100.0153359	1.281355546	44.0964826	15.85203232	102.3756813	1.188933532	232.1629193
JD-02 - SPOT 11	103.0793808	1.47947367	130.2660791	16.03235658	101.9081292	1.36204866	78.23074888
JD-02 - SPOT 12	101.1136515	1.30956658	111.3964605	16.37380006	100.6782484	1.169821132	90.37831902
JD-02 - SPOT 13	101.9146094	1.236945675	102.7384362	18.02725975	101.8795635	1.033732098	99.16402005
JD-02 - SPOT 14	101.8406182	1.600591318	106.599477	21.09474953	101.6383772	1.401380773	95.3460374
JD-02 - SPOT 15	100.0823335	1.342639355	88.95045911	18.77618707	100.5512326	1.162482376	113.0418366
JD-02 - SPOT 16	104.1884597	1.615248128	111.8676363	17.70355634	103.8528464	1.492421826	92.83547037
JD-02 - SPOT 17	100.9986777	1.547827596	121.5131832	17.0861573	100.1305437	1.428314031	82.4030291
JD-02 - SPOT 18	101.2274532	1.563723892	92.26292626	18.83553893	101.6076652	1.426429015	110.1283791
JD-02 - SPOT 19	103.9545927	1.317634342	123.4565251	16.74284183	103.1047048	1.153554839	83.51499018
JD-02 - SPOT 20	102.5609093	1.417897502	126.5190888	18.79833816	101.533692	1.222762147	80.25167823
JD-02 - SPOT 21	104.0767009	1.428361307	128.2792565	18.7823672	103.0235473	1.229828012	80.31193047
JD-02 - SPOT 22	120.8949378	2.261827532	504.1615362	32.90336833	102.3027066	1.324370092	20.29165243
JD-02 - SPOT 23	100.3105662	1.445635864	94.53422142	17.54704628	100.5541885	1.31722226	106.3680295
JD-02 - SPOT 24	101.9468874	1.261722763	124.4271319	17.91042083	100.9868461	1.057366867	81.16143523
JD-02 - SPOT 25	107.4401012	1.660942497	182.7867164	24.38098525	104.0702397	1.289152298	56.93534067
JD-02 - SPOT 26	100.4773662	1.528040264	80.52117708	22.78940478	101.319491	1.283537599	125.8296199
JD-02 - SPOT 27	101.7516145	1.609044474	91.15112485	22.25754958	102.2049714	1.390067229	112.1269447
JD-02 - SPOT 28	109.6613965	1.784171053	290.5062504	27.19248677	101.5088509	1.245504775	34.94205402
JD-02 - SPOT 29	118.1526086	2.535549866	394.8664847	41.67135274	104.8589405	1.361917421	26.55554336
JD-02 - SPOT 30	102.5881034	1.453294081	141.7983539	19.76762328	100.9071269	1.229906184	71.16241064
JD-02 - SPOT 31	103.4915828	1.249056179	127.0634187	17.42995922	102.4716707	1.04804859	80.6460835
JD-02 - SPOT 32	101.1482922	1.698035796	135.5525957	26.42983497	99.69449526	1.344703311	73.54672534
JD-02 - SPOT 33	102.7160339	1.606729548	155.2190226	20.78566058	100.4669882	1.379594516	64.72595079
JD-02 - SPOT 34	111.7311622	2.158314501	321.5319209	25.40882748	102.1288265	1.728272622	31.7631998
JD-02 - SPOT 35	100.9744805	1.567644155	133.1953246	24.40960427	99.61535133	1.243751626	74.78892496

Table A2. Detrital zircon age data.

	Apparent ages (Ma)						
Analysis	207Pb*	±	206Pb*	±	Best age	±	Conc
TRMS-01	235U	(Ma)	207Pb*	(Ma)	(Ma)	(Ma)	(%)
Spot 1	110.3693062	1.825092383	197.7062827	38.00617281	106.3618632	0.640489483	53.79791766
Spot 2	108.3738163	2.330375355	95.24552948	47.00752689	108.9731145	1.183872754	114.4128393
Spot 3	107.5379443	2.105395801	84.4963288	35.44971799	108.5799152	1.532112588	128.502524
Spot 4	107.1217377	2.012192787	96.62179268	28.80870974	107.5934443	1.664583743	111.3552557
Spot 5	105.3158979	2.078485472	NA	NA	110.6118609	1.557416952	
Spot 6	104.8113965	1.767399816	51.9887538	34.50663981	107.1494215	1.095491365	206.1011539
Spot 7	110.2319626	4.209619084	20.25450166	NA	114.4409717	1.560181799	565.0149957

Spot 8	105.3212876	1.543641665	110.5189364	23.11441321	105.0913966	1.242307847	95.08904087
Spot 9	102.531278	1.770501601	36.89688562	32.82894552	105.3751787	1.242601031	285.5936942
Spot 10	105.4109842	2.003996747	63.53229829	38.39913597	107.273496	1.261585552	168.848757
Spot 11	101.5963509	1.496269553	56.42783557	22.19664466	103.5311475	1.269676706	183.4753123
Spot 12	104.8955333	2.028209263	7.554591392	NA	109.2287097	1.201002224	1445.858605
Spot 13	106.345492	2.06721761	54.15777606	39.0913163	108.6893689	1.324541484	200.6902365
Spot 14	107.942804	1.561965084	68.84314998	22.62450914	109.7216948	1.298347667	159.3792481
Spot 15	104.771715	1.732988036	84.90248773	26.43538028	105.6484474	1.401004599	124.4350433
Spot 16	106.8189723	1.57737051	86.51036948	22.99905256	107.7328214	1.300113996	124.5316857
Spot 17	104.4746858	1.755476287	14.7877425	NA	108.4484196	1.275678421	733.3669732
Spot 19	110.7278183	2.054055345	160.3096786	39.86598306	108.4348694	1.034980272	67.64087507
Spot 20	104.1931154	1.928400245	50.91030368	30.59869926	106.5370784	1.548659651	209.2642761
Spot 21	102.9423365	1.591243038	47.30803452	30.06079631	105.3611497	1.075343011	222.7130144
Spot 22	106.8690645	1.831170866	98.40256575	28.10019227	107.2491713	1.446929707	108.9902184
Spot 23	106.0581616	1.533896626	103.4863725	19.94901053	106.1729104	1.335221738	102.5960305
Spot 24	102.8727639	2.269191636	88.62710751	46.34690979	103.4896756	1.281496125	116.7697767
Spot 25	105.4447844	2.06297908	67.05251348	35.26199409	107.150441	1.52063537	159.8007821
Spot 26	116.6775849	3.633114843	33.7855087	NA	120.7802098	1.337435984	357.4911682
Spot 27	105.7929954	1.639853166	108.2938822	23.66206861	105.6820728	1.35120089	97.5882207
Spot 28	118.848808	3.920876004	357.1482569	71.76872717	107.2771545	1.547499047	30.03714912
Spot 29	103.148431	1.394378924	60.29450572	23.57605733	105.0127217	1.063500217	174.1663199
Spot 30	110.4261739	1.871477244	63.04503899	28.56154528	112.6342816	1.481942511	178.6568514
Spot 31	106.3998505	2.005550343	131.6611107	35.08351413	105.2757363	1.366851712	79.95962954
Spot 32	107.6621933	1.566674282	90.71122163	22.91574482	108.4298955	1.279805376	119.5330562
Spot 33	105.715177	1.5478099	66.00168806	25.46584412	107.4844946	1.183109873	162.8511297
Spot 34	107.9119043	1.693631809	84.59837167	23.5881332	108.9699153	1.42851471	128.8085257
Spot 36	104.8328089	2.090941065	57.51212145	44.14050502	106.9251063	1.049736459	185.9175137
Spot 37	104.9041741	1.607462935	44.67525178	22.86347312	107.5749942	1.385342038	240.7932578
Spot 38	106.8373367	1.846729992	116.2111192	31.39768653	106.4175261	1.310375701	91.57258511
Spot 39	105.5848132	2.371813437	50.23818934	50.11136681	108.0542038	1.169072197	215.0837943
Spot 40	109.2383808	1.914774587	112.0133625	28.72079766	109.1110238	1.506884168	97.40893529
Spot 41	103.5118262	1.802432377	49.53953148	32.5845977	105.871752	1.282954209	213.7116539
Spot 42	111.4260347	2.582313013	98.11653064	31.91725906	112.0490083	2.268023669	114.1999289
Spot 43	105.7708449	1.456025446	64.95733666	21.63803602	107.5904657	1.205136275	165.6325078
Spot 44	106.6187369	1.988308177	32.06461536	32.39657757	109.9843998	1.553722547	343.008636
Spot 45	103.2009652	1.725805923	53.83662982	24.54517742	105.3503232	1.490395609	195.685212
Spot 46	116.893585	1.946548641	79.74378392	31.7625395	118.7252489	1.351809	148.8833901
Spot 47	105.4942883	1.923927888	81.39725055	27.38400426	106.5632105	1.622050942	130.917457
Spot 48	105.593774	1.679535666	75.84198904	24.43798734	106.9158845	1.40194828	140.9718888
Spot 49	104.6505606	1.668754139	66.40817469	33.01706149	106.3375631	0.996410998	160.1272186

Spot 50	102.5156821	1.933478555	11.61592323	NA	106.4664007	1.536000451	916.55565
Spot 51	103.7321506	1.773392114	69.45155273	33.40228233	105.230579	1.173524911	151.5165246
Spot 52	112.7094715	2.327382756	57.48383934	43.98447195	115.3395404	1.331881081	200.6468979
Spot 53	103.530289	1.752104527	70.87658644	31.91042624	104.9536927	1.21732854	148.079497
Spot 54	106.6869637	1.722452979	114.339674	26.4629453	106.3452885	1.347997811	93.00821389
Spot 56	111.7389061	1.654794929	132.1139429	27.64773821	110.7858833	1.132162221	83.85631439
Spot 57	102.9128437	1.671910354	50.13951148	21.79336157	105.2053739	1.506812768	209.8252871
Spot 58	109.173134	1.694188423	114.7775123	22.78028799	108.9153693	1.42734546	94.89260313
Spot 59	102.8067964	2.055099046	41.65623037	42.19708039	105.4621825	1.193381315	253.1726504
Spot 60	106.8635133	1.500754585	105.9726054	23.48536097	106.9024414	1.162337837	100.8774305
Spot 61	107.8008645	2.942180804	38.23571488	NA	110.9732924	1.821273504	290.2346478
Spot 62	108.6904201	1.970145073	88.89404852	38.62408134	109.5969515	1.086338514	123.289414
Spot 63	114.530203	2.306257244	3.093147294	NA	119.9603426	1.50216772	3878.261563
Spot 64	119.7441416	5.61823473	353.1598724	108.2922001	108.317176	1.435214209	30.67086167
Spot 65	107.7833959	2.017501689	44.75424161	34.42541954	110.6550659	1.478612302	247.2504549
Spot 66	107.6993921	1.821199927	83.12242217	32.2731896	108.8127697	1.243096127	130.9066397
Spot 67	106.3815868	1.958752365	74.39116266	32.9997848	107.8145391	1.447849158	144.9292299
Spot 68	109.3071034	1.56680343	119.4504532	22.48849209	108.842124	1.265862086	91.11905489
Spot 69	148.1714651	6.934278453	681.7851372	102.520759	116.9828391	1.74743864	17.15831465
Spot 70	107.1002136	1.966954833	27.73302195	NA	110.7021023	1.619940541	399.170716
Spot 71	101.2413408	1.907160133	NA	NA	106.2458295	1.495076243	
Spot 72	105.1737995	1.454379993	62.05717313	24.110405	107.0856669	1.112231435	172.5596921
Spot 73	104.4498023	2.060560173	38.26103827	30.04337562	107.3721714	1.760633725	280.6305743
Spot 74	103.5792052	1.907076757	70.63926888	23.97274857	105.0165355	1.722782535	148.6659434
Spot 75	104.284354	1.695500092	80.74962726	24.28929515	105.316173	1.431900598	130.4231073
Spot 76	109.2869239	1.635487762	130.1681144	27.16234316	108.331136	1.156449255	83.22401878
Spot 77	139.6302935	1.980845179	678.8719074	24.85915163	109.9756778	1.064123344	16.19976855
Spot 78	103.467598	1.708798661	85.47181017	22.60791831	104.2516034	1.501653615	121.9719148
Spot 79	111.1894669	1.725314564	125.5013785	31.0897525	110.5211489	1.061490367	88.06369317
Spot 80	101.5471974	2.930402433	NA	NA	106.2753259	1.173395877	
Spot 81	109.607644	2.186794086	122.970488	41.6634534	108.9924782	1.233009998	88.63303709
Spot 82	109.3823295	1.839786356	133.9869376	30.26857265	108.255854	1.309506046	80.79582677
Spot 83	163.5074742	9.871897967	916.1211641	130.9857708	116.3394643	1.739462649	12.6991351
Spot 84	106.1164264	1.960388483	126.8915775	30.71043902	105.1942271	1.506240236	82.90087429
Spot 85	103.9879827	1.495121531	2.48869338	NA	108.4679886	1.10287385	4358.431193
Spot 86	106.2756496	1.758588495	74.25014036	26.13983697	107.7089268	1.44374425	145.0622535
Spot 87	104.164698	1.664433766	52.09316251	31.11333714	106.4554396	1.121107014	204.3558779
Spot 88	107.0288701	1.837686905	48.79361339	27.66493027	109.6618046	1.510410626	224.7462261
Spot 89	108.300803	1.512218759	178.4196984	19.81339244	105.1373342	1.252936736	58.92697674
Spot 90	105.2926853	2.14146588	27.35972848	NA	108.7685202	1.624696706	397.5497062

Spot 91	108.0766656	1.687451793	115.878435	25.46907757	107.722956	1.326883273	92.96203903
Spot 92	103.9796622	1.774245283	67.94779956	30.2214622	105.5594556	1.329011513	155.3537514
Spot 93	103.992994	1.932828895	48.58280023	33.74402737	106.4275434	1.426515053	219.0642426
Spot 94	192.1456618	15.69503569	1291.453047	172.3429792	114.9847652	1.694788443	8.903518825
Spot 95	103.2572087	1.482573489	100.5079086	23.77072829	103.3758234	1.155833777	102.853422
Spot 96	105.1803691	1.879460244	36.17137113	28.0162062	108.2498253	1.581529276	299.2693446
Spot 97	111.940247	1.452962325	199.1444057	26.39051778	107.8824306	0.821761721	54.1729657
Spot 98	105.132309	1.997899822	75.48009641	40.81573683	106.4441918	1.082761394	141.0228615
Spot 99	108.0872163	1.747529137	95.7812508	25.43880794	108.6468877	1.425415149	113.4323125
Spot 100	99.71594579	1.895696737	20.84567057	NA	103.0435596	1.620932432	494.3163582
Spot 101	103.3874048	1.614569987	3.595244382	NA	107.7659024	1.292537663	2997.456943
Spot 103	110.3125223	1.73243216	182.2437781	29.21819242	107.0069668	1.149545815	58.71638962
Spot 104	100.5042847	2.073532667	NA	NA	105.0665208	1.270085244	
Spot 105	101.8377171	2.538379729	41.81696011	NA	104.4194761	1.139646668	249.7060423
Spot 106	106.1692816	1.601144252	78.21969061	22.60946166	107.4178747	1.354922447	137.3284321
Spot 107	106.467445	1.47912809	66.18203152	20.13034736	108.2751381	1.282655348	163.6020164
Spot 108	106.0669192	1.538706035	65.98117684	24.27599644	107.8598142	1.216895885	163.4705826
Spot 109	102.315321	1.919703516	32.07275322	NA	105.3551384	1.070615511	328.4879776
Spot 110	107.8996806	1.689131846	95.77645137	30.30228199	108.4502044	1.120856475	113.2326401
Spot 111	101.0264403	2.029506734	NA	NA	106.439715	1.244416909	
Spot 112	106.058365	2.09353301	82.19571398	33.48098347	107.122592	1.623027028	130.3262504
Spot 113	113.4174988	2.026336147	140.586007	36.27158768	112.1281486	1.205677018	79.75768781
Spot 114	106.5754465	1.751238016	90.305664	27.17472088	107.3054268	1.379984589	118.8246916
Spot 115	104.3771898	1.547453578	10.13822049	NA	108.5498316	1.07339869	1070.699061
Spot 116	121.6984761	2.203681426	359.1371682	33.09571495	109.887496	1.3515277	30.59763949
Spot 117	108.429041	2.391674855	118.690715	45.85259131	107.962586	1.36393147	90.96127364
Spot 118	106.9389503	1.686697707	77.47159506	28.15281743	108.2652257	1.249576132	139.7482853
Spot 119	101.2433516	1.673391797	11.14264461	NA	105.1089069	1.299169861	943.3030546
Spot 120	107.1418597	1.807049256	6.781861592	NA	111.7075547	1.510903279	1647.151792
Spot 121	112.4536318	1.956045552	176.2406979	31.98291496	109.4618294	1.327656754	62.10928048
Spot 122	107.104583	1.878368642	95.69278962	31.0035556	107.6176001	1.392230185	112.4615559
Spot 123	106.4555367	1.866630889	63.67173527	29.98846237	108.3772057	1.452791842	170.2124267
Spot 124	107.7344769	1.773359834	66.3986868	27.41443716	109.6128865	1.410188418	165.0829132
Spot 125	105.6600608	2.514199011	NA	NA	111.9956066	1.605258008	
Spot 126	118.5453496	2.729826865	369.0042094	42.83926949	106.4329796	1.612580869	28.84329689
Spot 127	111.1366356	1.718386288	58.93484012	25.74871316	113.5889162	1.378008509	192.7364459
Spot 128	112.9714708	2.685540706	222.4292783	51.64789607	107.8427249	1.230388994	48.48405109
Spot 129	103.6837661	2.061108092	12.59929009	NA	107.6870303	1.314354338	854.707127
Spot 130	107.2433283	1.04434247	111.7317367	15.4976887	107.0415919	0.837856899	95.80231636
Spot 131	102.4073243	1.820095435	NA	NA	106.9457499	1.345395861	

Spot 132	105.6643215	6.809518042	120.2556087	NA	105.0174149	1.792022864	87.32849636
Spot 133	103.2913775	1.925975335	1.752078494	NA	107.7443201	1.484250733	6149.514445
Spot 134	263.4253871	6.935165051	1900.305552	49.94752803	117.9742216	1.28797151	6.208171179
Spot 135	110.5632183	1.611928823	116.9848554	25.02726006	110.264211	1.217473805	94.25511587
Spot 136	103.1033779	2.844725435	7.970727643	NA	107.262857	1.64242151	1345.709725
Spot 137	108.3129499	1.635895536	168.1439657	23.939284	105.6099129	1.277427807	62.80921974
Spot 138	100.915511	1.839904678	10.0901086	NA	104.8013537	1.366288908	1038.654368
Spot 139	106.8739077	1.800038419	85.97541984	28.76881718	107.8147762	1.384737316	125.4018607
Spot 140	183.8841974	2.732992768	105.4032738	31.8793915	190.0466446	1.695073501	180.304309
Spot 141	106.5453374	1.824311599	76.78936495	32.13216126	107.8796765	1.2762776	140.4877831
Spot 142	106.4060871	1.390147204	108.557134	21.43549937	106.3100051	1.089729231	97.9300035
Spot 143	104.9033049	1.572628178	80.17304223	21.53398821	105.9942216	1.35707368	132.2068099
Spot 144	159.7229662	2.053506181	149.2327071	19.56963467	160.4309414	1.759005892	107.503874
Spot 145	2713.073674	11.22393859	2714.103069	9.87882242	2714.103069	9.87882242	99.91054163
Spot 146	108.1559439	1.634383828	128.3392003	24.7397979	107.2426129	1.272933216	83.56185223
Spot 147	105.9269555	1.724100837	84.17374551	28.67448034	106.8955898	1.288887589	126.9939804
Spot 148	107.5510115	1.61798289	115.128739	21.62822224	107.2101804	1.375244919	93.12199664
Spot 150	126.9872249	3.116697405	442.3951409	52.47664348	110.7662638	1.228628974	25.03785724
Spot 151	106.9967877	2.946386084	30.70904007	NA	110.4532706	1.101397837	359.6767282
Spot 152	105.5837322	2.076638872	34.27686894	NA	108.7699439	1.480500112	317.3275369
Spot 153	110.4165787	2.002664325	223.7333835	35.14940911	105.2304218	1.214228586	47.03384901
Spot 154	113.0490941	2.001095512	235.3583484	31.69407522	107.3245026	1.351368104	45.60046555
Spot 155	116.9139943	3.06713958	85.30543792	60.18825738	118.4738162	1.327451418	138.8819038
Spot 156	100.9316269	2.123848009	NA	NA	106.7674466	0.987013196	
Spot 157	106.0182479	2.059120021	101.5117046	31.41800727	106.2199326	1.6385328	104.6381134
Spot 158	105.664588	1.544331458	118.7705936	21.75249092	105.0831704	1.284424905	88.47574742
Spot 159	105.8466857	1.542905273	125.0850296	19.90748699	104.9928294	1.334199735	83.93716631
Spot 160	107.0863383	2.093001089	125.0869308	30.31430069	106.2777692	1.693915844	84.96312804
Spot 161	104.7066871	1.971996504	21.35058431	NA	108.4056845	1.534366486	507.7410668
Spot 162	105.7670098	1.95766139	22.03524551	NA	109.5196738	1.119622388	497.0204382
Spot 163	100.2927592	1.422155679	37.75460457	20.80623474	102.9416653	1.235487602	272.6598953
Spot 164	112.2126846	1.892568756	82.91001001	33.15381606	113.5973655	1.243917873	137.0128474
Spot 165	104.9886144	3.277752303	NA	NA	110.2092233	1.190864418	
Spot 166	106.6470822	1.613804196	100.2216737	22.95386487	106.9348611	1.341265371	106.6983389
Spot 167	109.1262745	1.656121305	116.6553577	21.48580007	108.7806242	1.418988348	93.24957409
Spot 168	108.9894352	2.188889207	151.4664165	45.1979908	107.0557572	0.927766537	70.67953392
Spot 169	106.0674337	1.805380603	104.1282416	24.12994174	106.1532182	1.552037145	101.9446949
Spot 170	110.6508766	2.682483902	129.0909422	51.37658562	109.7968122	1.452398916	85.05384675
Spot 171	113.6224356	1.920872172	120.2009837	32.39050809	113.3085189	1.281799174	94.26588319
Spot 172	101.3081911	1.359037562	NA	NA	107.1234399	1.043642298	

Spot 173	104.0035698	1.61781699	29.18685764	29.79705576	107.2967601	1.132808083	367.6201166
Spot 174	114.4307353	1.936852572	186.3537865	33.58010635	111.0006985	1.166139627	59.56449856
Spot 175	105.807166	2.083601552	59.9876916	38.43220618	107.8521194	1.394594169	179.7904145
Spot 176	107.9342973	1.687156767	84.39902201	23.68977058	109.0026544	1.416643628	129.151561
Spot 177	107.6135583	2.258088955	114.232253	42.90774083	107.3143722	1.338642444	93.9440214
Spot 178	98.1808044	1.599060735	NA	NA	105.6836421	0.928888572	
Spot 179	106.5124903	1.603056408	78.72006634	25.11834897	107.7580789	1.262543254	136.8876882
Spot 180	102.616124	2.253897462	-0.550235088	NA	107.1114789	1.433962086	-19466.49372
Spot 181	101.6287471	1.818093629	32.35860852	26.97200175	104.6066	1.562400366	323.2728624
Spot 182	107.0698999	1.828571641	78.47989306	23.24579039	108.3581673	1.622812322	138.0712474
Spot 183	104.2277061	2.734086928	NA	NA	117.0858538	1.576365384	
Spot 184	104.4955782	1.520035725	72.85997446	25.9538742	105.8890519	1.127756881	145.332266
Spot 185	113.750705	1.963414222	67.52095065	39.83847237	115.9727618	0.834630296	171.7581887
Spot 186	111.1874241	3.139404727	NA	NA	117.9925229	1.600420252	
Spot 187	96.97482091	2.009481936	NA	NA	104.2280354	1.279827663	
Spot 188	100.9686824	2.149796409	NA	NA	109.5936588	1.004916976	
Spot 189	110.3494054	1.82350646	86.24972334	31.37174461	111.4704157	1.256264637	129.2414763
Spot 190	113.0607942	2.111710582	229.5920238	38.76013822	107.600313	1.107153911	46.86587591
Spot 191	107.69723	1.684265977	74.26072213	27.98122953	109.213838	1.249124262	147.0681066
Spot 192	106.0062603	1.986787528	117.1211709	38.53005341	105.5112902	1.160084922	90.08729107
Spot 193	104.8079415	1.942910445	38.01004529	38.98656466	107.7676633	1.146081678	283.5241644
Spot 194	106.1740974	1.809150566	69.70209024	33.80016299	107.8074343	1.173456261	154.6688685
Spot 195	104.7831643	2.027390046	55.33962377	31.77438082	106.9697764	1.634626161	193.2968986
Spot 196	109.1915673	1.830424515	86.55327159	23.05585416	110.2332851	1.613527607	127.358889
Spot 197	99.80878259	7.2318901	NA	NA	108.4319642	1.028444571	
Spot 198	107.9078811	1.661812634	75.31446541	23.73950885	109.3889908	1.388053435	145.2430024
Spot 199	192.9866929	3.026989937	332.0637721	20.63260492	181.8023168	2.621114018	54.74921747
Spot 200	105.0084766	1.703329672	15.8041906	NA	108.9806204	1.183937144	689.5678692
Spot 201	112.7801583	4.598256306	130.0181221	44.52281397	111.9650205	4.294849889	86.11493437
Spot 202	109.1739854	1.962432616	124.8317717	33.83689424	108.4564811	1.330773135	86.88211308
Spot 203	104.3759263	2.181460897	32.87732449	NA	107.533079	1.49008975	327.0736918
Spot 204	106.0708384	1.610165969	59.81495849	22.70650152	108.140219	1.376726742	180.7912632
Spot 205	105.1190876	1.569164043	23.99316307	NA	108.7312611	1.202264767	453.1760183
Spot 206	105.4924437	1.940923839	79.79912467	27.86553841	106.6324566	1.630456711	133.626098
Spot 207	105.1238879	1.468842312	100.119022	17.02138042	105.3441723	1.340359358	105.2189386
Spot 208	143.9170258	5.696135416	721.9693193	85.67673934	111.3094583	1.447457205	15.41747762
Spot 209	106.3714641	1.897619085	88.79505604	25.8147862	107.1589162	1.627347426	120.6811742
Spot 210	113.6083485	1.463981968	88.42861627	15.97292235	114.8146833	1.346913446	129.8388329
Spot 211	140.1583723	7.357992598	680.7001303	115.9169282	110.323553	1.612588613	16.20736476
Spot 212	97.86978414	3.825577	NA	NA	107.9227851	1.289645592	

Spot 213	101.0315456	1.975960057	38.99850256	33.11262875	103.6804876	1.562199324	265.8576119
Spot 214	105.6457776	1.71821363	85.3501812	27.51075928	106.5488703	1.332332116	124.83731
Spot 215	101.6647478	2.408190276	NA	NA	108.3865794	1.403410868	
Spot 216	105.9380801	1.566173926	94.43415898	22.05571281	106.4498177	1.317131644	112.7238479
Spot 217	104.8633717	1.750806156	11.60904118	NA	109.0116927	1.477404914	939.024085
Spot 218	102.5411257	1.489726763	24.30905812	23.82621529	105.9362754	1.220248842	435.7893048
Spot 219	108.0589664	1.701412235	131.2965594	27.40833646	107.006926	1.254959081	81.50017521
Spot 220	141.1921614	2.059715785	232.9744204	22.97603916	135.7916931	1.619238577	58.28609544
Spot 221	108.7407826	1.74204111	88.77219889	23.2965122	109.6556298	1.494371002	123.5247422
Spot 222	115.7452199	4.151498921	219.436473	84.65673151	110.7637137	1.114467195	50.47643727
Spot 223	105.3246025	1.797792343	67.48012923	32.28930368	107.005911	1.251507586	158.5739568
Spot 225	108.7242473	1.376956391	181.022636	22.65830984	105.450418	0.957543013	58.25261432
Spot 226	104.7059948	1.56762946	32.2531191	25.48814672	107.9157552	1.243097306	334.5901365
Spot 227	106.4975985	1.796386764	4.591358421	NA	111.1060877	1.094977357	2419.895758
Spot 228	104.7375616	1.790259327	92.48322733	25.41155679	105.2775906	1.50843533	113.8342526
Spot 229	106.9072121	1.591924326	109.580574	21.57222615	106.7872823	1.350368264	97.45092433
Spot 230	103.4943691	1.837545748	18.3443459	NA	107.2294399	1.591351471	584.5367314
Spot 231	104.9750082	1.689787264	37.14580889	25.90756523	107.9856536	1.395630505	290.7075034
Spot 232	123.7201621	3.891436282	451.1193315	70.46034906	107.3459657	1.115982915	23.79547011
Spot 233	438.6791952	4.997233854	422.5610261	21.32383962	441.7524005	4.385919574	104.5416811
Spot 234	105.6527738	1.457373391	46.37808082	26.25926664	108.2998478	1.021042725	233.515156
Spot 235	112.9124661	3.582051268	203.8514924	71.04511513	108.6436843	1.471547597	53.29550596
Spot 236	117.819296	2.613251896	330.3543232	46.38994093	107.5586815	1.232731311	32.55858148
Spot 237	106.8318256	1.659573728	74.87739226	30.96425714	108.270964	1.063510608	144.5976692
Spot 238	106.5724744	1.959833163	18.20698243	NA	110.5666257	1.509095629	607.2759509
Spot 239	106.0109375	1.481126485	46.89235234	25.39112201	108.6599543	1.096515809	231.7221228
Spot 240	110.7522956	1.578425656	96.20211218	23.55320084	111.4305138	1.246033181	115.8295918
Spot 241	110.2420447	2.036897137	84.78895793	32.30063591	111.4228327	1.541681286	131.4119614
Spot 242	106.8858581	1.611931851	104.9866226	23.45262208	106.9700777	1.317188367	101.8892455
Spot 243	109.4573848	1.593580317	107.6935634	26.06359697	109.5395379	1.160747111	101.7140992
Spot 244	109.3546415	1.714245978	94.68321721	31.74299905	110.0300323	1.057582913	116.2085907
Spot 245	106.8766033	1.788815115	91.98015939	31.86983151	107.5450922	1.215288174	116.9220546
Spot 246	114.8925626	2.205380961	239.2792638	32.14987523	108.9752577	1.594228373	45.54312648
Spot 247	105.9007396	1.730264562	97.84383187	26.11953545	106.2602075	1.390162961	108.6018459
Spot 248	109.6389014	2.015728607	119.9173332	36.76564111	109.1672245	1.249089388	91.03540046
Spot 249	106.4791148	1.753900213	91.94031763	25.77552946	107.1303341	1.435644957	116.5216054
Spot 250	111.9287552	1.791885166	125.7276741	27.12058573	111.2799762	1.365583661	88.50873688
Spot 251	107.9639156	1.924466828	76.75937374	35.54761963	109.3823688	1.231569494	142.5003403
Spot 252	106.5330716	1.829239004	124.0574715	34.18708285	105.7499441	1.131636227	85.24270468
Spot 253	109.5813909	1.921974776	79.21731672	26.65100912	110.9824272	1.617938453	140.0986953

Spot 254	106.2381544	2.034058604	71.03186117	38.71811288	107.8142532	1.272192246	151.7829484
Spot 255	112.0957783	1.422633061	197.2242816	19.59166611	108.1262888	1.117648817	54.82402464
Spot 256	112.1196256	1.829408308	194.4896368	28.87343466	108.2785794	1.283285476	55.67318711
Spot 257	106.3536728	1.619437719	120.4227984	21.16465573	105.7259815	1.392952714	87.79565243
Spot 258	107.3778896	1.678383805	99.46914593	25.44414017	107.7353927	1.332555804	108.3103626
Spot 259	111.6756192	2.016196848	114.2474391	38.10776797	111.5541616	1.121055494	97.64259274
Spot 260	107.1297446	2.019217982	85.74398513	31.64485777	108.0949743	1.577313961	126.067122
Spot 261	103.8468792	1.991120232	NA	NA	108.666222	1.318204433	
Spot 262	104.0347977	3.804561526	NA	NA	109.7672798	1.272295609	
Spot 263	1652.013221	10.18791837	1725.17948	12.82253284	1725.17948	12.82253284	92.45899074
Spot 264	106.3748685	3.103711331	47.16372346	NA	109.0376613	1.683999293	231.18968
Spot 265	102.2654623	2.658958888	NA	NA	113.9598719	1.355125414	
Spot 266	106.3026822	1.925855335	86.38727514	38.27154734	107.1944068	1.081926119	124.0858757
Spot 267	102.0657588	1.976605338	18.30731483	NA	105.6879197	1.152217553	577.2988595
Spot 268	112.4716536	1.739806179	177.4498713	24.2304027	109.4239252	1.368202499	61.66469689
Spot 269	110.8792022	1.925191641	163.6148595	27.57705597	108.4374438	1.509281118	66.27603639
Spot 272	104.9594884	2.283079191	52.53197125	45.4561205	107.2830697	1.352358649	204.2243364
Spot 273	95.22365725	1.664813403	NA	NA	105.5426196	1.414565924	
Spot 274	111.8022256	1.84599513	167.3855956	33.76552392	109.2078557	1.056771617	65.24328176
Spot 275	101.9651411	1.951924682	NA	NA	109.7046122	1.109055794	
Spot 276	111.0529968	2.240310348	208.4079173	38.13565345	106.5644757	1.431255659	51.13264267
Spot 277	110.618239	1.916004871	122.0103765	36.05531339	110.0906345	1.090250796	90.23055061
Spot 278	160.746227	11.07331431	953.9481931	150.135438	112.1626027	1.459810006	11.75772474
Spot 279	103.7234025	2.467567886	NA	NA	109.2187696	1.423616879	
Spot 280	104.2995535	2.341367411	NA	NA	112.8570747	1.214227227	
Spot 281	107.0583226	1.807785388	120.5847029	26.39725039	106.4505216	1.458784355	88.27862827
Spot 282	101.5652063	3.370520832	NA	NA	110.4543652	1.431955763	
Spot 283	106.5761804	1.619865914	119.0158909	27.00979518	106.0214287	1.176444988	89.08174189
Spot 284	111.7201888	2.476651643	16.83994493	NA	116.219494	1.012020788	690.1417702
Spot 285	123.7110232	4.474067441	320.8206591	83.88007147	113.6943957	1.199442392	35.43861423
Spot 286	106.4772239	1.697197659	33.15768237	30.60080585	109.7827542	1.185830641	331.0929664
Spot 287	107.7415725	2.109875302	83.85103651	39.50447799	108.8241494	1.315349592	129.7827122
Spot 288	105.8053076	1.639506916	75.07851088	24.45911124	107.1757397	1.345802959	142.7515523
Spot 289	109.6758201	1.756172115	120.0635002	26.06245878	109.1982123	1.3826995	90.95038217
Spot 290	112.84538	4.071419505	197.2007735	84.97962194	108.8859127	1.165867575	55.21576349
Spot 291	108.5678601	1.470672107	88.92390962	27.50995345	109.4664131	0.902313411	123.101215
Spot 292	104.8217613	1.640875599	88.84206778	26.59211385	105.5270449	1.263976507	118.7804916
Spot 294	103.7256731	2.70470526	NA	NA	108.9634525	1.223973903	
Spot 295	107.2702307	1.971046199	NA	NA	112.6590135	1.06487749	
Spot 296	2686.189309	10.58219459	2722.680584	9.719698046	2722.680584	9.719698046	96.88818099

Spot 297	106.2315001	1.644398799	95.6947042	25.18320478	106.7011073	1.306933592	111.5015802
Spot 298	127.9519612	4.944979523	486.8379222	85.70285143	109.4562195	1.477376338	22.48309232
Spot 299	95.03480352	4.986379933	NA	NA	105.1348449	1.42078935	
Spot 300	118.9444684	2.173271511	281.813996	37.8194014	110.9576371	1.110372489	39.37264957
Spot 301	101.8803534	4.520392411	NA	NA	109.173064	1.145805922	
Spot 302	104.2701686	2.799807351	17.8549199	NA	108.0878988	1.935734678	605.3675929
Spot 303	104.5436683	1.425832763	72.1117426	19.60890939	105.9719209	1.234739632	146.955152
Spot 304	104.1799128	1.687488225	70.79928367	27.49302733	105.6450525	1.312107305	149.2176856
Spot 305	99.7930288	2.026922073	NA	NA	105.4851614	1.524507256	
Spot 306	108.0212071	1.802887937	121.8085947	32.91897653	107.3968098	1.138745559	88.16849918
Spot 307	103.008406	2.195610174	30.29035902	NA	106.1773601	1.537436196	350.5318641
Spot 308	107.2215575	1.754527265	64.087635	34.05928856	109.1716825	1.042854669	170.3474976
Spot 309	105.6403318	1.901401242	82.85904558	32.60084462	106.6520882	1.380965814	128.7150817
Spot 310	102.8563217	2.224266055	10.67100922	NA	106.8760608	1.121521172	1001.555323
Spot 311	106.5198878	1.786785807	15.36365108	NA	110.6384739	1.340358091	720.1313889
Spot 312	107.5353492	2.106221657	63.81708716	34.11118337	109.5198771	1.615119232	171.6152868
Spot 313	107.0574508	1.854697918	107.2070245	26.6399505	107.0517273	1.524734554	99.85514272
Spot 314	111.1407689	1.476945004	93.02952924	24.20882652	111.9872573	1.066794036	120.3781834
Spot 315	110.0856996	1.74900281	97.725449	31.61940088	110.6589773	1.111093028	113.234555
TRMS-02							
xx	1131.701155	10.07987632	1120.844713	13.3801358	1120.844713	13.3801358	101.4745602
Spot 1	247.6441895	2.140994883	265.1794079	14.96314437	245.7975389	1.747981361	92.69103539
Spot 2	1570.503479	11.66481035	1608.902679	11.82217297	1608.902679	11.82217297	95.84644021
Spot 3	101.9484707	2.478576257	52.84131319	51.77543504	104.0618069	1.39271569	196.9326661
Spot 4	2678.060298	10.50142839	2682.247736	8.960107986	2682.247736	8.960107986	99.63671234
Spot 5	171.742352	2.484793091	267.7477829	27.23884809	164.8493568	1.677261286	61.56889706
Spot 6	170.7954133	2.24213229	187.7561402	26.03481166	169.5717976	1.48126528	90.31491456
Spot 7	173.2004667	3.196844568	223.1246229	30.88567369	169.5654135	2.507167525	75.99583196
Spot 8	2684.800873	8.797092376	2668.633807	6.864428328	2668.633807	6.864428328	101.4117458
Spot 10	2657.325929	8.202221371	2678.56865	6.849554222	2678.56865	6.849554222	98.16795266
xx	442.1824699	4.753869042	417.7303262	17.49990478	446.8907594	4.619502967	106.9806838
Spot 11	2832.034032	7.089116115	2793.057579	5.811851645	2793.057579	5.811851645	103.3669978
Spot 12	2712.614929	10.28386265	2701.079993	9.739540338	2701.079993	9.739540338	101.0007113
Spot 13	2640.396243	7.572970717	2626.72665	5.030568824	2626.72665	5.030568824	101.2002369
Spot 14	184.781804	2.640860458	323.619538	32.05241617	174.0990358	1.157336873	53.7974428
Spot 15	105.7623759	1.669373443	83.18101202	24.76463708	106.7664201	1.369585583	128.3543173
Spot 16	2674.689613	10.47312311	2664.583057	7.692931206	2664.583057	7.692931206	100.8811367
Spot 17	105.4091876	1.466193404	77.98657111	29.54325179	106.6252197	0.817452625	136.7225385
Spot 18	1681.7024	7.09814049	1738.23223	7.384144522	1738.23223	7.384144522	94.16144968
Spot 19	435.7596966	3.884233427	508.3199177	19.54987992	422.1535061	2.626349203	83.04878314

Spot 20	167.9461708	2.518634524	127.2129141	23.13495278	170.8522966	2.185531777	134.3042079
Spot 21	238.5174253	2.567669101	234.8294913	21.18575655	238.8943806	1.840858897	101.7309961
Spot 22	2635.5727	9.125887215	2641.157615	9.701477106	2641.157615	9.701477106	99.51289845
Spot 23	109.9028175	1.833086004	55.61759913	26.13839852	112.4243542	1.53380228	202.138093
Spot 24	110.9632706	1.613331518	75.47411137	31.67901791	112.6227881	0.850329223	149.2204228
Spot 25	1424.435755	11.31751074	1433.914953	12.83201536	1433.914953	12.83201536	98.89633364
Spot 26	153.2732387	3.491883735	NA	NA	170.7990955	1.742282261	
Spot 27	349.4083523	7.868939786	749.8684324	37.81343039	292.1656189	5.624299772	38.96225074
Spot 28	2686.58016	10.53665593	2695.255367	9.735542891	2695.255367	9.735542891	99.25018459
Spot 29	2719.093164	11.60703963	2684.796016	11.93992452	2684.796016	11.93992452	103.0053843
Spot 30	2665.080052	7.269398267	2659.169856	7.078417908	2659.169856	7.078417908	100.5147154
Spot 31	2636.580157	10.10537209	2617.456586	8.916980207	2617.456586	8.916980207	101.6845613
Spot 32	1409.613837	9.283281544	1422.670621	15.55424297	1422.670621	15.55424297	98.4753635
Spot 33	2690.013222	11.10930399	2675.325536	12.10987919	2675.325536	12.10987919	101.2806805
Spot 34	2709.679833	9.803214968	2695.09562	9.07651119	2695.09562	9.07651119	101.2677031
Spot 35	106.593725	2.236933957	96.36294234	48.00549522	107.0522124	0.93340171	111.0927186
Spot 36	2651.739924	11.48877761	2652.308366	11.08471748	2652.308366	11.08471748	99.94974726
Spot 37	2688.149071	11.75312194	2688.35258	13.03079929	2688.35258	13.03079929	99.98155034
Spot 39	2693.928332	11.37718312	2686.182265	11.9872057	2686.182265	11.9872057	100.6726666
Spot 40	2687.898724	9.658362609	2684.018315	7.545406937	2684.018315	7.545406937	100.3364137
Spot 41	2703.163471	8.500009166	2693.358986	6.828953619	2693.358986	6.828953619	100.8509241
Spot 42	176.5355871	2.70610448	275.3274418	33.06396543	169.2434413	1.406136183	61.46987754
Spot 43	2686.29047	10.33654315	2674.395916	10.43581009	2674.395916	10.43581009	101.0362626
Spot 44	106.6279563	2.111069413	76.81002994	45.8563138	107.9661899	0.846377112	140.5626192
Spot 45	1007.981512	6.820807092	1011.812159	12.25543319	1011.812159	12.25543319	99.44642794
Spot 46	112.207765	2.082756324	148.4331266	34.81856908	110.508428	1.401837101	74.44997657
Spot 47	2659.564632	9.438600991	2648.765903	8.247506851	2648.765903	8.247506851	100.9438514
Spot 48	2675.308703	10.29490135	2678.473583	10.92165885	2678.473583	10.92165885	99.72503479
Spot 49	168.5749832	3.464307091	208.8782196	44.04460809	165.7185308	1.912336839	79.33739145
Spot 50	34.09370069	1.268883403	NA	NA	34.98974781	0.538904126	
Spot 51	2716.919413	10.29757392	2693.560675	9.880300713	2693.560675	9.880300713	102.0368582
Spot 52	160.6934997	3.466378283	149.8146552	44.77879727	161.4325477	2.135195898	107.7548438
Spot 53	112.2788177	2.260799333	37.70131726	34.59063457	115.8249212	1.791823653	307.2171733
Spot 54	1329.375402	15.44656065	1405.172079	22.72597015	1405.172079	22.72597015	91.29276203
Spot 55	228.0293809	3.218335286	272.7118172	28.42965799	223.717316	2.137910859	82.03433143
Spot 56	2703.538587	6.988988489	2673.347048	4.778360079	2673.347048	4.778360079	102.6466343
Spot 57	103.0752692	2.251006352	19.75434804	NA	106.7138598	1.336048035	540.2044126
Spot 58	2689.551797	7.076754539	2661.913929	5.49144341	2661.913929	5.49144341	102.4248803
Spot 59	168.8481574	3.475193138	158.980446	39.16942837	169.5545655	2.47615165	106.6512075
Spot 60	2676.121124	12.43216971	2680.414404	12.92492179	2680.414404	12.92492179	99.62744349

xx	397.2931901	5.853070443	340.6248236	33.03577105	407.1042842	4.024249022	119.516916
Spot 61	2702.938415	10.34808089	2687.869509	7.210667872	2687.869509	7.210667872	101.311723
Spot 62	175.5842075	4.648447724	69.76308196	60.80809544	183.5364542	2.412934592	263.0853584
Spot 63	172.8684662	5.110005696	297.186928	69.52677472	163.9161875	1.660228132	55.15592109
Spot 64	163.4256452	2.731194189	235.1418375	36.20392863	158.5185414	1.410651813	67.41400984
xx	1070.465342	8.001404282	1095.778804	12.93357439	1095.778804	12.93357439	96.55899303
Spot 66	2601.860675	8.217177918	2585.759145	6.239786614	2585.759145	6.239786614	101.4239814
Spot 67	2704.073555	11.88215356	2701.930609	10.3820997	2701.930609	10.3820997	100.184778
Spot 68	2718.788839	7.088372909	2669.165239	5.044688225	2669.165239	5.044688225	104.3795188
Spot 69	182.1844034	3.225997763	332.0666385	34.5429719	170.8331667	2.009286097	51.44544707
Spot 70	349.9697981	6.535534756	532.5481506	30.72990505	323.0727075	5.370705736	60.6654454
Spot 71	117.4165434	2.578485151	231.573159	45.67382912	111.8570606	1.357719498	48.30311988
Spot 72	224.209734	4.610734502	839.9894895	42.83256339	169.9813035	1.69528427	20.23612268
Spot 75	253.4976678	7.513213689	1149.155322	62.35375628	167.588965	1.92975297	14.58366522
Spot 76	2668.026229	9.300291932	2666.768153	8.305162625	2666.768153	8.305162625	100.1088026
Spot 77	165.163913	2.31705312	190.7905495	27.72685507	163.3828409	1.523828153	85.63466132
Spot 78	175.6987766	3.054382957	108.5336998	34.66665189	180.7297856	2.131081864	166.5195105
Spot 79	2692.381433	7.185811146	2656.766155	6.798007418	2656.766155	6.798007418	103.1351625
Spot 80	170.0973572	1.63915666	184.6148063	19.04201185	169.0538075	1.090099212	91.57109921
Spot 81	2703.884624	39.31917269	2652.238242	42.72970688	2652.238242	42.72970688	104.5725207
Spot 82	169.347059	2.337875634	107.7989175	28.74157805	173.7818978	1.500630435	161.2093162
Spot 83	2632.421119	13.8985966	2598.426067	13.97421332	2598.426067	13.97421332	103.0178414
Spot 84	178.032489	2.306522463	276.3987497	23.37271734	170.7118656	1.646010453	61.76289357
Spot 85	1330.627053	13.08872879	1409.131288	24.23729959	1409.131288	24.23729959	91.00492417
Spot 86	172.6474899	1.90507901	194.1356911	20.43398364	171.084584	1.379735961	88.12629094
Spot 87	165.0796672	2.7046255	64.63849821	28.85293572	172.1658448	2.205503239	266.3518639
Spot 88	175.0229031	10.05387135	1162.193863	114.2771562	110.9317055	2.67403229	9.545025922
Spot 89	118.403698	2.225145357	255.0248639	39.85406515	111.712598	1.083912039	43.80459077
Spot 90	122.1013914	2.177414736	131.6654874	38.98117543	121.6116764	1.099355286	92.3641258
Spot 91	106.0311397	1.962075762	74.95833202	39.87618904	107.4179826	1.057806363	143.3035925
Spot 92	1619.510735	6.887974392	1639.222683	10.16474237	1639.222683	10.16474237	97.87404856
Spot 93	177.6683941	2.824690001	302.4807948	33.33038792	168.4248524	1.547939181	55.68117225
Spot 94	178.8793619	2.458910459	323.8326214	27.81932849	168.0991982	1.434826669	51.90928493
Spot 95	1304.584231	10.07166872	1378.800501	15.70191801	1378.800501	15.70191801	91.37736744
Spot 96	931.6373317	8.495713149	1006.4612	13.96073741	1006.4612	13.96073741	89.45404666
Spot 97	2697.903593	7.679305799	2674.630905	6.801905067	2674.630905	6.801905067	102.0352147
Spot 98	2696.767636	8.629482622	2699.251804	7.855511222	2699.251804	7.855511222	99.78449554
Spot 99	161.3933357	2.599880023	80.68850747	27.04625339	166.9431705	2.171881692	206.8983251
Spot 100	1185.482107	9.930006296	1185.93368	17.34275485	1185.93368	17.34275485	99.94185471
Spot 101	2729.538859	8.253093232	2680.275222	8.07171735	2680.275222	8.07171735	104.3400764

Spot 102	979.8190099	7.218047835	1031.542416	10.4055329	1031.542416	10.4055329	92.7632122
Spot 103	109.5107659	2.864120326	84.87929513	59.91547675	110.6477478	1.217676685	130.3589381
Spot 104	2632.428742	9.272431845	2630.124567	6.567630948	2630.124567	6.567630948	100.2010162
Spot 105	183.1692777	2.639820917	345.9566406	29.83961835	170.79235	1.450760423	49.36813749
Spot 106	175.8011874	3.934516153	256.3560253	52.01758301	169.8689964	1.518724072	66.26292329
Spot 107	118.3934044	2.063412004	296.5405172	27.92629555	109.7122071	1.50489632	36.99737496
Spot 108	171.0186035	2.267479851	234.6188581	26.38546171	166.4568796	1.439222824	70.94778355
Spot 109	188.948727	6.772749226	424.1751173	85.08101018	170.6528771	1.596632855	40.23170387
Spot 110	123.4103644	1.653510762	167.7366648	20.72511433	121.1205245	1.334848508	72.2087354
Spot 111	115.9240382	1.958535712	100.7808254	29.7440391	116.6625455	1.46889353	115.7586725
Spot 112	2799.511252	8.87577621	2844.389659	6.898828846	2844.389659	6.898828846	96.24656719
Spot 113	170.6131472	2.330050573	190.5837886	23.59852269	169.1779056	1.809269344	88.76825612
Spot 115	184.0203253	2.613038827	207.5181346	29.11750867	182.1950885	1.640933295	87.79718884
Spot 116	2682.21767	9.704624776	2709.150382	11.27472151	2709.150382	11.27472151	97.6917173
Spot 117	1574.955875	11.88574036	1765.33887	9.692778919	1765.33887	9.692778919	81.38788728
Spot 119	112.7340094	1.887941163	198.9356098	30.0783292	108.691884	1.29959486	54.63671593
Spot 120	171.6778617	2.937166658	184.0176159	39.31653471	170.7820252	1.314879119	92.80743278
Spot 121	173.7732522	2.574032267	216.1914483	27.52645976	170.6712232	1.83385534	78.94448399
Spot 122	179.8828628	4.362364553	287.2687696	57.1575252	171.811675	1.470754845	59.80868551
Spot 123	2679.470627	10.72656501	2675.945433	9.560202323	2675.945433	9.560202323	100.3058536
Spot 124	2674.974733	10.13342762	2687.040131	9.893876731	2687.040131	9.893876731	98.95756182
Spot 125	2706.756091	7.252127137	2684.214933	6.635052563	2684.214933	6.635052563	101.968024
Spot 126	179.0424035	2.714337302	277.0112451	31.652374	171.7089776	1.539536287	61.98628419
Spot 127	205.8667287	4.1491246	559.3764972	44.55386929	176.3111531	1.537700037	31.51922792
Spot 128	109.1604145	2.04914491	162.2599913	31.35087503	106.7409702	1.542612207	65.78391221
Spot 129	2653.067006	7.642251343	2647.463163	7.344640967	2647.463163	7.344640967	100.488721
Spot 130	2679.147968	8.94309126	2677.131631	8.98758807	2677.131631	8.98758807	100.1745957
Spot 131	172.2903222	2.969071554	217.1927252	30.52182098	169.0361076	2.221989807	77.8277023
Spot 132	162.673416	2.006218625	153.087753	15.11544199	163.3342315	1.884335302	106.6932059
Spot 133	118.8724482	2.003557963	91.77769307	34.03366063	120.2298687	1.265807808	131.0011885
Spot 134	112.2794061	1.929134257	147.525562	31.52895477	110.6242593	1.336824801	74.98650252
Spot 135	2723.769627	15.22545924	2728.070084	22.29051642	2728.070084	22.29051642	99.62942042
Spot 136	2667.132335	10.73849937	2665.755343	8.44653892	2665.755343	8.44653892	100.1191611
Spot 137	2711.811157	10.65539444	2695.083502	10.19642474	2695.083502	10.19642474	101.4551002
Spot 138	2709.271664	9.597966776	2681.772082	9.364440073	2681.772082	9.364440073	102.40561
Spot 140	2688.790932	10.97904135	2681.997532	12.16363442	2681.997532	12.16363442	100.5900411
Spot 141	2696.354558	11.59069671	2684.800342	10.74698543	2684.800342	10.74698543	101.0049996
Spot 142	2700.496285	11.58578461	2690.634262	8.761370312	2690.634262	8.761370312	100.8562578
Spot 143	2700.025622	7.325896081	2670.738053	7.42465669	2670.738053	7.42465669	102.5676375
Spot 144	2701.534573	10.30691728	2681.059101	9.414711822	2681.059101	9.414711822	101.7872968

Spot 145	111.0806753	1.704996682	133.2927588	32.15924474	110.0464969	0.947785069	82.55999639
Spot 146	612.5693671	5.62131505	635.0908237	13.62312816	606.5009789	6.051585652	95.49830611
Spot 147	174.3837115	3.30603915	51.65734959	39.62829022	183.5615398	2.217599628	355.3444791
Spot 148	104.18202	1.756276065	99.85346898	32.32833058	104.3723667	1.170293578	104.525529
Spot 149	2667.458529	7.888930833	2651.820675	6.63366231	2651.820675	6.63366231	101.3686158
Spot 150	2686.807699	9.624181333	2705.52234	9.062356346	2705.52234	9.062356346	98.39086808
Spot 151	683.1509676	12.52516513	1997.820547	32.39276018	355.3112349	6.008931082	17.78494246
Spot 152	2708.918303	7.810798487	2658.479285	7.160435092	2658.479285	7.160435092	104.4597483
Spot 154	119.5818149	1.672969368	247.0905132	30.80635015	113.2664843	0.719036013	45.84007812
Spot 155	2687.652199	11.27469476	2691.393745	11.25759864	2691.393745	11.25759864	99.67546883
Spot 156	2688.148889	7.544280205	2692.515335	7.278439089	2692.515335	7.278439089	99.62154355
Spot 158	99.45546551	1.636586943	138.6725146	33.16622028	97.82592901	0.966044651	70.54456991
Spot 159	2680.702212	6.68709458	2625.627637	5.81828922	2625.627637	5.81828922	104.9014225
Spot 160	2489.905961	11.75931742	2614.641797	13.23839115	2614.641797	13.23839115	89.4924047
Spot 161	177.1231632	3.102150669	285.4252651	35.3590031	169.1119357	1.869744853	59.24911224
Spot 162	2683.565741	7.428737812	2632.525618	6.650400461	2632.525618	6.650400461	104.5318314
Spot 163	161.3744821	3.553530055	134.1474572	45.74141566	163.2356875	2.211359893	121.6837731
Spot 164	2657.262662	10.29101793	2637.008517	9.586899714	2637.008517	9.586899714	101.779612
Spot 165	173.5048574	2.646814664	269.5860356	31.32056774	166.534486	1.551349332	61.77415149
Spot 166	187.4084882	3.772360897	332.3669051	46.51556561	176.1025614	1.401211796	52.98438523
Spot 167	168.0985811	1.610298233	184.6642798	19.15896716	166.9225439	1.046849546	90.39243761
Spot 168	2654.059374	8.011589628	2668.927968	7.353312408	2668.927968	7.353312408	98.71306264
Spot 169	2693.167904	9.729293849	2662.68652	8.191634238	2662.68652	8.191634238	102.6764961
Spot 170	109.8482682	2.171117685	27.52444966	NA	113.6825765	1.312252667	413.0239766
Spot 172	167.2469258	2.209140087	197.5281899	27.59783336	165.1136178	1.305690384	83.5899007
Spot 173	166.9580138	2.217607458	144.1088336	27.7598987	168.5725388	1.365454581	116.975854
Spot 174	180.5242721	2.570251892	227.0794703	28.01200211	176.9892756	1.696706225	77.94155736
Spot 175	114.7946229	2.650447888	109.8803272	47.39705339	115.0325091	1.585167702	104.6889029
Spot 176	170.7517438	3.693058698	141.8024563	37.04670674	172.8467246	2.96901111	121.8926167
Spot 177	2687.345593	8.86523117	2678.213124	8.74649301	2678.213124	8.74649301	100.794383
Spot 178	184.0772321	4.87894027	418.5908275	59.27864868	166.3141412	1.911403998	39.73191248
Spot 179	2723.132421	7.571172702	2667.044196	6.17175719	2667.044196	6.17175719	104.961645
Spot 180	2705.973463	7.845409954	2680.578278	6.788411293	2680.578278	6.788411293	102.2204156
Spot 181	413.8018816	3.949426301	492.5770002	15.34806937	399.8112883	3.608872166	81.16726687
Spot 182	121.3683062	2.255067931	134.9042663	40.97216767	120.6780111	1.099316829	89.45455498
Spot 183	2657.514723	10.53018832	2640.480953	8.742583756	2640.480953	8.742583756	101.4942948
Spot 184	2711.556045	8.848045073	2681.155564	7.920092011	2681.155564	7.920092011	102.6620701
Spot 185	678.7398358	7.66909736	695.8521272	27.12136726	673.5986164	5.641609383	96.80197704
Spot 186	166.53527	2.331636052	178.7509508	25.74458913	165.6754116	1.704448875	92.68505195
Spot 187	111.7678974	1.718116869	158.4567945	32.75984293	109.5869322	0.893064729	69.15887235

Spot 188	2685.126594	5.928277376	2674.859944	4.794875695	2674.859944	4.794875695	100.8938473
Spot 189	2733.426069	7.098671377	2679.297041	6.741464469	2679.297041	6.741464469	104.776654
Spot 190	2691.820001	9.638981187	2653.749011	6.741907108	2653.749011	6.741907108	103.3554579
Spot 191	168.1746237	3.165318885	164.600109	41.72475525	168.4270979	1.650743868	102.3250221
Spot 192	125.7464235	1.969656087	242.095063	33.68718036	119.6745411	0.944716149	49.43287136
Spot 193	2712.237921	8.02189641	2688.299038	7.283550087	2688.299038	7.283550087	102.0894217
Spot 194	173.0353064	3.183460366	290.0896057	40.67849043	164.5884287	1.484618632	56.73709966
Spot 195	2726.249854	11.02083209	2699.054677	11.48515168	2699.054677	11.48515168	102.3724646
Spot 196	2694.444689	11.29774647	2699.315332	8.917415496	2699.315332	8.917415496	99.57847496
Spot 197	112.3730285	1.630458169	119.2499807	25.76309828	112.0497203	1.192446941	93.96204481
Spot 198	2669.107212	13.08633171	2695.390535	13.47161847	2695.390535	13.47161847	97.74229447
Spot 199	2690.929425	10.55414317	2678.118478	10.05553615	2678.118478	10.05553615	101.1158681
Spot 200	2676.044755	10.82022147	2675.184149	10.08859825	2675.184149	10.08859825	100.0741849
Spot 202	170.6647094	2.895207474	195.5180768	36.6659232	168.8786198	1.586504457	86.37493909
Spot 204	2661.620748	9.610745664	2670.116389	7.557163851	2670.116389	7.557163851	99.26307743
Spot 205	2740.375804	10.85581388	2684.382755	10.63477112	2684.382755	10.63477112	104.9402771
Spot 206	120.3972827	1.697586006	148.4915026	29.02576996	118.9787348	0.986920303	80.12494498
Spot 207	2682.531872	7.681474676	2631.08497	5.476373679	2631.08497	5.476373679	104.5695382
Spot 208	936.0238247	9.053603569	1550.812893	15.94256595	1550.812893	15.94256595	44.94601116
Spot 209	160.014121	2.293568353	176.1812731	28.68273473	158.922463	1.47935842	90.20394741
Spot 210	115.6465383	2.066676041	320.2805727	38.24080759	105.9424213	0.903960454	33.07800421
Spot 211	109.7308459	1.266787544	116.7272637	19.0048106	109.4091725	0.990225089	93.73060675
Spot 212	255.3635558	3.552333575	313.798322	33.13671506	249.0432617	1.451408168	79.36411516
Spot 213	2681.542815	12.93100233	2697.101024	11.64454837	2697.101024	11.64454837	98.65912834
Spot 214	133.7574001	2.672584673	308.6209945	42.35711785	124.1136476	1.281294788	40.21555558
Spot 215	259.6176482	2.749929178	403.8030311	20.18257079	243.9214513	1.897692424	60.40604764
Spot 216	206.7003822	2.676826822	187.4260863	22.57590413	208.3925902	2.158754836	111.1865452
Spot 217	2730.151375	6.99102082	2686.68806	6.569436856	2686.68806	6.569436856	103.8185089
Spot 218	193.8079067	3.310236141	379.8912923	38.34985217	178.8633953	1.378252	47.08278365
Spot 221	2691.697587	9.105550399	2690.765395	7.379746944	2690.765395	7.379746944	100.079993
Spot 222	2717.268228	8.198340572	2688.535092	7.202372873	2688.535092	7.202372873	102.5116868
Spot 223	2674.461012	8.873903218	2678.415387	8.587388875	2678.415387	8.587388875	99.65666065
Spot 224	2696.988434	9.559135754	2673.15083	9.896725433	2673.15083	9.896725433	102.085449
Spot 226	2723.673323	8.30595631	2679.401963	6.877887186	2679.401963	6.877887186	103.8946795
Spot 228	2677.352367	10.55622933	2669.241221	9.130031708	2669.241221	9.130031708	100.7061416
Spot 229	327.8366474	3.344297305	341.8888785	14.41225832	325.8624475	3.207995677	95.31238597
Spot 230	2656.83383	11.71614516	2654.247424	10.60695327	2654.247424	10.60695327	100.2247612
Spot 231	2675.919594	11.79058892	2684.369685	10.69125159	2684.369685	10.69125159	99.26864589
Spot 232	2696.435003	6.611338544	2680.569254	6.39950197	2680.569254	6.39950197	101.382908
Spot 233	170.2018425	2.946315431	206.0718847	31.51383784	167.6336536	2.151876478	81.3471735

Spot 234	2637.934924	8.670408673	2626.567356	7.298537849	2626.567356	7.298537849	100.9973133
Spot 235	2695.033659	8.973003852	2685.430387	8.959078622	2685.430387	8.959078622	100.8346368
Spot 236	2682.773863	8.108294866	2673.190262	9.108749051	2673.190262	9.108749051	100.8343597
Spot 237	2691.165044	11.47999719	2698.213595	8.705242802	2698.213595	8.705242802	99.3906178
Spot 240	166.5186035	2.671894483	232.7368249	32.85539654	161.8975785	1.60171419	69.56251059
Spot 241	112.6801163	2.228231342	178.0387562	45.51415152	109.6089	0.808514663	61.56462913
Spot 242	2674.892165	8.019756097	2648.874536	8.202784583	2648.874536	8.202784583	102.285929
Spot 243	2693.281625	11.19922466	2685.837466	11.86994719	2685.837466	11.86994719	100.6463997
Spot 244	113.2368077	1.327385662	173.12467	23.83718201	110.4066917	0.767762391	63.77293986
Spot 245	1163.657657	6.286692503	1151.478257	10.62153888	1151.478257	10.62153888	101.6260068
Spot 246	2678.235025	6.53934949	2661.537303	7.476412542	2661.537303	7.476412542	101.4598466
Spot 247	114.0053473	1.707137067	266.7999393	29.62397049	106.8184493	0.970206139	40.03690916
Spot 248	168.8720078	1.695220016	197.9817197	17.92969071	166.8016818	1.268185658	84.25105213
Spot 249	128.7229756	2.916475307	323.4955551	49.4394927	118.413587	1.220260374	36.60439383
Spot 250	2681.897671	8.327200539	2671.030994	6.331256236	2671.030994	6.331256236	100.9468126
Spot 251	391.7413852	7.80189043	703.0306113	38.06765363	341.0641644	5.31866536	48.51341591
Spot 252	2662.662281	12.89521136	2661.811226	9.966667832	2661.811226	9.966667832	100.0734103
Spot 253	151.8496515	8.510889816	726.4779456	123.2806934	117.6076157	1.903754366	16.18873861
Spot 254	2666.818468	9.736853872	2668.752617	8.584175502	2668.752617	8.584175502	99.83137836
Spot 255	159.9048057	2.835323083	61.89423419	35.42861693	166.5955472	1.988163261	269.1616585
Spot 256	1119.084026	8.311122818	1135.187999	16.13635095	1135.187999	16.13635095	97.85321439
Spot 259	2679.146058	8.941107517	2669.028801	8.387689397	2669.028801	8.387689397	100.8815184
Spot 260	179.2720551	2.523663778	325.9352933	20.36985682	168.3398229	2.070645906	51.64823397
Spot 261	627.0479906	5.809443121	637.7879191	22.76754075	624.080068	3.869106308	97.85071954
Spot 262	2674.2802	10.52009971	2674.785156	9.889295661	2674.785156	9.889295661	99.95558694
Spot 263	175.4376389	2.177011027	236.4958165	23.77702214	170.9400531	1.475821731	72.28037082
Spot 265	2645.155994	6.678194654	2617.713577	5.956914017	2617.713577	5.956914017	102.4238631
Spot 266	167.7278444	2.703020479	136.3590052	33.86106848	169.9575587	1.65982158	124.6397761
Spot 267	2709.744109	9.994966094	2695.144072	9.608665733	2695.144072	9.608665733	101.269077
Spot 268	108.3659783	2.33372212	66.90461646	48.21341204	110.2603233	1.121679453	164.8022649
Spot 269	180.0983746	4.077994903	331.0627047	51.34243092	168.8004162	1.648048939	50.98744552
Spot 270	2674.292205	7.006883845	2655.902215	5.796939227	2655.902215	5.796939227	101.6100366
Spot 271	109.9387982	1.770861923	104.9556252	25.248805	110.1679445	1.44432121	104.9662125
Spot 272	106.943965	1.524906942	115.9986328	25.44420753	106.5381513	1.10401761	91.84431639
Spot 273	169.1244944	3.211976852	254.6909391	33.20327748	163.0685408	2.368819758	64.02604716
Spot 274	2687.356255	6.561865422	2658.813584	5.191939585	2658.813584	5.191939585	102.5061411
Spot 275	114.1115235	1.639526705	75.38127903	26.96263669	115.9754097	1.16120282	153.8517404
Spot 276	2657.152282	12.07280055	2668.176436	9.910262882	2668.176436	9.910262882	99.04439716
Spot 277	2702.459791	7.818329947	2675.347333	6.935141547	2675.347333	6.935141547	102.3736857
Spot 278	178.9353667	2.118169813	228.3495122	22.25782012	175.217828	1.485628618	76.73229789

Spot 279	2555.796189	11.95316971	2553.261936	10.58914995	2553.261936	10.58914995	100.2235856
Spot 281	234.7237354	2.206982958	217.536622	18.21542461	236.4417645	1.623860941	108.6905563
Spot 282	1649.363555	10.62977574	1608.916985	13.66393878	1608.916985	13.66393878	104.4977846
Spot 283	2709.861597	13.16834705	2690.705551	11.06759125	2690.705551	11.06759125	101.6687487
Spot 284	1314.523181	9.827969703	1354.24671	15.96697827	1354.24671	15.96697827	95.27738805
Spot 285	108.8395475	1.432741673	95.25004904	20.54100694	109.4626227	1.176391124	114.9213295
Spot 286	1218.23462	9.365799882	1193.180736	15.21361217	1193.180736	15.21361217	103.2884511
Spot 287	243.1362037	3.207501847	234.5279029	19.98236179	244.030822	2.88547066	104.0519354
Spot 288	124.4823896	1.962455448	274.8269729	34.29934687	116.7482231	0.871119659	42.48062766
Spot 289	2701.350379	10.73814528	2678.641907	6.440004327	2678.641907	6.440004327	101.9843491
Spot 290	149.1961404	3.031844969	NA	NA	160.7382203	1.725966472	
Spot 291	2704.391323	10.57525799	2661.620291	8.983419672	2661.620291	8.983419672	103.7708762
Spot 292	116.3111556	2.985871917	125.9301248	59.36326876	115.8426232	1.162376885	91.98960405
Spot 293	2668.168941	7.021058925	2646.230438	5.400282247	2646.230438	5.400282247	101.9257093
Spot 294	2678.444543	6.796449848	2673.711059	6.763891043	2673.711059	6.763891043	100.4111574
Spot 295	2650.146511	8.236899941	2647.434148	9.552812693	2647.434148	9.552812693	100.2359382
Spot 296	2729.771413	7.829001459	2675.721862	7.47206342	2675.721862	7.47206342	104.7720638
Spot 297	2684.149824	7.26525326	2672.435838	6.823103079	2672.435838	6.823103079	101.0207504
Spot 298	176.0857849	2.279271038	221.0548619	25.93147062	172.7528007	1.455549164	78.14928801
Spot 299	172.5661726	1.834659724	213.3547724	15.86543333	169.6062165	1.558631976	79.4949251
Spot 300	104.2194163	2.655554177	NA	NA	109.3285002	1.565819011	
Spot 301	110.3074377	1.292453099	119.8804324	20.52131044	109.8645518	0.956291546	91.6451081
Spot 303	117.71612	2.967586191	284.4357432	57.77096794	109.6295944	0.939366674	38.54283331
Spot 304	2700.122016	8.799164406	2685.463012	9.162641405	2685.463012	9.162641405	101.2763062
Spot 306	234.3492498	2.683146597	189.4283433	18.31704113	238.8502994	2.372960223	126.0900535
Spot 307	2718.350602	11.23396257	2699.111763	10.51850765	2699.111763	10.51850765	101.6740021
Spot 309	2685.048908	10.03011723	2657.527476	9.597566825	2657.527476	9.597566825	102.4161381
Spot 310	2683.744293	9.271223853	2683.488843	9.892210375	2683.488843	9.892210375	100.0216416
Spot 311	2730.071194	8.61907666	2704.099201	7.906145758	2704.099201	7.906145758	102.2632227
Spot 312	1118.319949	7.091759668	1144.329444	15.13966992	1144.329444	15.13966992	96.56125626
Spot 313	156.0639412	4.45561415	0.861469402	NA	166.4694404	1.907591231	19323.89474
Spot 315	2494.281726	35.39887388	2638.96657	37.84833692	2638.96657	37.84833692	87.93283582
TRMS-03							
Spot 2	102.1812441	1.467455438	33.47276371	28.95200354	105.149723	0.943611725	314.1351695
Spot 3	103.3745095	2.203489638	NA	NA	111.0960605	1.055737837	
Spot 4	2714.381919	6.163522499	2714.262641	6.278912174	2714.262641	6.278912174	100.0096924
Spot 5	119.1629766	3.601721361	312.2406614	69.57786519	109.7096424	1.038199023	35.13624457
Spot 6	299.3285202	23.7090311	1960.50407	162.501356	131.8991732	1.339538391	6.727819401
Spot 7	108.5591041	1.437323008	31.12512839	24.8744321	112.1187806	1.03818102	360.219496
Spot 8	102.0280206	1.296726607	63.13792694	21.17276725	103.6992487	1.025550895	164.2424035

Spot 9	121.4551521	5.751497575	328.9437274	111.1720279	111.117592	1.231952967	33.78012188

Appendix B: Fault Kinematic Data

Table B1. Fault Kinematic Data compiled for the northern Hot Springs Mountains. Sense of movement is as follows: 0 = unknown, 1 = reverse, 2 = normal, 3 = dextral, 4 = sinistral. Data acquired primarily by J. Faulds from 2002 to 2012.

Station	Strike (azimuth)	Dip Direction (azimuth)	Dip angle (°)	Trend (azimuth)	Plunge (°)	Sense of Movement
F02-038	207	297	60	297	60	2
F02-039	41	131	57	131	57	2
F02-574	47	137	84	226	13	4
F02-574	290	20	37	291	1	4
F03-049	198	288	75	322	72	2
F03-049	235	325	59	325	59	2
F03-052	213	303	58	285	57	2
F03-064	53	143	70	143	70	2
F03-095	10	100	86	180	68	2
F03-109	232	322	56	285	50	2
F03-120	203	293	54	293	54	2
F03-122	202	292	58	290	58	2
F04-061	21	111	54	119	54	2
F04-078	324	54	78	54	78	2
Garside	225	315	40	303	39	2
Garside	195	285	49	320	43	2
Garside	27	117	80	117	80	2
F05-035	20	110	58	134	56	2
F05-035	20	110	58	31	43	4
F05-047	23	113	60	132	59	2
F05-102	17	107	85	107	85	2
F05-127	11	101	74	122	72	2
F05-127	355	85	78	173	17	3
F05-127	71	161	87	250	10	4
F05-180	6	96	80	100	80	2
F06-346	10	100	67	100	67	2
F08-546	218	308	73	308	73	2

F09-204	164	254	70	254	70	2
F09-238	52	142	69	154	68	2
F09-240	29	119	71	177	57	2
F09-301	48	138	65	90	54	2
F09-400	324	54	80	126	62	2
F09-416	40	130	77	166	74	2
F09-423	46	136	48	155	46	2
F09-436	347	77	82	153	60	2
F09-436	3	93	74	122	72	2
F09-436	14	104	55	144	48	2
F12-09	12	102	68	146	61	2
F12-12	52	142	60	146	60	2
F12-13	9	99	51	122	49	2
F12-131	13	103	77	251	66	2
F12-136	3	93	78	93	78	2
F12-136	16	106	73	106	73	2
F12-140	2	92	50	115	48	2
F12-151	55	145	35	144	35	2
F12-152	52	142	67	185	60	2
F12-180	39	129	55	138	55	2
F12-186	33	123	33	123	33	2
F12-212	14	104	60	123	59	2
F12-238	25	115	38	115	38	2
F12-243	208	298	46	305	46	2

Appendix C: 2 m Temperature Data

Table C1. 2 m Temperature Data. Data acquired by M. Coolbaugh in 2007

NAME	EAST	NORTH	TEMP_C	AVE_TEMP	AVE_GRAD	HEAT_FLUX	DAB
Q201	338239.8	4399867	23.1	16.9	0.6656	410.6752	0.85
Q202	338227.5	4399272.5	22.2	16	0.3552	219.1584	-0.05
Q203	338617.7	4399631.7	21.8	15.6	0.2172	134.0124	-0.45
Q204	338168	4398549.1	20.3	14.1	-0.3001	-185.1617	-1.95
Q1	340809	4408243	23.1	16.9	0.6656	410.6752	0.85
Q2	341737.9	4406564	30.5	24.3	3.2179	1985.4443	8.25

Q3	341261.1	4405488	28.7	22.5	2.597	1602.349	6.45
Q4	340754.1	4405530.1	29.2	23	2.7695	1708.7815	6.95
Q5	338570	4404914.1	24.3	18.1	1.0795	666.0515	2.05
Q6	340791.1	4409847.9	21.9	15.7	0.2517	155.2989	-0.35
Q7	339852	4405635.1	23.9	17.7	0.9415	580.9055	1.65
Q8	339351.9	4406088.9	24.6	18.4	1.183	729.911	2.35
Q9	338718.9	4406652	23.3	17.1	0.7346	453.2482	1.05
Q10	340760.1	4406023	23.6	17.4	0.8381	517.1077	1.35
Q11	341752	4406345	32.1	25.9	3.7697	2325.9049	9.85
Q12	342195	4406735	33.7	27.5	4.3216	2666.4272	11.45
Q13	341085.1	4406183.1	24.7	18.5	1.2174	751.1358	2.45
Q14	342241.1	4406759.4	33	26.8	4.0801	2517.4217	10.75
Q15	342684.4	4406975.2	26.6	20.4	1.8728	1155.5176	4.35
Q16	343151.9	4407204.8	25.2	19	1.3899	857.5683	2.95
Q17	343583.7	4407426.8	24.5	18.3	1.1485	708.6245	2.25
Q18	344014.7	4407617.1	24.4	18.2	1.114	687.338	2.15
Q19	344494.7	4407859.6	22.3	16.1	0.3897	240.4449	0.05
Q20	344961.3	4408085.1	21.8	15.6	0.2172	134.0124	-0.45
Q21	345349.9	4408282.4	20.7	14.5	-0.1622	-100.0774	-1.55
Q22	341339	4406290.8	24.7	18.5	1.2174	751.1358	2.45
Q23	340924.4	4406087	24.9	18.7	1.2864	793.7088	2.65
Q24	340494.1	4405870.2	22.6	16.4	0.4932	304.3044	0.35
Q25	340027.9	4405633.1	23	16.8	0.6311	389.3887	0.75
Q26	339560.4	4405412.9	24.6	18.4	1.183	729.911	2.35
Q27	339132.1	4405201.3	24.5	18.3	1.1485	708.6245	2.25
Q28	338646.3	4404960	24.5	18.3	1.1485	708.6245	2.25
Q29	340450.5	4405381.4	25.7	19.5	1.5624	964.0008	3.45
Q30	340393.8	4404921.4	27.4	21.2	2.1487	1325.7479	5.15
Q31	340341.8	4404469.2	25.8	19.6	1.5968	985.2256	3.55
Q32	340150.5	4403920.9	23.2	17	0.7001	431.9617	0.95
Q33	338563.9	4400325.1	24.5	18.3	1.1485	708.6245	2.25
Q34	340993.7	4405678.2	28.8	22.6	2.6315	1623.6355	6.55
Q35	341435.3	4405426.2	27.7	21.5	2.2522	1389.6074	5.45
Q36	341700.5	4405240.1	25.6	19.4	1.5279	942.7143	3.35
Q37	340855.6	4408854.5	22.1	15.9	0.3207	197.8719	-0.15
Q38	340740.8	4407728.3	21.9	15.7	0.2517	155.2989	-0.35
Q39	340673.6	4407198.8	21.8	15.6	0.2172	134.0124	-0.45
Q40	340603	4406608.8	22.6	16.4	0.4932	304.3044	0.35
Q41	340547.1	4406133.6	22.3	16.1	0.3897	240.4449	0.05
Q42	339073.2	4406340.9	22.7	16.5	0.5276	325.5292	0.45

Q43	339619.1	4405855.6	24.2	18	1.045	644.765	1.95
Q44	340147.6	4405357.8	23.8	17.6	0.907	559.619	1.55
Q45	338332.5	4405965.8	24.7	18.5	1.2174	751.1358	2.45
Q46	338763.8	4406219	22.8	16.6	0.5621	346.8157	0.55
Q47	338825.3	4407311.9	22.2	16	0.3552	219.1584	-0.05
Q48	339341.9	4407198.9	22.1	15.9	0.3207	197.8719	-0.15
Q49	339670.8	4406991.4	22.1	15.9	0.3207	197.8719	-0.15
Q50	340051.1	4406905.1	21.9	15.7	0.2517	155.2989	-0.35
Q51	340796.9	4405305.3	30.7	24.5	3.2868	2027.9556	8.45
Q52	340640.5	4404870.4	28.7	22.5	2.597	1602.349	6.45
Q53	340761.2	4405084.4	28.6	22.4	2.5626	1581.1242	6.35
Q54	341222.8	4404839.8	21.7	15.5	0.1828	112.7876	-0.55
Q55	341392.3	4405132.8	22.7	16.5	0.5276	325.5292	0.45
Q56	341894.3	4405643.4	27	20.8	2.0107	1240.6019	4.75
Q57	342314.9	4405870.5	24.9	18.7	1.2864	793.7088	2.65
Q58	342641.2	4406268.6	24.7	18.5	1.2174	751.1358	2.45
Q59	343115.7	4406388.5	25.8	19.6	1.5968	985.2256	3.55
Q60	343589	4406494.8	25.6	19.4	1.5279	942.7143	3.35
Q61	343149.1	4406820.5	23.3	17.1	0.7346	453.2482	1.05
Q62	342744.7	4407225.7	29.6	23.4	2.9075	1793.9275	7.35
Q63	342541.4	4407369.5	30.4	24.2	3.1834	1964.1578	8.15
Q64	342363.6	4407543.7	35.6	29.4	4.9769	3070.7473	13.35
Q65	342219.6	4407663.5	34.1	27.9	4.4595	2751.5115	11.85
Q66	342022.3	4407820.7	34.9	28.7	4.7354	2921.7418	12.65
Q67	341826.2	4408004.4	27.2	21	2.0797	1283.1749	4.95
Q68	341579.5	4408138.9	22.9	16.7	0.5966	368.1022	0.65
Q69	341619.5	4408619.4	23.1	16.9	0.6656	410.6752	0.85
Q70	342120.2	4408742.7	27.7	21.5	2.2522	1389.6074	5.45
Q71	342622.8	4408827.5	28.1	21.9	2.3901	1474.6917	5.85
Q72	342956.8	4408920.4	26.4	20.2	1.8038	1112.9446	4.15
Q73	343488.6	4408833.6	23.5	17.3	0.8036	495.8212	1.25
Q74	344015.2	4408704.9	20.6	14.4	-0.1966	-121.3022	-1.65
Q75	345326	4407712.4	21.2	15	0.0103	6.3551	-1.05
Q76	345433.9	4407223.9	23.2	17	0.7001	431.9617	0.95
Q77	345629.5	4406721.9	22.5	16.3	0.4587	283.0179	0.25
Q78	345832.4	4406272	21.6	15.4	0.1483	91.5011	-0.65
Q79	345888.6	4405783.9	22.9	16.7	0.5966	368.1022	0.65
Q80	345477.8	4405521.8	24.7	18.5	1.2174	751.1358	2.45
Q81	345006.1	4405741.6	23.2	17	0.7001	431.9617	0.95
Q82	344943.8	4406533.8	23.1	16.9	0.6656	410.6752	0.85

Q83	344720.5	4407050	23.1	16.9	0.6656	410.6752	0.85
Q84	344258.8	4406815.9	22.9	16.7	0.5966	368.1022	0.65
Q85	344032.4	4407179.6	23.8	17.6	0.907	559.619	1.55
Q86	344551.2	4407517.1	23.5	17.3	0.8036	495.8212	1.25
Q87	343347	4407926	25.6	19.4	1.5279	942.7143	3.35
Q88	342899.2	4408095.9	30.5	24.3	3.2179	1985.4443	8.25
Q89	342538.5	4408209.8	31.1	24.9	3.4248	2113.1016	8.85
Q90	342194.6	4408361.5	43.9	37.7	7.8395	4836.9715	21.65
Q91	342140.4	4407158.5	32.9	26.7	4.0456	2496.1352	10.65
Q92	341572.7	4407188.3	25	18.8	1.3209	814.9953	2.75
Q93	341139.6	4407414.1	22.3	16.1	0.3897	240.4449	0.05
Q94	342230.7	4406386.9	28.4	22.2	2.4936	1538.5512	6.15
Q95	341435	4405981.3	30.4	24.2	3.1834	1964.1578	8.15
Q96	339712.7	4404952.7	23.8	17.6	0.907	559.619	1.55
Q97	339214.8	4404229.5	22	15.8	0.2862	176.5854	-0.25
Q98	338938.8	4405701	24.9	18.7	1.2864	793.7088	2.65
Q99	339926.6	4406403.9	22.9	16.7	0.5966	368.1022	0.65
Q100	339884.1	4408113.1	22.4	16.2	0.4242	261.7314	0.15
Q101	339194.4	4407797.3	22.6	16.4	0.4932	304.3044	0.35
Q102	342354	4408583	39.7	33.5	6.391	3943.247	17.45
Q103	342362	4409161	26.6	20.4	1.8728	1155.5176	4.35
Q104	342440	4409553	27	20.8	2.0107	1240.6019	4.75
Q105	342652.3	4409609.5	25.8	19.6	1.5968	985.2256	3.55
Q106	342848.7	4409689.5	21.3	15.1	0.0448	27.6416	-0.95
Q107	343080.4	4409691.5	21.8	15.6	0.2172	134.0124	-0.45
Q108	343329.4	4409642.1	22.5	16.3	0.4587	283.0179	0.25
Q109	342290.2	4409788.2	22	15.8	0.2862	176.5854	-0.25
Q111	337715	4404261.2	23	16.8	0.6311	389.3887	0.75
Q113	336771.5	4404111.3	22.3	16.1	0.3897	240.4449	0.05
Q114	336013.6	4403614.6	23.1	16.9	0.6656	410.6752	0.85
Q115	335408.1	4403364.4	22.2	16	0.3552	219.1584	-0.05

Appendix D: Magnetic Susceptibility Data

Table D1. Magnetic Susceptibility Measurements. Data acquired by N. Dellerman in 2020.

Station	Measurement (x10^-3 SI)	Map Unit	X (NAD83 UTM zone 11N)	Y (NAD83 UTM zone 11N)
MAG-1	2.12	Ta	338524	4408523
MAG-2	4.09	Ta	338703	4408652
	3.63			
MAG-3	0.057	Tas	338681	4408674

	0.08			
MAG-4	0.062	Tas	338607	4408653
	0.341			
	0.143			
	0.14			
MAG-5	15.1	Ta	339248	4409804
	14.5			
	5.38			
	12			
	9.24			
	17.3			
MAG-6	3.02	Tbo	339227	4409250
	3.51			
	4.38			
	9.89			
	10.1			
	12.4			
	7.32			
	5.3			
	7.32			
MAG-7	0.123	Tas	338852	4409279
	0.153			
MAG-8	18.9	Tbo	338156	4408461
	18.9			
	1.16			
	0.882			
MAG-9	0.425	Taa	338416	4408185
	0.364			
	0.251			
MAG-10	6.91	Tbo	338257	4408145
	5.16			
	8.82			
	7.85			
	13.1			
	12.6			
MAG-11	8.31	Tbo	337911	4407686
	10			
	8.53			
MAG-12	4.05	Tabr	338110	4407421
	3.65			
	5.88			
MAG-13	0.534	Kd	338279	4407432
	0.496			
	4.09			

	0.792			
MAG-14	1.52	Kd	338371	4408004
	1.72			
	0.642			
	0.4			
	0.537			
	7.06			
	0.448			
	0.48			
	0.486			
	0.673			
MAG-14a	16.4	Kd	338425	4407915
	11.7			
	2.99			
MAG-15	2.42	Tpd	346707	4403342
	5.11			
	6.33			
	7.97			
	8.9			
	3.45			
	4.51			
MAG-16	0.773	Tyt	338901	4401458
	1.52			
	0.321			
	2.06			
	2.62			
	4.71			
	5.91			
	4.6			
	3.91			
	4.4			
MAG-17	0.092	Tds	338573	4401177
	0.09			
	2.23	Tb		
	2.55			
	2.23			
	0.039	Tst		
	-0.142			
	0.056			
	0.065			
	0.081			

Appendix E: 3D Gravity Inversion Model

In addition to the gravity maps of complete Bouguer anomaly, 3D gravity inversion modeling was performed by Innovate Geothermal Ltd. The 3D gravity inversion modeling effort described here was made possible with gravity and topographic data from the Desert Queen area. In addition, a 3D geologic model and rock density data were used as constraints to guide the inversion calculations toward a geologically reasonable solution. Here follows a description provided by Jeff Witter (Innovate Geothermal Ltd., 2021) of the component parts of the inversion modeling exercise, as well as a description of the software tools utilized and the various parameters employed for the inversion calculations.

The 3D geologic model for Desert Queen was constructed based on geologic mapping and cross sections by Nolan Dellerman and James Faulds. The geologic map and cross sections were simplified to represent the main faults and stratigraphic units at Desert Queen. The commercially-available Rhino3D software (https://www.rhino3d.com/) was used by Innovate Geothermal Ltd. to construct the 3D geology from the geologic map and cross-sections.

The 3D geologic model consists of five stratigraphic units: Quaternary sediments, Tertiary volcanic rocks, Eocene-Oligocene altered sedimentary rocks, Cretaceous diorite, and undivided Mesozoic basement rocks. In addition, 22 fault surfaces were constructed for the 3D geologic model. The 3D geologic model volume is 10 km (N-S) x 10 km (E-W) and is ~3 km thick.

The gravity data from the Desert Queen area used in the inversion modeling described here come primarily from a gravity survey performed by Magee Geophysical

Services in 2009. A few dozen additional gravity measurements collected in the Desert Queen area are available from other gravity surveys performed by various groups at different times, including: UNR/Oppliger in 2003-2004, USGS/Ponce in 1997, and Phillips in 1979. All of these gravity measurements in the Desert Queen area were re-processed, merged, and leveled in the spring of 2021 by geophysicists at Magee Geophysical Services and were available for the 3D inversion modeling. A total of 438 gravity stations fall within the 3D gravity inversion model footprint and were used in the inversion modeling exercise. The complete Bouguer anomaly (CBA) gravity data with a terrain correction density of 2.5 g/cm^3 were used for the 3D inversion modeling. Mean gravity station spacing is ~400 m in most of the Desert Queen area, with wider station spacing in the upland areas to the NW, SE, and SW. Estimated error on measured gravity data is 0.05 mGal.

The starting/reference density values used in the 3D gravity inversion modeling effort are shown in Table 1. In this case, the starting and reference densities have the same value. The starting density is the density value given to the rock units at the beginning of the inversion calculations. The reference density is the density value that the inversion algorithm attempts to stay close to during each successive iteration of the inversion modeling. The rock unit density values used here were obtained from rock density measurements made on analogous rock units from the nearby Desert Peak geothermal field (J. Faulds, pers. comm., 2021).

Table E1. Starting and reference rock unit density values used in the 3D gravity inversion modeling. The density contrast values were calculated assuming an overall average model reference density of 2.5 g/cm^3.

Rock unit name	Starting/Reference rock unit density	Density contrast
Quaternary sediments	2.1 g/cm^3	-0.4 g/cm^3
Tertiary volcanics	2.25 g/cm^3	-0.25 g/cm^3
Jurassic diorite	2.6 g/cm^3	+0.1 g/cm^3
Triassic meta-sediments	2.66 g/cm^3	+0.16 g/cm^3
Mesozoic basement	2.65 g/cm^3	+0.15 g/cm^3

The upper boundary of the 3D models created in this study is the land surface. A public domain 10 m resolution digital elevation model (DEM) from the U.S. Geological Survey was used to represent the land surface. The coordinate system used for all data in this study is UTM NAD83 zone 11.

The 3D gravity inversion model has the same dimensions as the 3D geologic model. Specifically, the 3D gravity inversion model covers 100 km^2 (10 km x 10 km) and extends from the land surface to 1500 m below sea-level (i.e., ~3000 m thick).

The 3D model volume was discretized into cells to facilitate the inversion modeling. The minimum cell size in the model volume is 50 m x 50 m x 50 m. Model cell size is smallest at the topographic surface and increases downward to a maximum cell size of 200 m x 200 m x 200 m at the bottom of the model volume. The model volume consists of: 40 layers of 50 m x 50 m x 50 m cells, 10 layers of 100 m x 100 m x 100 m cells, and 3 layers of 200 m x 200 m x 200 m cells. The total number of cells in the output density model is ~1.5 million.

Software used in this 3D gravity modeling exercise includes:

- 3D gravity inversion modeling engine -- SimPEG (https://simpeg.xyz/; Cockett et al., 2015)
- Inversion modelling GUI – GeoAPPS (https://geoapps.readthedocs.io/en/stable/index.html)
- Visualization and data management tools -- Geoscience Analyst (https://mirageoscience.com/mining-industry-software/geoscience-analyst/) and Rhino3D (https://www.rhino3d.com/)

The purpose of gravity inversion modeling is to generate a density model of the subsurface depicting the distribution of rock density that is quantitatively consistent with the variations in the gravity signal measured at the land surface (Li and Oldenburg, 1998; Fullagar and Pears, 2007; Fullagar et al., 2008). The analytical approach applied for Desert Queen was similar to other recent efforts (e.g., Siler et al., 2020; Witter et al., 2016, 2018).

The 3D gravity inversion modeling effort described here, for Desert Queen, consisted of two specific steps. First, a 3D geologic model (V1) was constructed, and 3D gravity inversions were run using this V1 geology model. The density model results were interpreted, and some of the geologic cross sections were then revised by Nolan Dellerman as part of this study. The second step involved construction of an updated 3D geologic model (V2) using the revised cross sections and then running more 3D gravity inversions using the V2 geology model.

During each gravity inversion model run, the stratigraphic contacts from the 3D geologic model are fixed, and the inversion modeling solves for density in each of the model cells. At the outset, the inversion algorithm begins with the starting density values

for each rock unit (Table D1), and progressively changes density values (within ± 0.5 g/cm^3 of the starting values) until the target misfit value (±0.05 mGal) is reached. The 0.05 mGal value was chosen, because it is equal to the estimated gravity measurement error. The misfit is calculated at each gravity station, and it is the difference between the measured gravity data and the calculated gravity response of the model volume.

In addition to a 3D density model volume, each 3D inversion run generates a map of the misfit. From these misfit maps, the root-mean-squared (RMS) misfit is calculated as a measure of the overall fit of the model output to the measured gravity data. In all of the Desert Queen 3D gravity inversion runs, the RMS misfit ranged from 0.04 – 0.09 mGal. This compares to an estimated measurement error of 0.05 mGal for the gravity data itself. This is a good result, because the goal is to have the inversion model achieve a level of misfit that is mathematically consistent with the gravity data measured in the field. Note that non-uniqueness is an unavoidable problem in geophysical modeling. Of the infinite set of possible models that are consistent with the data, we cannot know which model output is "correct" based solely on the modeling. Instead, geological constraints and low levels of model misfit are tools to help guide toward what might be the most likely solutions.

The SimPEG inversion algorithm includes specific parameters that can be set by the user to explore the density model space. Two of these parameters are: Lp Norm regularization and Reference model scaling factor. The Lp Norm regularization is a parameter that varies from 0 to 2 and controls how "compact" density anomalies are portrayed in the model output. An Lp Norm value of 2 allows zones of anomalous density to be smeared out over broad areas with gradational contacts between zones of high and

low density (i.e., a smooth norm). In contrast, an Lp Norm value of 0 creates compact density anomalies with sharp boundaries between zones of high and low density (i.e., a sparse norm). An Lp Norm value of 1 models the zones of anomalous density in a manner that lies between the smooth and sparse extremes.

The Reference model scaling factor varies the influence of the 3D geologic model when calculating the 3D density model output. A high scaling factor will help preserve sharp density boundaries between the different rock units depicted in the 3D geologic model and attempt to preserve the reference density values for the rock units. A low scaling factor will be less stringent and, for example, would allow gradational density transitions across defined rock unit boundaries.

Specific gravity inversion parameters set for two of the Desert Queen inversion runs using the V2 geology model are:

DQ-V2a -- Inversion Parameters

Lp Norm regularization, s=2 (smooth norm)

Reference model scaling factor, alpha_s = 100

DQ-V2b -- Inversion Parameters

Lp Norm regularization, s=1 (smooth/sparse norm)

Reference model scaling factor, alpha_s = 100

Deliverables

All Desert Queen 3D gravity inversion models used the same input files. These input files are included as part of the deliverables and consist of:

1. Starting Mesh file in UBC format

2. Measured gravity observations file

3. Starting/Reference 3D geology model file in UBC format

4. Topography file

Two versions of the 3D density model output and misfit have been provided as part of the deliverables. These are named DQ-V2a and DQ-V2b and correspond to the models described above. The Rock Density Model files are point clouds of the 3D density models in the form of 4-column .txt files. The four columns are: X and Y locations of the point in space (in UTM NAD83 zone 11); Z is the elevation (m above sea level) of the point in space; and the fourth column is the model rock density in g/cm^3.

The DQ-V2a and DQ-V2b Model Misfit files show the amount of misfit between the observed gravity data (measured in the field) and the predicted gravity values (calculated by the inversion modeling) at each of the gravity stations. The DQ-V2a and DQ-V2b Model Misfit files include the calculations to determine the overall RMS misfit for each of these cases.

Plate 1

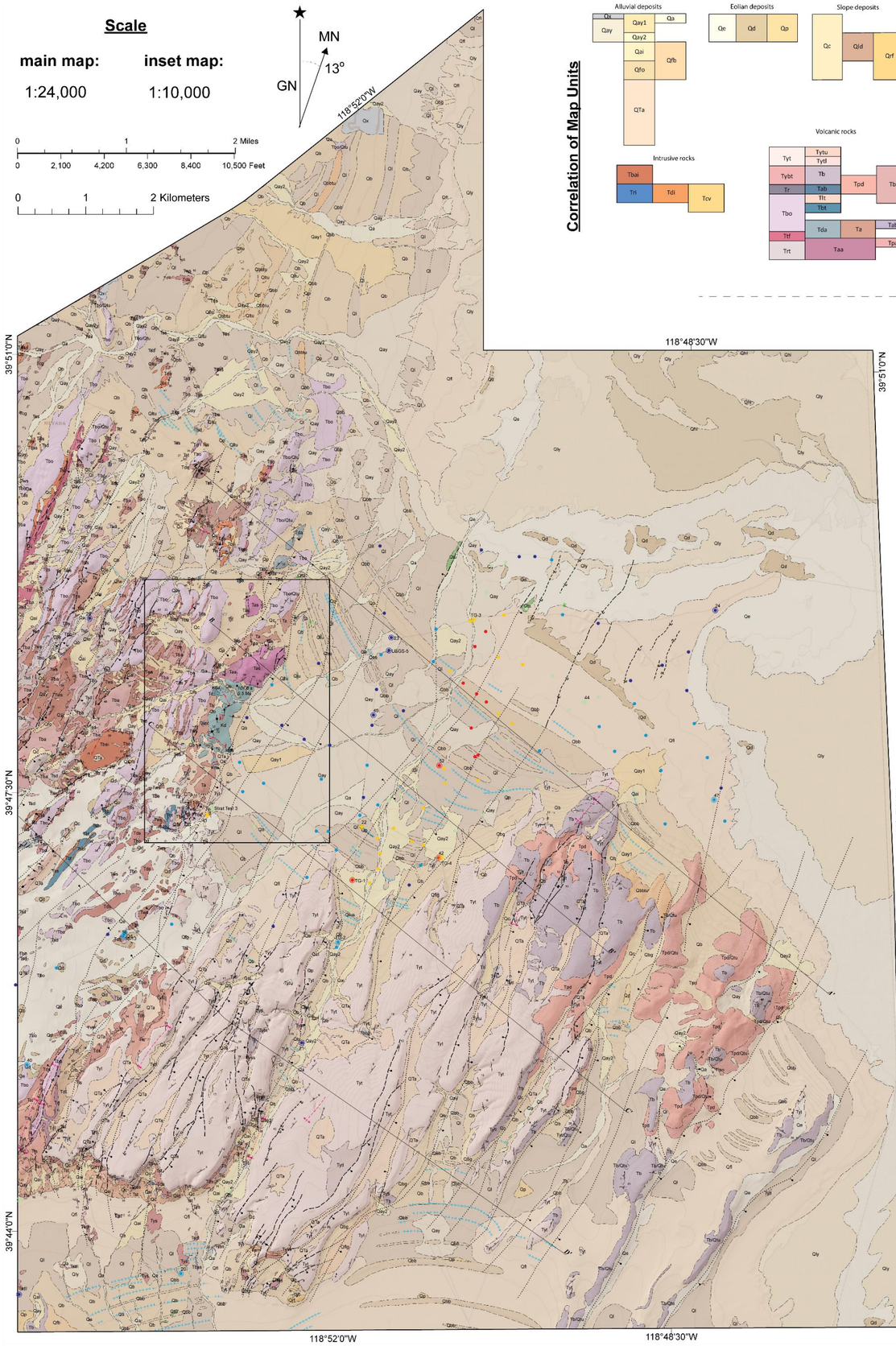

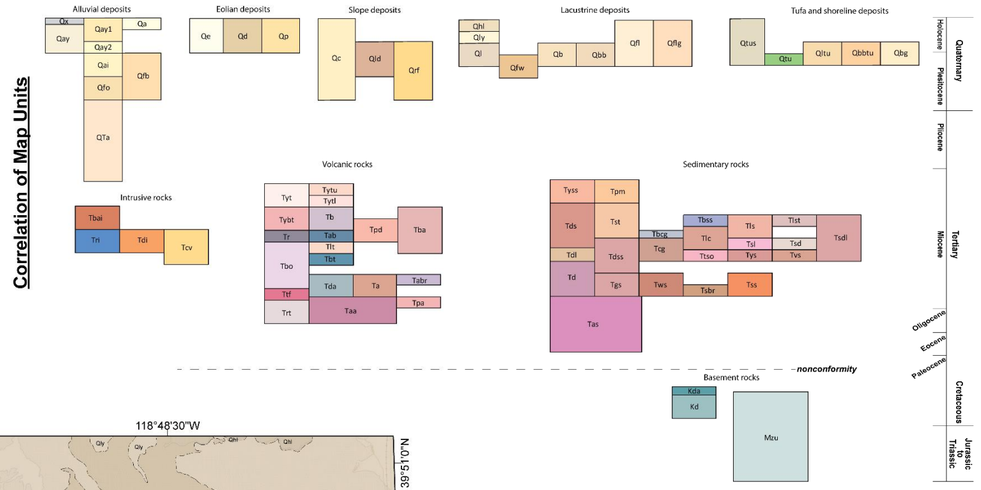

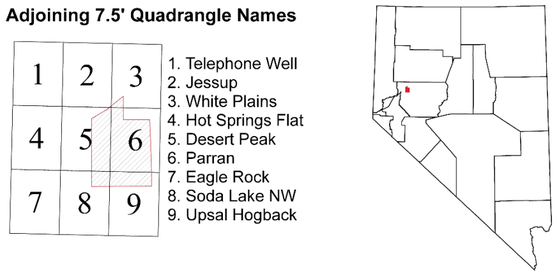

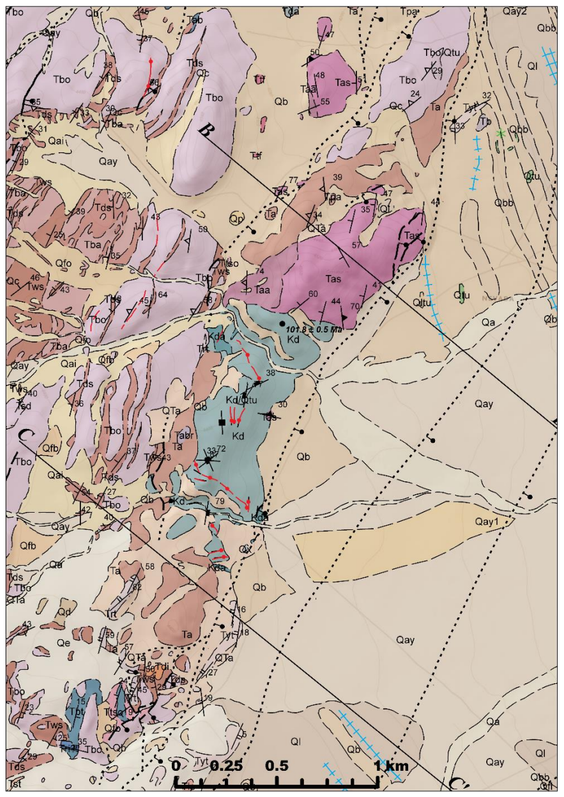

Plate 1:
GEOLOGIC MAP OF THE DESERT QUEEN GEOTHERMAL AREA, CHURCHILL COUNTY, NEVADA

Compiled by: Nolan Dellerman
Mapping contributions by: James Faulds, Heather Green, and Nolan Dellerman

Map Symbols

Contact - Dashed where approximate.

Normal fault - Solid where certain, dashed where approximate, dotted where concealed, queried if existence uncertain. Ball on downthrown side.

Anticline - Dashed where approximately located, dotted where concealed.

Syncline - Dashed where approximately located, dotted where concealed.

Spit or bar - Dashed where approximate.

Dike - Dashed where approximate.

Vein - Dashed where approximate.

Line of cross section.

Strike and Dip of Bedding
Inclined

Strike and Dip of compaction foliation in ash-flow tuff
Inclined

Strike and Dip of flow banding, lamination, or foliation in igneous rock
Inclined Horizontal

Strike and Dip of metamorphic foliation
Inclined Vertical

Strike and Dip of joints
Inclined Vertical

Tufa • **U-Pb geochronology sample point**

Temperature at 2 m depth (°C)
- 20.6 - 22.4
- 22.4 - 23.9
- 23.9 - 27.0
- 27.0 - 32.1
- 32.1 - 43.9

Geothermal well temperatures at ~60 m depth (°C)
- 0.0 - 25.2
- 25.2 - 32.0
- 32.0 - 39.7
- 39.7 - 63.9
- 63.9 - 92.3

Cross Sections

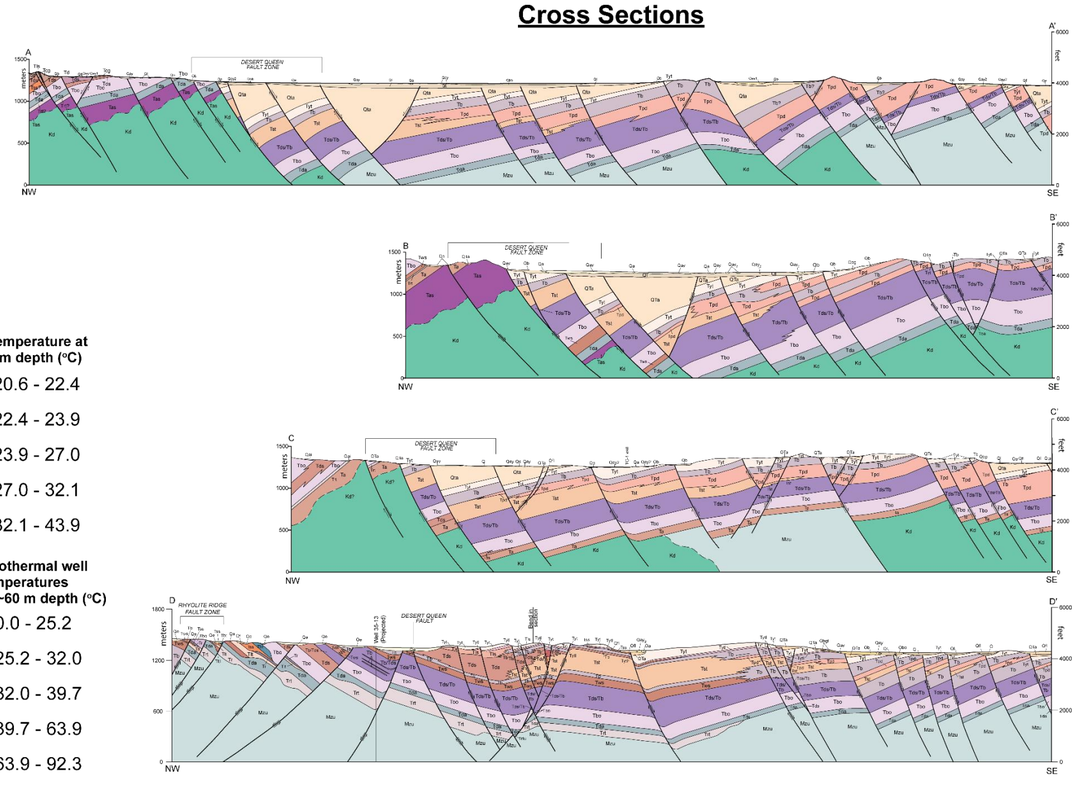

Quaternary alluvial fan, playa, and eolian deposits

- Qx — Disturbed areas, consisting of mine dumps, gravel pits, etc. Undivided.
- Qa — Young active alluvium. Active wash and alluvial fan deposits of poorly sorted gravel, sand, and silt.
- Qe — Eolian deposits. Windblown sand and silt deried from late Pleistocene to mid Holocene lacustrine deposits. Locally divided into Eolian sand dunes.
- Qd — Eolian sand dunes.
- Qp — Ephemeral playa deposits. Sand, silt, and mud in small closed depressions, and behind beach gravel bars.
- Qld — Landslide deposits. Massive angular blocks.
- Qc — Colluvium. Coarse, poorly-sorted, angular to subangular gravel on steep bedrock slopes.
- Qrf — Rockfall.
- Qay — Young fan alluvium, undivided.
- Qay1 — Young fan alluvium, mid to late-Holocene. Silty, sandy pebble gravel; bar-and-channel morphology; moderately varnished.
- Qay2 — Young fan alluvium,early Holocene to mid-Pleistocene. Silty, sandy pebble gravel; bar-and-channel morpology; darkly varnished.
- Qfw — Subaerial deposits of the Wyemaha alloformation, late Pleistocene.
- Qai — Remnant alluvial fan. Pebble to cobble conglomerate, late to middle Pleistocene.
- Qfo — Old alluvial fan deposits, early to middle Pleistocene.
- Qfb — Alluvial deposits with mainly basaltic clasts.
- QTa — Old alluvium found within the Hot Springs Mountains. Early Pleistocene to late Miocene.

Quaternary lacustrine and spring deposits

- Qhl — Modern Humboldt Lake, Holocene.
- Qly — Offshore deposits of the Holocene lacustrine cycle. Silt, sand, and mud.
- Ql — Lacustrine silt, sand, and mud of the Sehoo formation, undivided.
- Qltu — Lacustrine silt, sand, and mud of the Sehoo formation with massive lithoid tufa deposits.
- Qb — Nearshore and onshore beach and shoreline deposits associated with the Sehoo lacustral cycle. Poorly-sorted sand, pebbles, cobbles, and boulders.
- Qbb — Shoreline beach-berm deposits of the Sehoo formation. Curvilinear beach berms of poorly-sorted sand, pebbles, cobbles, and boulders.
- Qbbtu — Shroeline beach-berm deposits with massive lithoid tufa deposits.
- Qbg — Nearshore and onshore beach and shoreline deposits associated with the Sehoo lacustral cycle consisting primarily of bouldery gravel.
- Qtus — Shoreline tufa deposits.
- Qtu — Massive lithoid tufa deposits.
- Qfl — Young fan alluvium and lacustrine deposits, undivided.
- Qflg — Young fan alluvium and beach gravels.

Miocene volcanic and sedimentary rocks

- Tyt/Qtu — Tyt covered by abundant shoreline tufa.
- Tytu — Upper poorly welded reddish-brown to locally pale brown Tyt.
- Tyt — Ash-flow tuff- Aphyric ash-flow tuff. Sparse (<1%) phenocrysts of plagioclase, biotite, and rare sanidine. Lower part contains abundant black fiamme. Up to ~60 m thick, ~7.5 Ma.
- Tytl — Lower poorly welded, reddish-brown, pumice-rich Tyt.
- Tybt — Bedded white tuff.
- Tyss — Grayish-white, medium- to coarse-grained feldspathic arenite with subrounded grains.
- Tpm — White to light gray, massive, poorly sorted, pumice-rich, matrix-supported conglomerate with angular to subangular clasts of basalt up to 15 cm long.
- Td — Diatomite - massive.
- Tds — White diatomaceous shale that appears to pinch out toward the east.
- Tdl — Lowe member of Tds.
- Tdss — Diatomaceous shale and sandstone.
- Tst — Pale gray to white tuffaceous siltstone and lesser fine- to medium-grained sandstone; locally includes diatomaceous shale, thin limestone beds, and light gray tephras up to ~1 m thick.
- Tbss — Light gray to bluish-gray, medium- to coarse-grained, moderately sorted, litharenite and pebble conglomerate consisting primarily of subrounded grains or clasts of basalt and lesser feldspar..
- Tcv — Calcite veins.
- Tbcg — Poorly exposed, essentially unconsolidated bouldery congolmerate containing angular to subrounded clasts of aphanitic and porphyritic basalt. Stratigraphic position unclear.
- Tcg — Congolmerate, mainly basalt clasts.
- Tsd — Silicified siltstone and diatomite.
- Tsl — Lacustrine sediments, including diatomaceous shale, siltstone, and sandstone.
- Tlc — Carbonate clastics.
- Tls — Limestone, locally containing abundant tufa. ~9-10 Ma.
- Tlst — Limestone dominated by tufa.
- Tsdl — Interbedded white tuffaceous siltstone, diatomaceous shale, and limestone.
- Tvs — Volcaniclastic sandstone.
- Tys — Yellowish fine- to medium-grained, poorly indurated sandstone and siltstone.
- Tb/Qtu — Aphanitic basalt largely covered by shoreline tufa.
- Tb — Aphanitic, typically vesicular basalt containing 1-10% phenocrysts of olivine, plagioclase, and sparse pyroxene up to ~3 mm long. Includes pods of scoriaceous basaslt
- Tpd/Qtu — Porphyritic dacite largely covered in shoreline tufa.
- Tpd — Porphyritic dacite containing ~35% phenocrysts of plagioclse (up to ~6 mm long), lesser hornblende (up to ~5 mm long), and biotite. Includes parts of domes, flows, and dikes.
- Tlso — Older tuffaceous sediments.
- Tab — Altered younger basalt lavas.
- Tri — Rhyolite intrusions.
- Tr — Rhyolite lavas.
- Tbai — Basaltic andeiste intrusion.
- Tba — Basaltic andesite lavas.
- Tdi — Dacite intrusions.
- Tbo/Qtu — Basalt largely covered with late Pleistocene shoreline tufa.
- Tbo — Older aphanitic basalt lavas, undivided.
- Tgs — Gray shale.
- Tws — White siltstone with lesser diatomite.
- Tsbr — Rock avalanche breccia.
- Tbt — Bedded tuff.
- Tss — Sandstone.
- Tlt — Lithic-rich aphyric ash-flow tuff.
- Ttf — Finely porphyritic plagioclase-rich ash-flow tuff.
- Tabr — Andesite breccia.
- Tpa — Porphyritic andesite.
- Tda — Dacite and andesite lavas.
- Ta — Andesite lavas.
- Trt — Late Oligocene to early Miocene rhyolite ash-flow tuffs (undivided). Only upper member is represented on map.

Early Tertiary rocks

- Taa — Altered andesite lavas. Presumed Oligocene to early Miocene.
- Tas — Highly altered and silicified sedimentary rocks. Interbedded sandstone, conglomerate, and siltstone). Paleocene to Eocene based on analysis of detrital zircons.

Cretaceous basement rocks

- Kd/Qtu — Diorite largely covered by late Pleistocene shoreline tufa.
- Kda — Highly altered diorite.
- Kd — Diorite pluton. Altered greenish gray pyroxene and amphibole rich diorite with relatively lower proportion of plagioclase (>10%). Quartz veinlets common with larger (up to 2m) mineral rich veins throughout.

Undivided basement rocks

- Mzu — Undivided basement rocks. Assumed Mesozoic. Only represented in cross sections.

-Projection: Universal Transverse Mercator zone 11, North American Datum 1983 (m)
-Topo base from USGS National map
-Contour interval 40 ft